Optimization of Jet Energy Resolution and Response of the DØ Detector

by

John P. Borders

Submitted in Partial Fulfillment
of the
Requirements for the Degree
Doctor of Philosophy

Supervised by
Professor Thomas Ferbel

Department of Physics and Astronomy
College of Arts and Science

University of Rochester
Rochester, New York

1994

AAD2069

FERMILAB
LIBRARY

For Amy

Curriculum Vitae

The author was born in Lafayette, Indiana He attended Purdue University from 1983 to 1987, and graduated with a Bachelor of Science degree in 1987. He came to the University of Rochester in the Fall of 1987 and began graduate studies in physics. He pursued his research in high-energy physics under the direction of Professor Thomas Ferbel and received the Master of Arts degree in 1989.

Acknowledgements

I would like to thank all those on the DØ experiment who supported me in completing this thesis. I would also like to thank Tom Ferbel for his nearly endless patience in in advising me on editorial style and content, and Fred Lobkowicz for his erudite advice about the subtle details of the analysis. I also can't forget Paul Draper and Jerry Blazey, who guided me in choosing my course of graduate work. Finally, I acknowledge the Department of Energy for supporting the research presented in this thesis, and for allowing me the opportunity for participating in the DØ experiment.

Abstract

The DØ Experiment (E-740) is located at the Tevatron of the Fermi National Accelerator Laboratory (Fermilab). As one of only two general-purpose experiments situated to take full advantage of $p\bar{p}$ collisions at a center-of-mass energy of 1.8 TeV, DØ occupies an important position in the investigation of fundamental interactions at high energies. One of the main tools of the DØ experiment is the calorimeter, which is used to measure the energies and positions of electromagnetic particles and hadronic jets (remnants of constituents produced in $p\bar{p}$ collisions at large transverse momenta). To be of value, calorimeters must be calibrated using particles of known energy. Electrons and hadrons traversing calorimeter modules of the DØ detector were studied in a special test beam during the period between July 1991 and January 1992. A subset of the collected data is used here to improve the ability to measure the energy of hadronic jets.

Using hadron data in the energy range 7.5-150 GeV, we optimize single-particle hadron energy resolution by varying the different layer weights (sampling weights) of the calorimeter that are used to parameterize the energy of incident particles. We find that through such optimizations we can achieve a 10% improvement in the energy resolution of single hadrons, and that this improvement is reduced to only about 3% when the weights are restricted to be energy-independent, position-independent, and fixed to the value that produces the best single-electron resolution. We observe that optimization causes the relative electron/hadron response to depart from unity, which suggests that weights based purely on energy loss through ionization (dE/dx), may be more suited for measuring jet energy, because they appear to produce a relative electron/hadron response of the calorimeter that is closer to unity.

Using predictions from parton fragmentation, we then assemble electron and hadron events in the energy range between 2 GeV to 150 GeV into jets of energy between 15 GeV to 225 GeV. These jets should be very similar to jets observed at DØ. We find that optimizing layer weights can improve the resolution of such simulated jets by a significant amount (10-15%) over that found using weights proportional to dE/dx. Our results can be used to develop techniques that could also improve the energy resolution of jets observed in DØ.

Contents

Curriculum Vitae iii

Acknowledgements iv

Abstract v

Chapter 1. Introduction 1

1.1 The Fundamental Constituents of Matter 3

1.2 The Standard Model 4

1.2.1 Fundamental Particles in the Standard Model 4

1.2.2 Fundamental Interactions in the Standard Model 6

1.3 Testing the Standard Model 7

1.3.1 Collider Physics 8

1.3.2 Perturbative QCD 9

1.3.3 Search for the Top Quark 12

1.3.4 Searches Beyond the Standard Model 14

Chapter 2. Calorimetry 16

2.1 Interactions Within a Calorimeter 17

2.1.1 Electromagnetic Interactions 18

2.1.2 Hadronic Interactions 19

2.1.3 Mixed Interactions (Jets) 22

2.2 Sampling Calorimeters 23

2.2.1 Energy Measurement in a Sampling Calorimeter 24

2.2.2 Energy Resolution of a Sampling Calorimeter 25

2.2.3 Compensating Calorimeters 25

2.2.4 Position Resolution of Sampling Calorimeters 26

Chapter 3. The DØ Detector 27

3.1 Fermilab and the Tevatron 27

3.2 Specific Goals of DØ 29

3.3 The DØ Detector 30

3.3.1 Central Tracking 31

3.3.2 The Muon Tracking System 33

3.3.3 The Calorimeters 35

3.3.4 ICD and Massless Gaps 42

3.4 Data Acquisition, Electronics, and Triggering 43

3.4.1 Electronic System 43

3.4.2 The Trigger and Data Acquisition System 43

3.4.3 Calibration of Electronics 44

3.4.4 Zero-Suppression 45

Chapter 4. The DØ Test Beam 46

4.1 NWA Building and Neutrino West Beamline. 47

4.2 Test Beam Cryostat and Transporter 49

4.3 Load 2 Test Beam Configuration 50

4.4 Data Taken at the Test Beam 52

Chapter 5. Optimization Of Hadronic Sampling Weights Using Single Particles 56

5.1 The Process of Optimizing Sampling Weights 57

5.2 Restricting the Optimization of Hadronic Weights to Produce the Best Jet Resolution 61

5.3 Characterizing Results of Weight Optimizations 62

5.3.1 The Default Sampling Weights 62

5.3.2 Characteristics of the Response of the Calorimeter to Single Hadrons 63

5.4 Optimizing Single-Hadron Response While Applying Restrictions Aimed at Improving Jet Resolution 66

5.4.1 Results of Hadronic Optimizations 67

5.4.2 Varying only Relative Scales on the Default Set ("Shifted Set") 71

5.4.3 Quality of the Response of the Calorimeter to Hadrons 74

Chapter 6. Optimizing Jet Energy Resolution with Jets Simulated from Test-Beam Data 76

6.1 Generating Test Beam Jets 77

6.2 Parameters of Jet Response 78

6.3 Optimization of Jet Resolution 82

6.3.1 Optimization of Relative Electromagnetic and Hadronic Scales (Scheme OS-1) 83

6.3.2 Full Optimization Without Energy Dependence (Scheme OS-2) 83

6.3.3 Sampling Factors as a Function of Reconstructed Jet Energy (Scheme OS-3) 84

6.3.4 Sampling Factors that Depend on Jet EM Fraction (OS-4) 86

6.3.5 Sampling Factors that Depend on both EM Fraction and Reconstructed Energy (Scheme OS-5) 88

6.3.6 Corrections to Reconstructed Energies 90

6.4 Judging the Success of the Optimization Schemes on Resolution 91

Chapter 7. Conclusion 96

Bibliography 99

Appendix A. The DØ Test Beam Transporter 102

A.1 Design Specifications of the Transporter 103

A.2 A Description of the Transporter System 104

A.2.1 Motion of the Transporter 105

A.2.2 The Cryostat PWC 106

A.3 The Safety System 108

A.4 The Control System Electronics 110

A.5 The Transporter Control Program 112

A.5.1 Brief Summary of the Programming Language 113

A.5.2 The Transporter Program 113

A.6 Using the Transporter Control Systems 117

A.6.1 The Manual Controls for the Cryostat Transporter 117

A.6.2 The Manual Controls for the Moving PWC 118

A.6.3 The Computer Control System 119

Appendix B. DØ Particle Library 122

B.1 Contents of Particle Library 122

B.2 Using the Test Beam Particle Library to Simulate DØ Jets..... 128

B.2.1 Particle and Energy Field Selection 129

B.2.2 Energy Scaling 129

B.2.3 Position Shifting 130

B.2.4 Constructing the Jet 131

List of Figures

Figure 1.1 Example of proton-antiproton collision involving constituent quarks (q) and mediating gluons (g). 8

Figure 1.2 Examples of some lowest-order α_s^2 QCD processes 10

Figure 1.3 Examples of higher order processes 11

Figure 1.4 tt production processes 13

Figure 2.1 Energy loss mechanisms for electromagnetic processes as a function of particle energy. Photon cross sections in carbon (a) iron (b), and uranium (c). Fractional energy deposition by electrons in carbon (d), iron (e), and uranium (f) 18

Figure 2.2 Responses of hadronic and electromagnetic components 21

Figure 3.1 DØ and the Fermilab Tevatron 28

Figure 3.2 The DØ Detector and associated detector systems 31

Figure 3.3 DØ central tracking system with FDC cross section 32

Figure 3.4 Characteristics of the muon system 33

Figure 3.5 Muon WAMUS PDT cell structure, showing sense wire signals and diamond-shaped pattern of verniers pads. The different regions of the vernier pads are read out separately. 34

Figure 3.6 Perspective view of DØ calorimeters. 36

Figure 3.7 Quarter view of DØ detector, indicating the range of pseudo-rapidity of individual cells. 37

Figure 3.8 Structure of DØ calorimeter cells 38

Figure 3.9 Depth of material in the DØ detector as a function of angle from the beam pipe 38

Figure 3.10 The DØ central calorimeter 39

Figure 3.11 End calorimeter electromagnetic section 40

Figure 3.12 A Side View of the DØ Detector. Muon detector not shown. 41

Figure 3.13 Placement of ICD and massless gaps between calorimeters 42

Figure 4.1 NW Beamline 47

Figure 4.2 Sketch of test beam cryostat and transporter 49

Figure 4.3 Calorimeter modules in Load II test beam 50

Figure 4.4 Top and end views of the Load 2 configuration 51

Figure 4.5 Reconstructed energy distributions for (a) e^-, and (b) π^- for a representative set of incident energies in Load II at $\eta = 0.05$ and $\phi = 3.16$ (3.10 radians) 55

Figure 5.1 Fractional resolution obtained when using default weights at η=0.45 64

Figure 5.2 Reconstructed energies obtained using default weights at η=0.45 64

Figure 5.3 Fractional difference between incident and reconstructed energy using default weights at η=0.45 65

Figure 5.4 Fractional resolutions for hadrons at (a) η=0.05, and (b) η=0.45 70

Figure 5.5 Deviation plots for (a) η=0.05, and (b) η=0.45 71

Figure 5.6 Resolution plots for (a) η=0.05, and (b) η=0.45 72

Figure 5.7 Fractional energy deviations for (a) η=0.05, and (b) η=0.45 73

Figure 6.1 Standard deviation of "artificial" inspill pedestals (jet-pedestal events) as a function of incident jet energy 79

Figure 6.2 Reconstructed energies obtained using default weights at η=0.45 80

Figure 6.3 (a) Relative differences and (b) relative resolution for corrected reconstructed jet energies 81

Figure 6.4 Sampling factors as a function of reconstructed energy (OS-3). The fits are to linear functions of the form $P_1 + P_2 E_{def}$ (see Table 6.4). 85

Figure 6.5 Sampling factors as a function of the fraction of the reconstructed energy in a TB jet that is deposited in the EM section. The fits are to linear functions of the form $P_1 + P_2 F_{EM}$ (see Table 6.5) 87

Figure 6.6 Sampling factors as a function of EM-fraction corrected reconstructed energy (OS-5). The fits are to linear functions of the form $P_1 + P_2 E_{rec}$ (see Table 6.6). 89

Figure 6.7 Nominal parton energy as a function of reconstructed TB jet energy for various optimizations. The fits are to second-order polynomial functions of E_{rec}. 91

Figure 6.8 Fractional resolutions for TB jets as a function of incident energy for the various optimization schemes. Fits of the data are to Eq. 6.2 93

Figure 6.9 Ratio of optimized TB jet resolutions to the default values as a function of jet parton energy. 94

Figure 6.10 Fractional differences between the corrected reconstructed TB jet energies and incident parton energies, for different optimization schemes. 95

Figure A.1 Calorimeter modules studied in the DØ test beams. 103

Figure A.2 NWA Test Beam cryostat and transporter layout 104

Figure A.3 Sketch of test beam cryostat and transporter 105

Figure A.4 Linear scales on tables used for mounting the Cryostat PWC 107

Figure A.5 The transporter control and readback system 111

Figure A.6 Diagram of transporter control program 115

Figure A.7 Manual controls for transporter 117

Figure A.8 Manual controls for the cryostat PWC 118

Figure A.9 Remote keypad and display for computer-controlled transporter system 120

Figure B.1 Particle Library hadrons from 2 GeV to 20 GeV 124

Figure B.2 Particle Library hadrons from 25 GeV to 150 GeV 125

Figure B.3 Particle Library electrons from 2 GeV to 20 GeV 126

Figure B.4 Particle Library electrons from 25 GeV to 150 GeV 127

Figure B.5 Polynomial fits to electron and hadron data in the Particle Library 128

List of Tables

Table 1.1 Fundamental Particles 5

Table 1.2 Force-Mediating Bosons 6

Table 3.1 Muon Toroid Characteristic 34

Table 4.1 Test Beam data incorporated in this thesis 52

Table 5.1 Default sampling weights, with $\alpha = 0.00394$ and $\delta = 0$ 63

Table 5.2 Definitions of sets of hadronic weights 67

Table 5.3 Sampling Factors for Set 1 67

Table 5.4 Sampling Factors for Set 2 68

Table 5.5 Sampling Factors for Sets 3, 4, 5, and 6 68

Table 5.6 Parameters from optimizations at η=0.05 69

Table 5.7 Parameters from optimizations at η=0.45 69

Table 5.8 Results from varying only the relative hadronic scale, α' 72

Table 6.1 Summary of optimization schemes (OS) 82

Table 6.2 Optimized relative scales (OS-1) 83

Table 6.3 Fully optimized, energy-independent sampling factors (OS-2) 84

Table 6.4 Parameters describing energy-dependence of sampling factors (OS-3) 86

Table 6.5 Energy-independent sampling factors (OS-4) obtained from linear fits to the EM energy fraction in TB jets (with statistical uncertainties from the fits) 88

Table 6.6 Energy dependent sampling factors obtained from linear fits to the energy after it is corrected for EM fractions (OS-5) (with statistical uncertainties from the fits) 90

Table 6.7 Parameters from fits of second-order polynomial in reconstructed TB jet energy to the incident parton energy (with statistical errors from the fits) 90

Table 6.8 Parameters describing resolution of reconstructed and corrected TB jet energies 92

Table A.1 Transporter motor parameters of motion 106

Table B.1 ID numbers for the energy fields in the Particle Library 127

Chapter 1.

Introduction

It was Democritus who first speculated on the possibility of the smallest possible particle, which he called the *atom*. Although science has applied that label to an object that is now known to be made of even more fundamental particles, the concept of having a smallest possible unit of matter still entrances us all. Particle physics is based on such concepts, and it involves the investigation of the properties of the most fundamental particles, forces, and interactions that make up the universe. The origins of this field can be traced to experiments such as those of Curie, Thomson, and Rutherford, whose groundbreaking research into the nature of radiation and matter has laid the foundation for the more sophisticated modern investigations.

In this search for yet smaller, and thus more fundamental, particles, it has been necessary to develop methods to probe the fine structure of matter. It is important to investigate not only normal and stable matter, but also particles that are rarely, if ever, observed in nature. The best way to probe these issues is through the use of particle accelerators, and the only way to measure the results of the interactions produced by accelerators is through modern detector techniques.

The Fermi National Accelerator Laboratory in Batavia, Illinois, USA, is the site of the Tevatron, currently the world's highest-energy particle accelerator. The Tevatron is

capable of boosting protons and antiprotons to an energy of 0.9 TeV, producing collisions with a center-of-mass energy of 1.8 TeV. This very powerful device provides an environment in which much important physics has been performed in fixed target experiments, and, as the collider detectors CDF and DØ mature, even more exciting discoveries may be forthcoming. Investigations are underway to provide precise tests of the Standard Model, the latest modern view of matter, and to search for fundamental particles that are predicted, but not yet observed, such as the top quark and the Higgs boson. Also, if the Standard Model is to prove inadequate, the Tevatron is the most likely existing tool that can provide evidence for any departures.

The DØ experiment, as one of only two general-purpose collider experiments equipped to take full advantage of the collision energies available at the Tevatron, occupies an important position for testing the Standard Model. However, the DØ detector would be of little use if an accurate calibration of its response were not available. In order to fully calibrate the detector, and to obtain a complete understanding of its operation, a fixed-target test beam was set up on the Neutrino West Beamline at Fermilab. At the test beam, various modules of the DØ calorimeter and components of the tracking system were placed in a beam of particles of known energy and trajectory, thereby allowing a complete investigation of detector response that could be used to simulate interactions expected in the DØ collider experiment.

This dissertation is concerned with various aspects of the measurement of the response of the DØ calorimeter to particles in the test beam, and with ways to extend that information to the study of multiparticle jets. The remainder of this chapter will outline the historical and theoretical development of the Standard Model, and describe some of the physics options for DØ. Chapter 2 will present the basic concepts of calorimetry, which provides the principal investigative tool for DØ. A description of the DØ detector is given in Chapter 3, and Chapter 4 describes the apparatus at the DØ test beam. Chapters 5 and 6 present the results of analysis of the test-beam data that are needed to provide optimized use of the DØ detector for the measurement of the energies of hadronic jets. Finally, Chapter 7 contains the conclusions that can be drawn from this analysis. Information on the DØ test-beam Particle Library and the test-beam

Transporter system, subjects to which I have made major contributions, are provided in appendices for future reference.

1.1 The Fundamental Constituents of Matter

In the 1800s, the atom was presumed to be the most basic building block of all matter. With the verified existence of nearly a hundred different elements, and hence different atoms, matter seemed to be made of a very complex set of fundamental particles.

At the turn of the century, J. J. Thomson discovered electrons: charged particles whose charge-to-mass ratio was much greater than that for ions. This introduced the possibility that atoms were composed of many of these smaller, negatively charged particles, each balanced out with corresponding positive charges. Then, in 1911, Rutherford and his colleagues published results in which α particles were scattered from thin metal foils. From the observed scattering distribution it was apparent that atoms were composed mostly of empty space, and a small, massive, positively charged nucleus. A more complete model of the atom was proposed in the 1930s (after the discovery of the neutron), in which matter is composed of a small number of subatomic particles: electrons, protons, and neutrons.

Subsequently, however, new particles were observed in cosmic rays and in experiments in early particle accelerators: positrons, muons, pions, kaons, hyperons, etc. The group of particles that had *strong* interactions (including protons and neutrons) were called *hadrons*. Since all of these particles appeared to be indivisible, it seemed that they were all elementary. However, as hundreds of hadrons were soon identified, scientists were again faced with a bewilderingly large number of fundamental constituents of matter.

In order to account for the huge array of hadrons, Gell-Mann[1] (and, independently, G. Zweig)[2] in 1964 attempted to describe them as composites of a smaller number of even more fundamental constituents, which Gell-Mann termed *quarks*. Soon experimental results began to support this theory. Deep inelastic scattering experiments were performed in the late 1960s, in which high-energy electrons were scattered off protons and neutrons. This was known as "deep" scattering because, through the uncer-

tainty principle, the high momentum transfers from the incident electrons to the target provided "deep" probes into the structure of the nucleon. The distribution in the angles of the inelastically scattered electrons suggested that the electrons collided with point-like charged objects (which were termed partons) that resided within the nucleon. Soon Gell-Mann's quarks became identified with these partons (both quarks and gluons).

Today it is recognized that there are a relatively small number of fundamental particles that are described by the Standard Model, and that quarks and gluons are constituents of all hadrons.

1.2 The Standard Model

The Standard Model is based on a gauge theory, and has its underpinnings in the Glashow-Weinberg-Salam (electroweak) theory, which describes the behavior of the unified weak and electromagnetic interactions, and in Quantum Chromodynamics (QCD), which describes the behavior of strong (color) interactions.

Gauge theories contain force-mediating bosons to transmit interactions. QED uses a simple U(1) group to describe the electromagnetic force through the exchange of massless photons. Electroweak theory expands this to the SU(2)⊗U(1) group to account for the existence of three additional massive *intermediate vector bosons* (IVBs) as the carriers of the weak force. These bosons correspond to the charged W^+ and W^-, and to the electrically neutral Z^0. Finally, QCD involves the color SU(3) group, which contains an octet of color-charged gluons that carry the strong force. The Standard Model, combining electroweak theory and QCD, involves the $SU_C(3)\otimes SU_W(2)\otimes U_Q(1)$ group to describe the existence of all of these force mediators. (C refers to color, W to weak isospin, and Q to electric charge, the symmetries pertinent to the Standard Model.)

1.2.1 Fundamental Particles in the Standard Model

The Standard Model describes matter as consisting of two types of point-like, spin 1/2 fermions: *quarks* and *leptons*[3]. These come in at least three different groupings, or *families*. The Standard Model does not constrain the number of families of particles, so the possibility of having additional leptons and quarks cannot be excluded. Interactions among all these particles are described in terms of the transfer of a third type of field particle: the *gauge boson*.

The properties of the fundamental particles are given in Table 1.1. The fundamental fermions are arranged in the form of weak-isospin doublets.

Table 1.1 Fundamental Particles

				Color charge	Electric Charge	Weak Hypercharge
Quarks	$\begin{pmatrix} u \\ d \end{pmatrix}$	$\begin{pmatrix} c \\ s \end{pmatrix}$	$\begin{pmatrix} t \\ b \end{pmatrix}$	$\begin{pmatrix} r,g,b \\ r,g,b \end{pmatrix}$	$\begin{pmatrix} +2/3 \\ -1/3 \end{pmatrix}$	$\frac{1}{3}$
Leptons	$\begin{pmatrix} \nu_e \\ e \end{pmatrix}$	$\begin{pmatrix} \nu_\mu \\ \mu \end{pmatrix}$	$\begin{pmatrix} \nu_\tau \\ \tau \end{pmatrix}$	—	$\begin{pmatrix} 0 \\ -1 \end{pmatrix}$	-1

There are six different leptons: *electron*, *electron neutrino*, *muon*, *muon neutrino*, *tau*, and *tau neutrino*, and all are subject to the weak force. The charged leptons couple to the electromagnetic force, but no leptons are affected by the strong force. The weak hypercharge Y of the doublets is related to weak isospin I and charge Q through the relation $Y=2(Q-I_3)$.

Only five of the six quarks have been detected thus far: *up*, *down*, *charm*, *strange*, and *bottom*. A sixth quark, the *top*, is expected to have a mass of about 165 GeV,[4] and is being sought for assiduously. Each quark has fractional electric charge, and a *strong* charge (called *color*), which can take the values *red* (r), *blue* (b), or *green* (g). Quarks appear to be confined within hadrons, of which there are two kinds: baryons and mesons. Hadronic matter consists of quarks in color-neutral combinations, i.e., a quark and an antiquark (mesons), or three quarks, all of different color (baryons). Two quarks can occupy the same energy state within a hadron, but only if they have different color charges. The *u* (up) and *d* (down) quarks make up essentially all matter that appears in the universe. Protons consist of two *u* and one *d* quark, and neutrons contain two *d* and one *u* quark.

The properties of the three types of force-mediating (spin-one) gauge bosons in the Standard Model are shown in Table 1.2. Although normal gauge theories predict only

massless intermediate vector bosons, mass can be generated by a mechanism known as *spontaneous symmetry breaking*. This mechanism requires the presence of a new spin-zero field, or particle, known as the Higgs, which has yet to be observed.[5]

Table 1.2 Force-Mediating Bosons

Bosons	Symbol	Mass (GeV/c^2)	Color Charge	Electric Charge
Photon	γ	0	0	0
Intermediate Vector Bosons	Z^0	80.22±0.26		0
	$W^{\pm}$	91.173±0.020	0	±1
Gluons	g	0	$r\bar{b}$, $r\bar{g}$, $b\bar{g}$ $b\bar{r}$, $g\bar{r}$, $g\bar{b}$ $\frac{(r\bar{r}-b\bar{b})}{\sqrt{2}}$ $\frac{(r\bar{r}+b\bar{b}-2g\bar{g})}{\sqrt{6}}$	0

1.2.2 Fundamental Interactions in the Standard Model

The experimentally observed interactions are accounted for accurately in the Standard Model. The electromagnetic force has infinite range and follows an inverse-squared law. The infinite range is related to the fact that the force-mediating photons are massless. The weakening of the electromagnetic coupling with distance of separation is explained by higher-order effects such as *vacuum polarization*, which is the screening of electric charge by virtual particle-antiparticle pairs.[5]

The weak force has an extremely short range, and seems to be far weaker than the electromagnetic force (at low momentum transfers). The short range of the weak force can be explained by the large masses of the force-mediating IVBs. The large masses of the W and Z limit the distances they can propagate. At extremely short distance (or large momentum transfers), the electromagnetic and weak forces become comparable in strength. The weakness of the weak force relative to the electromagnetic force in

particle decays is accounted for merely by the momentum-transfer scales of the interactions. The link between the electromagnetic and weak forces provides the basis for unification of the electromagnetic force and the weak force in electroweak theory.

Quarks, bound by the strong color force within a hadron, exhibit the behavior known as *asymptotic freedom*. At extremely close ranges, the strong force seems to have essentially no effect on the binding of the quarks; that is, at large momentum transfers, they appear to be free within the hadrons. As the separation between quarks is increased, however, the force becomes far stronger than for electromagnetic interactions. As the quarks are separated yet more, the potential energy of the system becomes so great that quark-antiquark pairs are generated spontaneously, and form new hadrons. In this way, "free" quarks are never observed. This description of the strong force is used in calculations in perturbative QCD, where extremely close ranges (or, equivalently, extremely high momentum transfers) correspond to small coupling constants in interactions (see Sec 1.3.2).

The surprising result that the strong color force becomes weaker asymptotically is well accounted for in QCD. It has origin in the fact that QCD corresponds to a non-Abelian gauge theory, while QED is Abelian. The non-Abelian nature of the gluon fields allows them to couple (that is, $g \leftrightarrow g + g$), while one photon cannot split into two (even virtually). Thus gluon interactions provide terms that cancel the reduction of coupling at large distances that holds in QED, and, in fact, produce just the opposite effect.

1.3 Testing the Standard Model

Although the Standard Model provides an excellent description of all fundamental processes, it contains many free parameters. Quantities such as particle masses, coupling constants, and mixing angles must be determined experimentally. The Standard Model relates the various parameters, and makes predictions that must be tested thoroughly. Experimental elementary particle physics addresses these issues, and the most important facilities for such tests involve particle accelerators.

1.3.1 Collider Physics

Accelerators are used to investigate fundamental phenomena by colliding particles with either a fixed block of matter (fixed-target experiments) or with other particles that are traveling in the opposite direction (collider experiments). In most accelerators, the primary particles are either electrons or protons; this is mainly because they are stable and readily available. Hadron colliders, such as the Tevatron, offer important ways to explore the validity of the Standard Model.[6] For example, hadron colliders are very well suited for the following possible studies:

1. A comparison of data with QCD predictions at very high transverse momenta.
2. The identification of a heavy top quark and a measurement of the top quark mass.
3. The identification of the triple electroweak gauge coupling through measurement of radiative W decays.
4. Precision measurements of the W mass.
5. Searches for new high-mass particles for investigating physics beyond the Standard Model.

In collisions involving the color force between a proton and an antiproton, a quark or gluon from one scatters from a quark or gluon from the other (Fig. 1.1). The remaining *spectator* partons continue on (although they also participate in the interaction because of the overall need to conserve color and to produce only color-singlet hadrons).

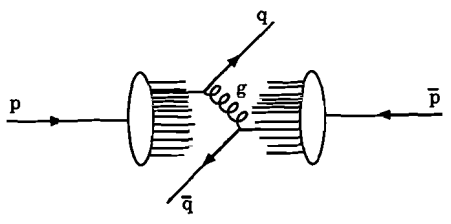

Figure 1.1 Example of proton-antiproton collision involving constituent quarks (q) and mediating gluons (g).

The scattered partons undergo a process known as *fragmentation*, in which they evolve into hadrons. Since fragmentation involves primarily low-momentum transfers,[7] the end result is frequently the production of a *jet* of tightly collimated particles,

with total energy approximately equal to that of the initial parton. Although partons cannot be observed directly, a measurement of the energies of these jets can give a good indication of the parton energies.

Additional gluons or quark-antiquark pairs can be produced before fragmentation occurs, resulting in more jets. The *cross section* of each different final state is basically the probability of seeing that final state. For example, the initial or the scattered parton can radiate a gluon. Such effects usually decrease the cross section for any final state, because each higher-order contribution involves an extra multiplication by the strong-coupling parameter (α_s), and thus the probability of seeing this final state is correspondingly reduced. The cross sections for different processes can be calculated using the electroweak theory or QCD (using a perturbative expansion, see Sec. 1.3.2), and compared to the experimental results. This comparison can then be used to check the validity of the Standard Model or to measure its parameters.

1.3.2 Perturbative QCD

QCD, just like QED, contains a fundamental coupling constant (α_s) in the QCD Lagrangian. The coupling constant in QED (α_{em}) describes electromagnetic interactions, and is a function of distance (or, equivalently, momentum transfer) in such a way that the strength of the electromagnetic force increases as the momentum transfer increases. In QCD, however, the coupling gets weaker as the momentum transfer increases, an effect which (as has been indicated) can be attributed to the self-coupling of the color-charge-carrying gluons.

The QCD Lagrangian, again just as in QED, must be dealt with in terms of a perturbative expansion in the coupling constant α_s in order to provide predictions that can be compared with physical results. Divergent integrals that appear in certain terms of the expansion are *renormalized*, that is, combined into terms such as physical mass and charge of particles.[5] The result is that the 'infinities' are replaced in the theory by finite physical values of these parameters, which are determined experimentally.

Effectively, perturbative QCD applies renormalization through the introduction of a mass or momentum scale Λ that appears in the leading order definition of the coupling

constant:

$$\alpha_s = \frac{12\pi}{\left(33 - 2n_f\right)\ln\left(Q^2/\Lambda^2\right)} \tag{1.1}$$

where Q^2 is the magnitude of the square of the four-momentum transfer in the scattering, and n_f is the number of flavors appropriate to the process in question. The value of Λ, and therefore α_s, must be determined from experiment. Since the perturbation expansion does not converge rapidly for large α_s (that is, low Q^2), QCD is best explored at high energies where high momentum transfers are possible. Additionally, it is useful to select events with large transverse momentum (p_T), because these events correspond to collisions at short distances, and therefore high Q^2.

In the perturbative expansion of QCD, higher-order terms in the cross section correspond to more complex final states. For example, a two-parton final state, which is the simplest possible interaction, is described by the leading-order term in the expansion. Therefore, the cross section for a "two-to-two" scattering is proportional to α_s^2. Several Feynman diagrams of two-parton final-state processes are show in Fig. 1.2.

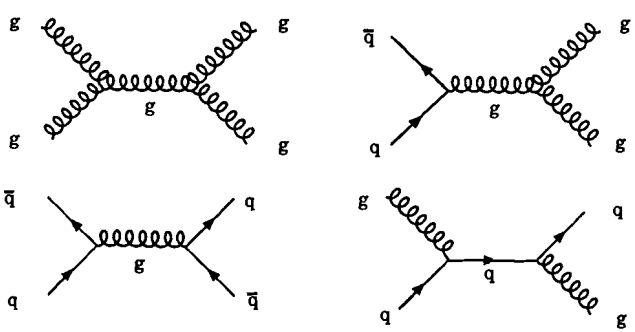

Figure 1.2 Examples of some lowest-order α_s^2 QCD processes

Since each additional gluon coupling in a QCD interaction contributes terms proportional to $\sqrt{\alpha_s}$ in the amplitude, the next-to-leading order (NLO) terms in the expansion (proportional to α_s^3) involve three-parton final states, such as two quarks and a gluon from one of the parent quarks. Increasingly more complex final states are described by increasingly higher terms in the expansion. Several other higher-order processes are shown in Fig 1.3.

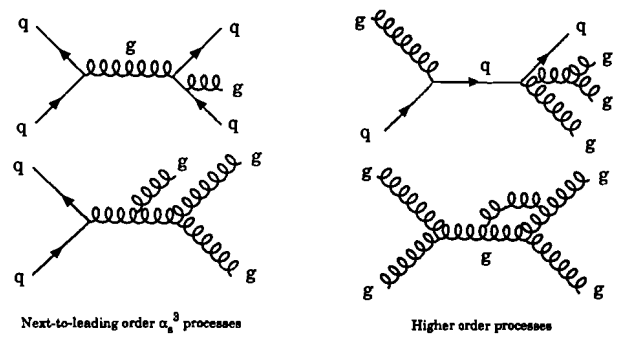

Figure 1.3 Examples of higher order processes

In order to fully test QCD, the theory must be compared with experimental data in the energy regions where the perturbative expansion is valid. Various tests are readily performed at hadron colliders, such as a measurement of the inclusive jet cross section, a measurement of the dijet mass spectrum, multi-jet production, and the longitudinal distribution of jet production.

For example, the two-jet cross section for a fundamental process to be observed at hadron colliders can be written to first order as follows:

$$\sigma(p\bar{p} \to 2\,jets) = \sum_{ab} \iint dx_a dx_b f_{a/p}(x_a, Q^2) f_{b/\bar{p}}(x_b, Q^2) \hat{\sigma}(ab \to 2\,jets) \tag{1.2}$$

Here Q^2 is the magnitude squared of the momentum transferred in the collision, x_i is the fraction of the total hadron momentum carried by parton i at a given Q^2, $f_{i/h}$ is the parton distribution function, which gives the probability that parton i carries a momentum fraction x_i of hadron h, and $\hat{\sigma}$ is the cross section for the fundamental subproc-

ess of the scattering of constituent partons a and b. The sum is over all colors and flavors of quarks and gluons, and the integrals are over the ranges of the x_i. This cross section can be calculated and compared with experimental measurements.

Most of the relevant measurements rely upon accurate determinations of jet angle and energy, and uncertainties in jet production cross sections at hadron colliders are primarily due to limitations in jet energy measurement,[6] as well as from the algorithms used to measure jets. Theoretical uncertainties arise from a lack of knowledge of parton distribution functions, which are usually determined in deep inelastic scattering experiments at low Q^2, and then extrapolated via QCD to the relevant range of kinematics.[8]

1.3.3 Search for the Top Quark

The discovery of the top quark would lend considerable validity to the Standard Model, and finding the top quark is therefore one of the highest priorities in high energy physics. Several experiments have placed quite stringent limits on the top mass.

Electron-positron collider experiments at LEP and SLC have placed limits on the mass of the top quark using the interaction:[9]

$$e^+e^- \longrightarrow Z^0 \longrightarrow t\bar{t} \tag{1.3}$$

and have deduced that the mass of the top is $m_t > 45.8$ GeV/c^2. In addition, combining results from several LEP experiments, and using radiative corrections from the Standard Model, a theory-dependent prediction of the top mass is available at $m_t = 165 \pm 25$ GeV/c^2.[4]

The predominant interaction through which top quarks are expected to be produced at the Tevatron is through the gg fusion process, or a $q\bar{q}$ interaction via an intermediate gluon, as shown in Fig. 1.4.

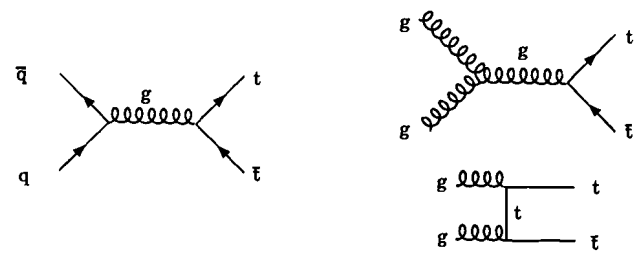

Figure 1.4 $t\bar{t}$ production processes

These processes are observed through:

$$\begin{aligned} p\bar{p} &\rightarrow t\bar{t} + X \\ t \rightarrow bW^+,\ \bar{t} &\rightarrow \bar{b}W^- \end{aligned} \tag{1.4}$$

where X refers to anything else, and where the Ws are real or virtual, depending on the top mass. The bs produce hadronic jets, and each of the Ws can decay into either a charged lepton and a neutrino, or into two quarks (which are seen as hadronic jets).

The mode that yields the cleanest signature involves the leptonic decay of both Ws. Here the backgrounds from QCD are smallest and, since the resolution of most detectors is quite good for charged leptons, they can be easily measured with high precision. This channel is characterized by the presence of two b-jets, two high-p_T charged leptons (ee, $e\mu$, or $\mu\mu$), and missing E_T from the two neutrinos. Unfortunately, the branching ratio for this process is quite low (about 5%), so the yield is small.

A much higher rate (30%) exists for a semi-leptonic decay, or where only one of the Ws decays into a charged lepton and the other into two quarks. This process is marked by two b-jets, 2 quark jets from the W, an isolated high-p_T charged lepton (e or μ), and missing E_T from one neutrino. Unfortunately, the background for this channel, namely W bosons produced in association with jets, is quite high. This background can be reduced by identifying a b-quark in the final state, which would not be prevalent in the jets of the background events. Since the b is identified through its lifetime or its transi-

tion into a lepton, b-detection is highly dependent on the ability to identify charged leptons or short-lived particles. However, because the charged lepton from b-decay usually appears in the middle of a b-jet, this process is only useful when the lepton is a muon; that is, if the jet can be contained in the high-density material of the calorimeter, the muon can then be detected downstream of that. Finally, although the channel wherein both Ws decay hadronically corresponds to 44% of the total rate, the jet combinatorics and the multijet QCD background to this mode is exceedingly large.

Using a combination of the first of the above two channels, CDF has produced the best limit thus achieved on the top mass: $m_t > 91$ GeV/c^2 at a 95% confidence level,[10] assuming couplings of the Standard Model. These results bear out the expectation that hadronic collider experiments at the Tevatron are very well suited for finding the top. With increasing luninosity at the Tevatron, there is hope that this search will soon be successfully concluded.

1.3.4 Searches Beyond the Standard Model

Although the Standard Model is quite successful in describing the phenomena apparent at low energies, it seems unlikely to be the 'ultimate' complete theory. There are several reasons for this:[11] there are too many parameters that must be determined experimentally; there is no apparent reason why the gauge group happens to be SU(3)⊗SU(2)⊗U(1); there is no reason why there are several different gauge couplings, or why the fermion masses have their particular values; etc. Although the Standard Model correlates the experimentally observed features, a more elegant theory would also explain their origin. The search for more complete Grand Unified Theories (GUTs) is an attempt to find a more appealing theoretical solution.

One of the common threads in GUTs is the idea that all forces can be unified at some very high mass scale. At such a scale, the groups SU(3), SU(2), and U(1) could be shown to be merely subgroups of a larger symmetry that would be unbroken at higher energies. In this way, the three forces encompassed in the Standard Model could be unified much in the way the electromagnetic and weak forces have been unified in the electroweak theory. Essentially, the goal of GUTs is to seek a formulation that, at some

mass scale M, has:

$$\alpha_{em}(M^2) \approx \alpha_s(M^2) \tag{1.5}$$

The estimates for this mass scale are much larger than is currently reachable in any foreseen accelerators: typically, the prediction is about 10^{15} GeV/c^2.[12] Ultimately, all four forces (including gravity) might be included in the unification, but that would require a yet higher mass scale.

One of the most popular theories that proposes to provide unification is *supersymmetry* (SUSY). SUSY predicts that every fundamental particle is associated with another whose spin differs from the first by 1/2 unit. Thus, every fermion (boson) has a boson (fermion) superpartner with identical quantum numbers except for spin. This provides a means for canceling divergences in virtual loops for each particle by its SUSY partner, thereby accounting for one of the biggest mysteries in unification, namely the difference between the unifying scale and the masses of the fundamental objects.

SUSY introduces a new quantum number, which is called *R-parity*, with:

$$R = (-1)^{-3B+L+2S} \tag{1.6}$$

where B is baryon number, L is lepton number, and S is spin. R is +1 for natural particles, and -1 for supersymmetric partners (SSPs).[6] Assuming R-parity conservation (which is not required by the theory), an obvious prediction of SUSY is that SSPs must be produced in pairs, all SSPs must decay into other SSPs, and the lightest SSP is stable. If the lowest mass object is weakly interacting (e.g., the photino), then the cross section for events with substantial missing E_T would be observed to be anomalously large.

Since no SUSY partners of the known fundamental fermions or bosons have been observed, there is as yet no evidence for SUSY. The search for SUSY particles is therefore a very important goal of experiments at the Tevatron, and both CDF and DØ are pursuing an active program along these lines. Channels for investigating SUSY at hadron colliders involve multi-jet events from direct production of SSP pairs, and searches for an excess of events with a large amount of missing E_T.[6]

Chapter 2.

Calorimetry

One of the most powerful and versatile types of high-energy particle detectors is the calorimeter. Calorimeters are basically blocks of material in which particles can interact and deposit a fraction of their energy. The deposited energy can be sampled, and thereby provide a measure of the total deposited energy. Calorimeters usually have sufficient depth of material to contain essentially the total energy of an incident hadron.

The DØ detector (which will be discussed in detail in Chapter 3) relies upon calorimetry for measuring energies of jets and isolated electromagnetic showers (produced by electrons, direct photons, etc.). In order to understand the operation and performance of the calorimeter, a test beam was constructed (see Chapter 4) for the primary purpose of studying the energy response and position resolution for both leptons and hadrons, as well as such issues as stability, gain and pedestal variations in individual channels of the calorimeter. This dissertation is focused on using the test-beam data to improve the overall response of the DØ detector to jets. In order to properly interpret and apply the calorimeter signals observed at the test beam, it is important to have a good understanding of the principles of calorimeter detectors. This chapter, which follows closely the development given in Wigmans,[13] presents a general outline of calorimetry and its use in elementary particle physics.

Calorimeters have several properties that make them well suited to experiments at high energies:[13]

1. Sensitivity to the energy of both charged and neutral particles - a feature clearly not obtainable using detectors that rely solely on a magnetic field for energy determination.
2. Particle discrimination from differences in shower development for different kinds of particles.
3. Precision of measurement that improves with increasing energy, a vital feature at the high energies of the Fermilab Tevatron.
4. A calorimeter depth needed to contain showers that increases only logarithmically with energy, so it is possible to construct compact calorimeters that will contain even the highest energies at the Tevatron.
5. No magnetic field required to obtain energy measurements.
6. Flexibility in segmentation that can provide precise position resolution.
7. Fast response times (less than 50 ns) - an issue of great importance at the highest luminosities.
8. Energy information that can be used for on-line selective triggering as well as offline reconstruction, thus increasing data rates and reducing storage of uninteresting events.

Combining the above features, calorimeters can be designed to investigate the most fundamental physics issues. In particular, by surrounding the interaction region with calorimetry, such devices can be used to measure any missing transverse energy that would signal the production of neutrinos or similarly weakly interacting SUSY particles. Also, due to their ability to measure hadronic jets, calorimeters can provide important information about predictions of QCD.

2.1 Interactions Within a Calorimeter

Particles deposit energy within a calorimeter (or within any type of matter) by interacting *electromagnetically* and *hadronically*. Electromagnetic interactions involve the photoelectric effect, Compton scattering, pair production, and ionization, and are characterized by the radiation length of the traversed material. Hadronic interactions are stronger and of short range, involve primarily strong interactions with atomic nuclei, and are characterized by the collision length of the material.

2.1.1 Electromagnetic Interactions

Charged leptons lose energy in matter primarily through ionization and *bremsstrahlung*, or radiation of photons in the nuclear Coulomb field. Photons lose energy primarily through the photoelectric effect, Compton scattering, and pair production. Different effects dominate at different energies, depending on the type of particle and the material that the particle is traversing. The energy dependence of cross sections for interactions of electrons and photons in various types of matter is shown in Fig. 2.1.[14] At high energies, pair production and radiation dominate electromagnetic processes, both of which involve multiplication of electromagnetically-interacting particles.

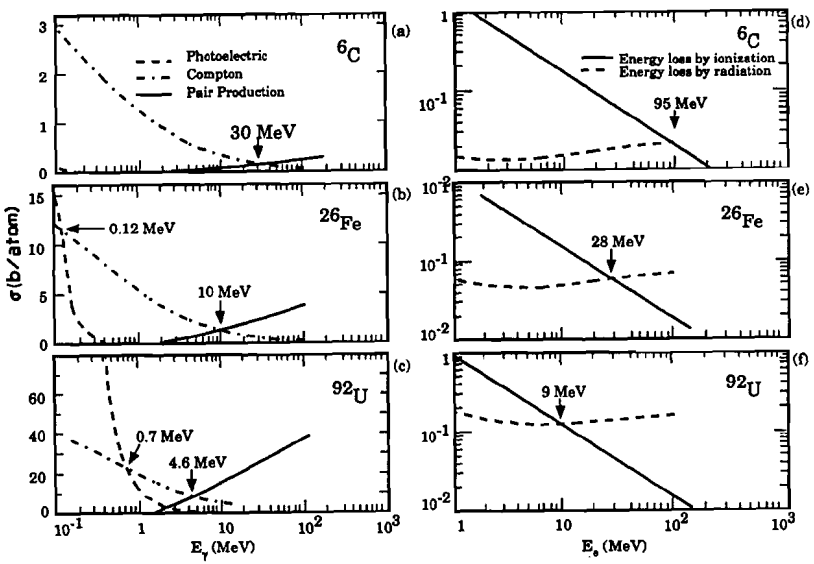

Figure 2.1 Energy loss mechanisms for electromagnetic processes as a function of particle energy. Photon cross sections in carbon (a) iron (b), and uranium (c). Fractional energy deposition by electrons in carbon (d), iron (e), and uranium (f)

Since the dominant energy loss mechanisms for both photons and electrons at high energies involve particle multiplication, these particles produce electromagnetic *showers* as they traverse matter. Thus showers develop until the energy of any particle falls

below the critical energy ε_c, the energy at which the primary energy loss mechanisms change from radiation to ionization loss. That is, as long as the particles within a shower have average energy greater than ε_c, the shower continues to grow both spatially and in particle number. When the average energy of the particles becomes less than the critical energy, the shower begins to diminish as the shower particles lose energy by ionization and eventually come to rest (or annihilate if they are positrons).

Muons with energies below ≈ 1 TeV lose energy mostly through ionization and therefore produce relatively narrow paths of energy deposition in the calorimeters. Energy loss through ionization can be calculated in terms of the mean energy loss per unit path length, or $\langle dE/dx \rangle$, by the Bethe-Bloch formula:[15]

$$\left\langle \frac{dE}{dx} \right\rangle = \frac{4\pi Q^2 e^2 n Z}{m\beta^2 c^2}\left[\ln\left(\frac{2m\beta^2c^2}{\bar{I}}\cdot\gamma^2\right)-\beta^2\right] \tag{2.1}$$

where m is the rest mass of an electron, $\beta = v/c$ is the particle's velocity relative to the speed of light in a vacuum, γ is the particle's Lorentz factor $(1-\beta^2)^{-1/2}$, $Q = ze$ is the particle's charge, Z is the atomic number of the medium, $\bar{I}$ denotes the average energy needed to ionize an atom in the medium, and n is the number of atoms per unit volume. The units of dE/dx are usually described in terms of MeV-cm^2/g, which is obtained by dividing Eq. 2.1 by the density of the traversed material, to obtain a material-independent measure of the energy loss.

The value of $\langle dE/dx \rangle$ for relativistic muons initially falls with increasing energy, and reaches a minimum near β=0.96. At higher energies, $\langle dE/dx \rangle$ undergoes a "relativistic rise", and levels off at about 2-3 MeV/g-cm^2 in most materials.[13] Due to the low rate of energy loss, the depth of material needed to contain muons is very large. Thus, calorimeters are not designed to contain muons.

2.1.2 Hadronic Interactions

Since hadronic interactions are dominated by the strong force, they are much more difficult to predict than electromagnetic interactions. Although the energy deposition

also appears in the form of a shower similar to the electromagnetic case, the scales and complexity are greater. Since the primary energy loss mechanisms depend upon multiple interactions with atomic nuclei (and therefore the mean free path for nuclear collisions), hadronic showers have greater spatial extent, both longitudinally and laterally. Thus, the amount of material needed to contain a hadronic shower is correspondingly greater than for an electromagnetic shower of the same incident energy.

The hadron must undergo an initial strong interaction at some point within the calorimeter in order to start the transfer of its energy. The ensuing shower composition is highly dependent upon the results of this initial interaction, in which the incident hadron's energy is shared among produced hadrons, which can interact again further downstream in the material. However, a significant fraction of the produced mesons decay via the electromagnetic interaction (π^0, η). These particles, along with any photons emitted in nuclear de-excitation, produce more local electromagnetic showers. The shower produced by a hadron consists therefore of a sum of two contributions: a localized electromagnetic part and a more extended hadronic part.

The electromagnetic component of the shower energy is deposited through the same mechanisms as were described in Sec. 2.1.1. The hadronic component, on the other hand, keeps propagating in the calorimeter, with a significant amount of its energy lost through mechanisms that do not produce large signals (ionization energy) in a calorimeter. Also, a fraction of energy is spent in breaking up nuclei, and some is lost in decays of $\pi^{\pm}$ and $K^{\pm}$, etc., into final states involving neutrinos and muons, which leave the calorimeter. The amount of this lost or *invisible* energy can vary greatly from shower to shower. Consequently, not only is the signal for the hadron response smaller than for electrons or photons, but, in addition, fluctuations in the amount of detectable energy cause a degradation in the energy resolution for the response of the calorimeter to the hadronic component (hadronic response) as opposed to the response to the electromagnetic component (electromagnetic response). The ratio of the mean electromagnetic response of the calorimeter to the mean hadronic response is commonly known as e/h.

Figure 2.2 demonstrates two possibilities in the response of a calorimeter to the electromagnetic and hadronic components of a hadron shower. In calorimeters of type

(a), for which e/h = 2.0, the observed energy will be sensitive to the relative fractions of energy in the hadronic and electromagnetic components. Specifically, the energy will differ by a factor of two for showers that are either purely electromagnetic or purely hadronic in nature.

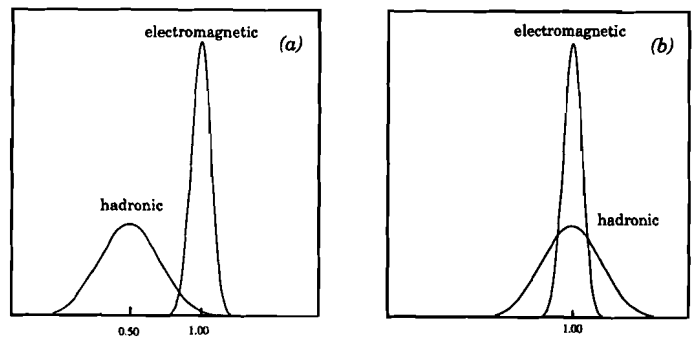

Figure 2.2 Responses of hadronic and electromagnetic components

Consequently, calorimeters that do not have similar response to the two components of the hadronic shower will have a poorer resolution, due to variations in the relative magnitudes of electromagnetic and hadronic components of the shower. However, the energy deposited in calorimeters of type (b) (e/h = 1.0) will on the average be proportional to the sum of the incident energy of the hadron, independent of such variations. Thus, fluctuations in the relative fraction of energy in the two components will produce a degradation in resolution in calorimeters of type (a), but will have a far smaller effect on the resolution in calorimeters of type (b). Therefore, a calorimeter with e/h close to unity will provide better inherent hadronic resolution.

In order to minimize this degradation in resolution, large departures in e/h from unity should be avoided. This can be achieved by selecting materials that have the property of compensating for invisible energy. Such calorimeters, which will be discussed in more detail in Section 2.2.3, are known as *compensating calorimeters*. Compensating calorimeters effectively reduce the difference in the relative responses of the electromagnetic and hadronic components of a shower in a calorimeter. Also, by the

same token, compensating calorimeters reduce the difference in response to electromagnetically interacting particles (such as photons and electrons) and hadronically interacting particles (pions, etc.).

It is important to distinguish between the relative response of a calorimeter to electrons and to hadrons of same energy, as opposed to the value of e/h, which refers to the ratio of the response of a calorimeter to the electromagnetic and hadronic components of a hadron shower. Clearly, because an electron interacts only electromagnetically, the relative electron/hadron response is related to e/h, but it does not have to be the same. When e/h is unity, then the relative electron/hadron response will also be unity; however, when e/h differs from unity, because the electromagnetic and hadronic fractions of a hadron shower can vary, the electron/hadron response will also vary and will usually differ from both e/h and from unity.

2.1.3 Mixed Interactions (Jets)

Since hadrons arise primarily from the fragmentation of constituents, the response of a calorimeter to single hadrons is not as important for hadron collider experiments as the response to a mixture of purely electromagnetically interacting particles and hadrons (as found in a jet). Because a jet is composed of both kinds of particles, the jet energy resolution will be optimal if the response to electromagnetically interacting particles is the same as the response to hadronically interacting particles, which, as we indicated above, would hold if e/h were unity. Studies have shown that the relative electron/hadron response of a calorimeter can have the greatest detrimental effect on jet resolution.[13]

Although jets are conceptually similar to single-hadron showers (because single hadron showers also have electromagnetic and hadronic components), there are two important differences. First, there are fluctuations in the composition of the jet (between hadronic and electromagnetic particles) that are due to the original partonic fragmentation that produced the jet. Since partonic fragmentation cannot be simulated at a test beam, fluctuations in the products of this initial phase likewise cannot be simulated in test beam data (such effects can only be calculated phenomenologically). Second, the mixture of particles in a jet is established at the interaction point, rather than within

the calorimeter's material. This can be used to improve jet resolution through the use of separate electromagnetic and hadronic calorimeter sections, which can be accomplished by designing a front section with enough depth to contain electromagnetic showers, and a subsequent section to contain hadronic showers. The electromagnetic section can be chosen to obtain the best resolution for purely electromagnetic particles within the jet, and the hadronic calorimeter for the best possible resolution for hadronic particles within a jet (recognizing that a substantial portion of the energy of a hadronic shower can be deposited within the electromagnetic section).

2.2 Sampling Calorimeters

There are two main types of calorimeters: *homogeneous* and *sampling*. Homogeneous calorimeters are usually constructed of a single active material, namely material that is sensitive to energy deposition throughout its volume. A lead-glass calorimeter is an example of a homogeneous calorimeter. Sampling calorimeters, of which DØ is a prime example, consist of alternating layers of active material and *absorber*. The absorber, which is usually an extremely dense material such as lead or uranium, generates showers that are propagated and sampled statistically in the active readout material. Since active material is in general much less dense and more expensive than materials such as lead or uranium, the volume and cost of homogeneous calorimetry is often prohibitively expensive, especially for use at high energies. Sampling calorimetry, on the other hand, can be constructed in a compact, efficient manner, allowing a cost-effective method to contain high-energy showers.

The active layers in a sampling calorimeter can consist of any stable material that can be made to ionize or scintillate. Examples include gases, plastic scintillator [polymethyl methacrylate (PMMA), or the polystyrene-based scintillator SCSN38], silicon, the warm liquid tetramethyl pentane (TMP), and cryogenic liquids such as argon or krypton. Although energy deposited in the absorber is completely lost, and the fraction deposited in the active material is small (usually less that 20%), the observed fraction can be predicted to good precision, and thereby used to obtain the overall incident energy.

2.2.1 Energy Measurement in a Sampling Calorimeter

Assuming that the amount of energy detected in the active material bears a linear relationship to the total energy, the total energy of an incident particle can be estimated through Eq. 2.2:

$$E^k = \alpha \sum_i^X \beta_i L_{ik} \tag{2.2}$$

where L^k_i is the signal observed in the ith active readout layer, and X is the number of readout layers in the calorimeter. The *sampling weights* β_i and the scale factor α are described below.

The relative sampling weights β_i in Eq. 2.2, reflect the contribution of the different layers to the energy deposited in the active material:

$$\beta_i = \frac{E^i_{total}}{E^i_{active}} = \frac{E^i_{active} + E^i_{absorber}}{E^i_{active}} \tag{2.3}$$

Here, E^i_{active} is the total energy deposited in the active material, and $E^i_{absorber}$ is the total energy deposited in the absorber material for the ith layer of the calorimeter. E^i_{total} is the sum of the energies deposited in both active and passive parts, which is the total energy deposited in the ith layer. The sampling weights are expected to be inversely proportional to the sampling fractions for energy deposition through ionization ($\langle dE/dx \rangle$), which are found by assuming that all particles are minimum-ionizing (MIPs). This is given essentially by Eq. 2.1 when $\beta \approx 3$. Because of non-linearites in response, these dE/dx weights are only approximately correct for any given calorimeter.

The energy scale factor α for the calorimeter is found by studying the response of the calorimeter to particles of known incident energy, usually in a test beam. After this calibration is established, α is used to convert the readout units (e.g., ADC counts from analog-to-digital converters) to units of energy (GeV).

2.2.2 Energy Resolution of a Sampling Calorimeter

Since the energy in a sampling calorimeter is measured on a statistical basis, fluctuations are expected about the predicted mean response, which contributes to the resolution of the detector. The resolution of a detector is also affected by contributions from, for example, electronic noise, background radiation, and the dependence of response on the nature of incident particles. The ratio of resolution to the mean response can be approximated by the following equation:

$$\left(\frac{\sigma}{\mu}\right)^2 = C^2 + \frac{S^2}{\mu} + \frac{N^2}{\mu^2} \tag{2.4}$$

where σ and μ are the observed standard deviation and mean energy, respectively; C is a *constant term* that corresponds to a contribution from effects such as gain variations in any amplifiers, uncertainty in beam momentum, and any difference in response to electrons and pions; N is an energy-independent *noise term*, with possible contributions from any background radiation and electronic noise; and S is a *sampling term*, representing the contribution from statistical sampling fluctuations. The parameters σ and μ are usually obtained from fits of a Gaussian form to the observed energy distributions at some fixed incident energies. For very high energies, the resolution is often characterized by the sampling term S, although the constant term eventually dominates at highest energies. The noise term, N, being energy-independent, will limit the resolution at low energies.

2.2.3 Compensating Calorimeters

Because hadronic showers involve nuclear breakup, which is an endothermic process, calorimeters generally display a lower response to hadrons than to electromagnetically-interacting particles, and the value of e/h is usually > 1. However, many calorimeters use a technique known as *compensation* to produce a more equivalent response. Compensation can be reached through any combination of three ways:[13]

1. Reducing the response to the electromagnetic component of a shower by varying the amount of active and passive material, or by placing a boundary layer between the absorber material and the active material. The latter can suppress electromagnetic response by absorbing the soft photons produced in the outer layers of the absorber.
2. Increasing the hadronic component of a shower by improving the re-

sponse to neutrons from nuclear breakup. This can be achieved by adding hydrogen atoms into the active medium (e.g., methane).

3. Increasing the response of the hadronic component of a shower by use of a fissionable material such as ^{238}U as the absorber. Low energy neutrons can fission, and produce ionization in the medium.

The third technique is the only one that provides extra energy to the system. Various combinations of active materials in conjunction with ^{238}U produce different effects on the behaviour of e/h. In particular, it has been shown that uranium-liquid argon calorimeters have an e/h ratio that approaches unity with increasing energy ($e/h \rightarrow 1.05$).

2.2.4 Position Resolution of Sampling Calorimeters

The active layers in sampling calorimeters are usually constructed in the form of a grid of readout cells in order to provide position information for incident particles. The precision of position measurement is primarily dependent on the granularity of the calorimeter, the signal-to-noise ratio, and the characteristic width of the showers. The granularity of the readout cells is therefore chosen so as to obtain a resolution consistent with the inherent resolution of the showers that will be seen in those cells. Thus, the very narrow, high-intensity, localized electromagnetic showers require very fine granularity, and provide extremely fine position information (sometimes < 1 mm); while the broad, highly fluctuating hadronic showers have a much poorer position resolution, which often cannot be improved through finer granularity. Given adequate cell granularity, the position resolution of a hadronic or electromagnetic shower is determined primarily by the signal-to-noise ratio, and thus improves with increasing energy approximately as $1/\sqrt{E}$.

The trajectory of an incident particle through a calorimeter is assumed to be the same as the pattern of energy deposition of the shower. The position of the shower in the various layers can be found statistically using algorithms such as a weighted energy mean, or a center-of-gravity. Angular resolution depends on position resolution, and on the number of layers that are combined and read out together. The readout of the longitudinal layers is often limited by purely financial considerations, and at times by the signal/noise ratio.

Chapter 3.

The DØ Detector

DØ is a multi-purpose detector located at the Fermi National Accelerator Laboratory (Fermilab). It has been designed to study $p\bar{p}$ collisions at the Tevatron, at center-of-mass energies of ~ 2 TeV. The DØ experiment completed its initial run in 1993, and a second run is scheduled for 1994. An upgrade is being planned for the late 1990s, in order to take data at the higher luminosities expected after the improvement of the accelerator complex. In this chapter we will describe the main elements of the DØ system.

3.1 Fermilab and the Tevatron

The Fermilab accelerator has been operating in the fixed-target mode since 1972. With the construction of the Tevatron, and the introduction of the collider mode, the energy available in the center-of-mass has been extended to almost 2 TeV. The Tevatron is currently the world's highest-energy particle accelerator, and provides a unique opportunity for studying physics of fundamental interactions at the largest mass scales. A diagram of the accelerator system is given in Fig. 3.1

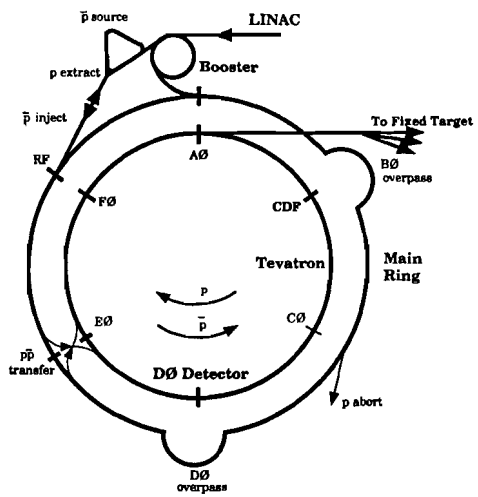

Figure 3.1 DØ and the Fermilab Tevatron

H^- ions are accelerated to 750 KeV in a Cockroft-Walton accelerator. After being boosted to 200 MeV in a 150 meter linear accelerator (the LINAC), the H^- ions are stripped of electrons using a carbon foil just before they enter a booster synchrotron (the Booster) as protons. The booster accelerates the protons to 8 GeV, then injects them into the 1.3-mile diameter Main Ring accelerator. The Main Ring is used to accelerate protons and antiprotons to 150 GeV for injection into the Tevatron, and to provide 120 GeV protons for producing antiprotons.

When producing antiprotons, protons are accelerated to 120 GeV in the Main Ring and targeted in the $p\bar{p}$ source area. There, 8 GeV negative particles are selected and accumulated in the accumulator source ring for the space of several hours, while their phase space is reduced by stochastic cooling.[6] When a sufficient number of antiprotons have been collected and cooled, they are injected back into the Main Ring and accelerated to 150 GeV. After there is a sufficient number of antiprotons, protons are also accelerated to 150 GeV. The protons and antiprotons are then injected into the Tevatron

in six equally spaced bunches, and each bunch is accelerated to the maximum energy of 900 GeV. The Tevatron is located physically just below the Main Ring, and utilizes superconducting magnets to guide the protons and antiprotons.[6] Collisions occur typically at a center-of-mass energy of 1.8 TeV at both the BØ interaction region (CDF experiment) and the DØ interaction region (DØ experiment).

3.2 Specific Goals of DØ

Some of the most important searches that can be performed at a hadron-hadron collider involve the identification and measurement of properties of high-mass particles such as the top quark, as well as precision measurement of the production and properties of the W and Z gauge bosons. As mentioned in Sec. 1.3.3, the best channels for the measurement and identification of the top involve the emission of charged leptons, i.e. electrons or muons. Excellent charged-lepton measurement is important for the precision measurements of the W and Z masses, and accurate measurement of the energy of hadronic jets is vital for testing QCD. Also, in order to detect neutrinos and similar objects, it is necessary to use transverse momentum conservation to identify missing transverse energy (missing E_T) in the detector. Thus, DØ was designed to provide excellent identification of charged leptons, measurement of the energies of charged leptons and hadronic jets, and accurate measurement of missing E_T.

To guarantee a good measurement of missing E_T, DØ was designed to have almost completely hermetic coverage for the measurement of electrons, muons and hadronic jets, with very few cracks or holes. DØ also chose a sampling calorimeter to provide precise electron measurement and accurate measurement of hadronic jets. Since the measurement of jets depends upon the ratio of responses to electromagnetic and hadronic particles (e/h), liquid argon was chosen as the active material and depleted uranium (^{238}U) as the absorber. The high density of uranium permitted the construction of a compact calorimeter. The DØ electromagnetic calorimeter sections have very fine granularity, allowing sub-millimeter position resolution, and fractional energy resolution of about $0.15/\sqrt{E}$, with E in GeV. The hadronic calorimeter sections have the depth needed to contain most jets ($\geq$ 6 interaction lengths), and hadron energy resolu-

tion of about $0.5/\sqrt{E}$. To identify and measure muons, even within high-energy QCD jets, DØ designed a muon system consisting of magnetized toroids and layers of proportional drift tubes surrounding the entire calorimeter.

Being interested primarily in the highest mass scales, DØ chose to design a small tracking system and a compact calorimeter as the most cost-effective way of attaining large coverage of muons and a hermetic calorimeter. Thus, DØ was designed without a central magnetic field, which would aid in measuring the momentum of charged particles, but would require a much larger central tracking system (and thus a much larger calorimeter and muon system).

3.3 The DØ Detector

The DØ detector consists of three main subsystems

1. The Central Tracking System, for tracking charged particles produced in the collision.
2. The Calorimeter System, for providing the energy measurement for all objects contained in the calorimeter (e.g., electrons, direct photons, jets, etc.).
3. The Muon Detection System, for measuring the momenta of muons that leave the calorimeter.

A diagram of the DØ detector is shown in Fig. 3.2. A special subsystem, the intercryostat detector (ICD) has been added to supplement the calorimeters in regions that have large amounts of "dead" material, where energy cannot be read out because of structural design. The combined system provides almost full coverage for the detection of jets, muons, and electomagnetically-interacting particles ($e^{\pm}$,π^0, etc.), with excellent E_T resolution, jet containment, and discrimination between charged hadrons and electrons.

The DØ coordinate system defines the z-axis along the proton beam, the x-axis out from the center of the Tevatron, the y-axis up, the azimuthal angle ϕ, and the polar angle θ is measured from the proton beamline.

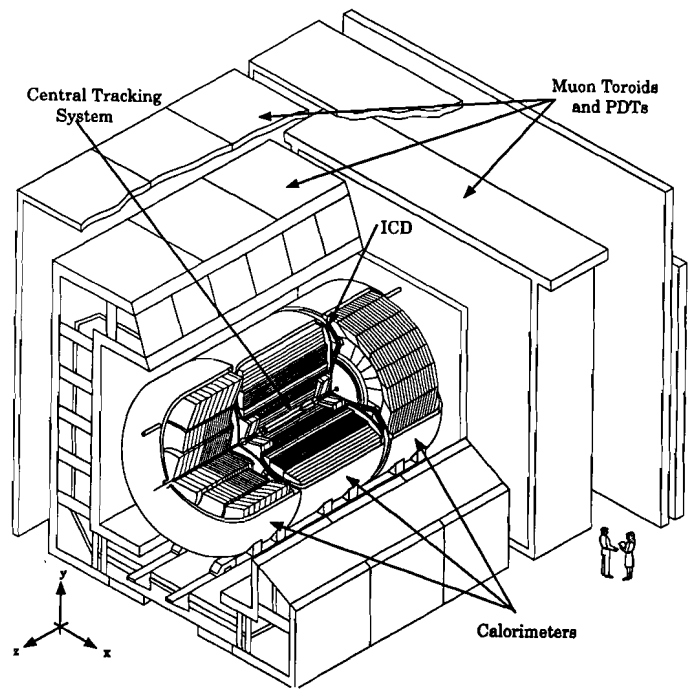

Figure 3.2 The DØ Detector and associated detector systems

3.3.1 Central Tracking

The DØ central tracking system[16] consists of four distinct sections as shown in Fig. 3.3(a): vertex drift chambers, a transition radiation detector (TRD), a central drift chamber (CDC), and forward and backward drift chambers (FDC).

The inner vertex drift chamber[17] contains three supercell layers in the form of cylindrical drift chambers located just outside of the beam tube. A 90% CO_2 and 10% ethanol mixture is utilized as the gaseous ionizing medium. With wires of maximum length of 110 cm parallel to the beam axis, the three layers are held between four carbon-fiber cylinders. The system is designed to have a position resolution of 30-85

μm, and a two-track discrimination at better than 90% confidence for track separations greater then 700 μm.[17]

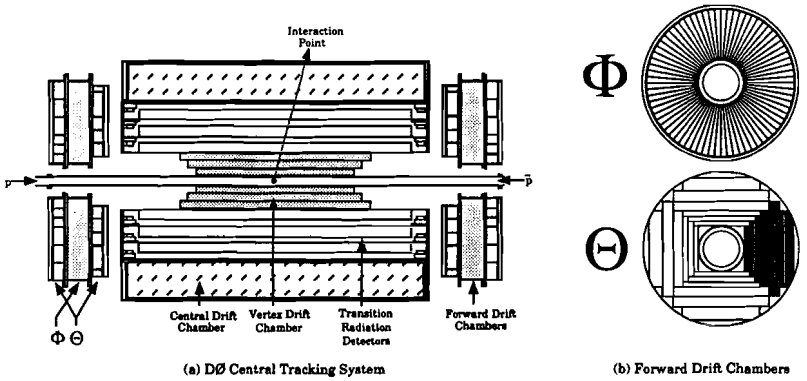

(a) DØ Central Tracking System (b) Forward Drift Chambers

Figure 3.3 DØ central tracking system with FDC cross section

The transition radiation detectors[18] contain polypropylene foils to generate transition radiation X-rays, followed by radial drift chambers, operated with Xe gas, to detect the X-rays. The TRDs provide discrimination between electrons and hadrons for momenta below 200 GeV (pion/electron rejection factor of ≥ 30 for an electron efficiency of 90%).[19]

The central drift chamber has four cylindrical layers, each divided into 32 cells in the (r,ϕ) plane. The basic cells are formed from Rohacell covered with epoxy-coated Kevlar cloth, and wrapped with a double layer of 0.002 in. Kapton.[16] The field shaping electrodes are lines of conductive ink screen (printed onto the Kapton), and are linked internally to resistive dividers. Since each cell contains 7 sense wires and 2 delay lines parallel to the beam direction, each charged particle traversing this chamber can produce signals in 28 sense wires and 8 delay lines. The central drift chamber (which uses a 93% Ar, 3% CO_2, and 4% CH_4 mixture) provides good ionization (dE/dx) measurement to distinguish single electrons from coalescent e^+e^- pairs from photon conversions. The accuracy in the measurement of the axial coordinate of a charged particle trajectory is about 3 mm.

The forward/backward drift chambers[16] are composed of two distinct types of modules. The Φ chambers have 16 layers of 50 cm wires in the radial direction to measure the azimuthal angle, as shown in Fig. 3.3(b). Sandwiching each Φ chamber are two Θ chambers, each with 8 layers of sense wires, with the orientation as shown in Fig. 3.3(b). The two Θ chambers are rotated by 45° with respect to one another. Both chambers use the same gas mixture as in the CDC.

3.3.2 The Muon Tracking System

The DØ Muon tracking system[20] is composed of magnetized iron toroids between layers of proportional drift tubes (PDTs). The PDTs of the wide angle muon spectrometer (WAMUS) and the small angle muon spectrometer (SAMUS), provide an angular coverage to within three degrees of the beam pipe. Fig. 3.4 shows the placement of the muon toroids and PDTs.

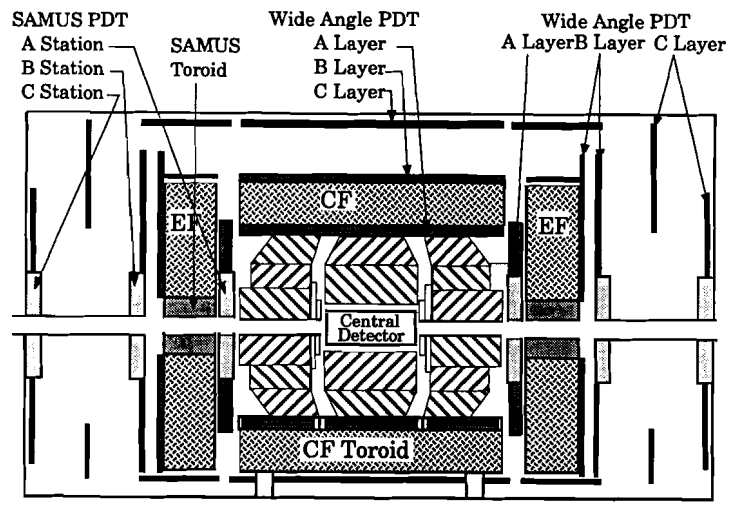

Figure 3.4 Characteristics of the muon system

There are five toroids in the main muon tracking system: one central toroid (CF) and two endcap toroids (EF) for the WAMUS, and two smaller toroids for the SAMUS.

Table 3.1 gives some important characteristics of the toroids.

Table 3.1 Muon Toroid Characteristic

Toroids	Central (CF)	Endcap (EF)	Small Angle
Angular Coverage	$41° \le \theta \le 139°$	$9° \le \theta \le 43°$	$2.5° \le \theta \le 11°$
Z interval (cm)	± 378.5	447.0 - 599.4	447.0 - 599.4
Mean Field (Tesla)	1.9	1.9	1.9
Number of Coils	20	8	4
Turns/coil	10	8	24
Operating Current (Amps)	2500	2500	417
Operating Voltage (Volts)	107	19	13.3
Coil Resistance (mΩ)	42.8	7.5	32

The WAMUS is composed of three main layers of PDT modules, labeled A, B, and C. Layer A is closest to the calorimeters, and measures the trajectory of the incident muon; and layers B and C are beyond the iron, and measure the trajectory of the exiting muon.

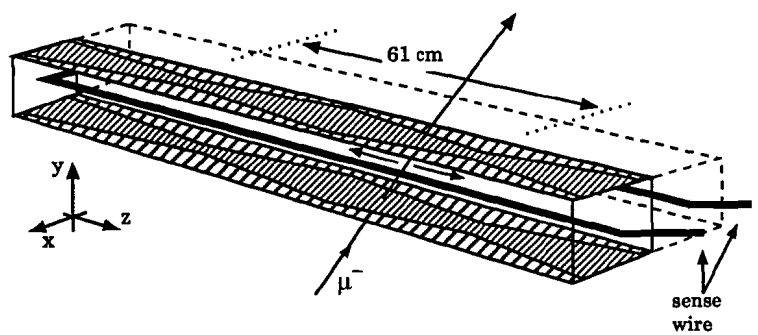

Figure 3.5 Muon WAMUS PDT cell structure, showing sense wire signals and diamond-shaped pattern of verniers pads. The different regions of the vernier pads are read out separately.

Each layer of the PDT module is composed of several decks of rectangular cells: layer A has 4 decks, and layers B and C have 3 decks. Each of the cells consists of an aluminum support structure enclosing a sense wire and two vernier sense pads, and is

operated with 90% Ar and 10% CO_2 as the active gas. Each sense wire goes through the centers of two adjacent cells, as shown in Fig. 3.5. An incident particle will therefore produce two signals in a single sense wire, and the time delay between signals gives an estimate of the particle's coordinate, to within about 10 cm accuracy.

The vernier cathode pads, which are placed on each side of the aluminum structure, are repetitively constructed with a diamond shaped pattern of 61 cm, as seen in Fig. 3.5. The sum and difference of the induced signals on the top and bottom sets of pads are calculated to give the position of the charged particle to about ± 2 mm within each diamond pattern. Thus, the rough coordinate (±10 cm) found from the sense wire identifies the appropriate diamond of the vernier pads, and the pads then provide a resolution to within 2 mm. In the tranverse (x) direction of the cell, position is determined by drift time to the sense wire, to a resolution of ±0.3 mm. The A layer provides a resolution for any particle incident on the iron toroid of about ±0.6 mrad or ±0.1 mm, and the B and C layers together yield a resolution for the exiting particle of ±0.2 mrad or ±0.17 mm.

The SAMUS is similarly constructed of three layers of PDTs, again labeled A, B and C. These PDTs are constructed of stainless steel tubes 30 mm in diameter, each containing a 50 μm sense wire running down their center. The coordinate resolution in a single drift tube is about 0.2 mm. There are three sublayers of PDT modules, each composed of two sub-sublayers of PDT tubes in parallel. Each of the three sublayers is at an angle with respect to the other: the X and Y sublayers are at 90°, and the U sublayer is at 45° to both.

The few "punch-through" hadrons from the calorimeter usually interact in the additional absorber material of the muon system, and therefore the Muon Tracking System helps to further discriminate hadrons from muons (the calorimeters already provide excellent containment, as will be discussed below).

3.3.3 The Calorimeters

There are three main calorimeters in the DØ detector: one central calorimeter (CC) and two end calorimeters (EC). Each of these consists of a set of modules contained in a

separate cryostat, which is filled with liquid argon as an active material (see Fig. 3.6). Each calorimeter contains electromagnetic and fine hadronic compartments that are subdivided into a number of readout layers, and which use depleted uranium for an absorber. There are also coarse hadronic compartments, which use copper or stainless steel. The argon is maintained in a liquid phase using liquid nitrogen as a coolant, and the argon purity is monitored by specialized argon purity test cells, developed by the University of Rochester.[21]

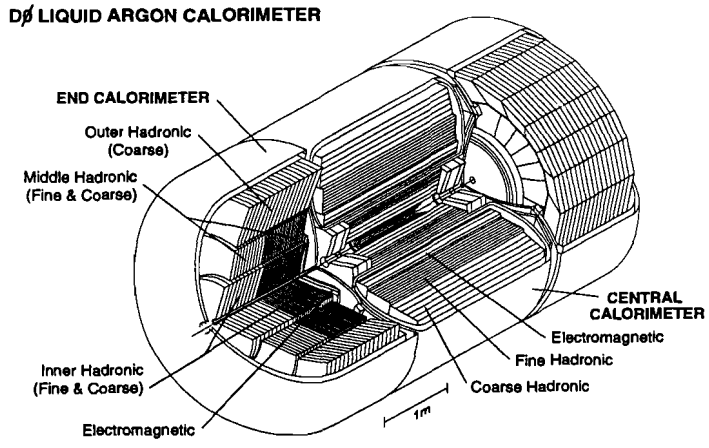

Figure 3.6 Perspective view of DØ calorimeters.

Positions and segmentation in DØ calorimeters are specified according to the azimuth ϕ, pseudo-rapidity $\eta = -\ln \tan(\theta/2)$, and longitudinal depth. The position in ϕ is specified in terms of a new unit of angle measure, which we call a DØ units, which is defined so that 1 DØ unit = $2\pi/64$ radians. We use this unit because it corresponds to exactly 10 readout cells in ϕ, and thus cells can be specifed by an integer coordinate. The calorimeters are composed of *electromagnetic layers*, which fully contain most electromagnetic showers, and *hadronic layers*, which, together with the electromagnetic layers, fully contain most hadronic showers. The various calorimeter layers are composed of separate readout cells, whose transverse size varies with pseudo-rapidity η and

azimuth ϕ to form semi-projective towers with intervals of $\Delta\eta \times \Delta\phi = 0.1 \times 0.1$, as viewed from the interaction point. Therefore, the size of the calorimeter cells changes significantly both with η and with radius, as indicated in Fig. 3.7. The third layer of the electromagnetic sections, which contain the peaks of electromagnetic showers, are subdivided further into 0.05x0.05 in η–ϕ space.

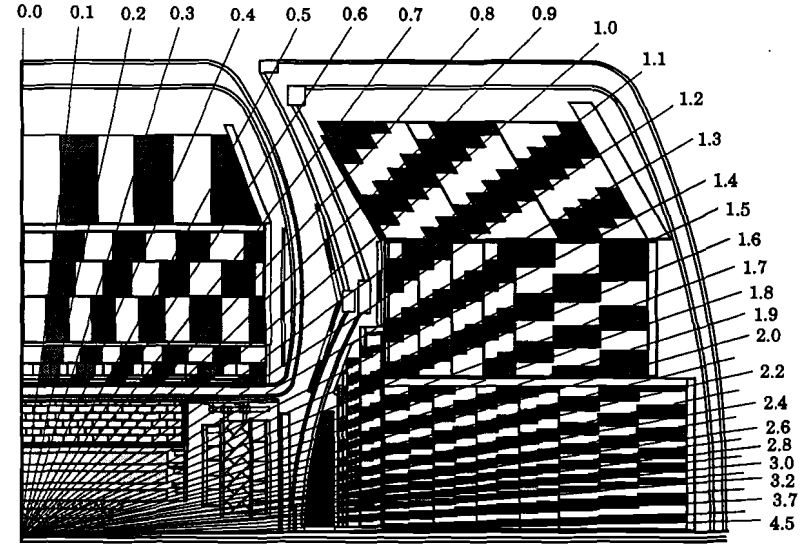

Figure 3.7 Quarter view of DØ detector, indicating the range of pseudo-rapidity of individual cells.

The basic repetitive structure of the calorimeter cell is illustrated in Fig. 3.8.[22] Uranium plates alternate with G-10 signal boards that are plated with a coat of resistive epoxy on the side of the liquid argon, and have a copper plane on the inner side. The uranium absorber plates, which are either 3 or 4 mm thick in the electromagnetic layers, and 6 mm thick in the hadronic layers, are separated by two 2.3 mm liquid argon-filled gaps and a 1.7 mm signal board. The high-resistance coats are maintained

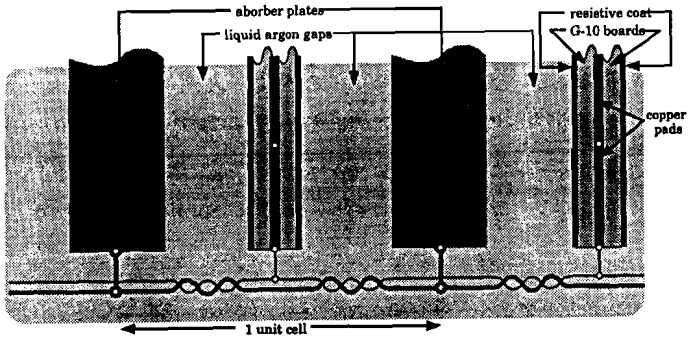

Figure 3.8 Structure of DØ calorimeter cells

at a positive high voltage of about 2000 volts relative to the grounded absorber plate. Incident particles produce free electrons in the liquid argon on both sides of the readout boards. These electrons are attracted to the layer of resistive coating by the high voltage. These currents induce image signals on the copper readout pads, which are then amplified and transmitted to the data acquisition system.

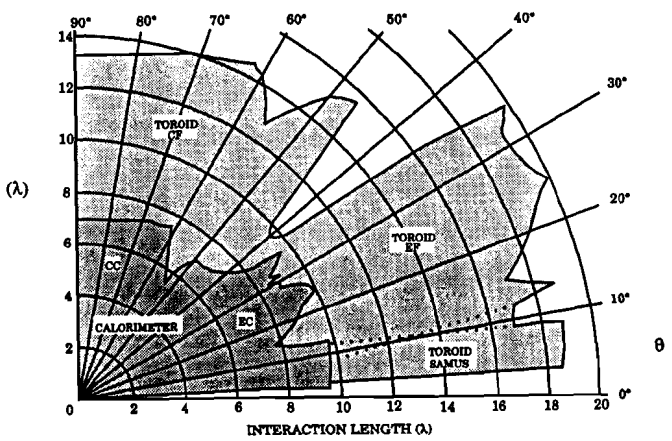

Figure 3.9 Depth of material in the DØ detector as a function of angle from the beam pipe

In order to ensure good jet-energy measurement, the DØ calorimeters were designed to contain most hadronic showers (and thus most jets) that are likely to be produced in 1.8 TeV collisions. A diagram of the amount of absorber material in the DØ detector, including both the calorimetry and the iron in the muon system, is shown as a function of θ in Fig. 3.9, in terms of the interaction length λ (which is the mean free path for inelastic nuclear interactions, a function of the atomic weight of the traversed material).

The central calorimeter (CC) consists of three cyclindrical layers: the electromagnetic (CCEM), the fine hadronic (CCFH), and the coarse hadronic (CCCH). Each of the cylindrical layers consists of wedge-shaped modules. A cross section of the CC is shown in Fig. 3.10. The main ring vacuum pipe goes through one of the CCCH modules (not shown explicitly in the figure.).[22]

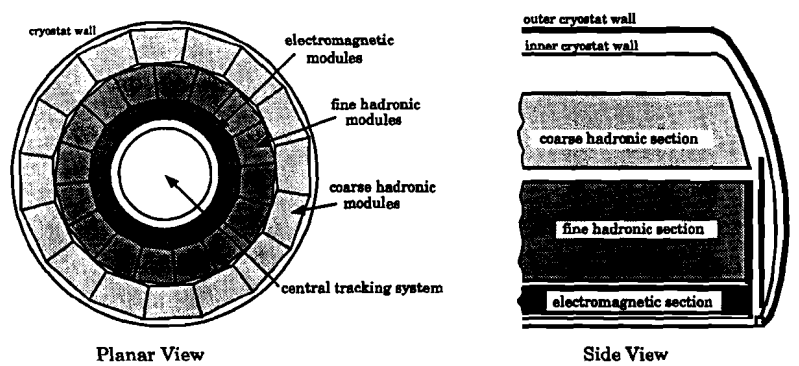

Figure 3.10 The DØ central calorimeter

The CCEM modules contains 20.5 radiation lengths of material in the angular range $35° \leq \theta \leq 145°$, or $|\eta| \leq 1.15$. The absorber plates are formed of uranium plates that are 3 mm thick, 2.6 m long, and 160-200 mm wide. The four longitudinal layers of a CCEM module have 2, 2, 7, and 10 radiation lengths in depth. The CCFH (3.24 absorption lengths thick) and CCCH (2.93 absorption lengths thick), together with the

CCEM, contain a total of 6.93 absorption lengths of material in the angular range $60° \leq \theta \leq 120°$, or $|\eta| \leq 0.55$.

The south and north end calorimeters (ECS and ECN) together extend the region of calorimetry from $\theta = 45°$ to $\theta \approx 1°$ ($\eta = 0.9$ to $\eta \approx 5$), resulting in at least partial acceptance down to about 1° from the beam pipe. The end calorimeter systems consist of four module subsystems, all with azimuthal symmetry: a disk-shaped, finely segmented, electromagnetic calorimeter that is located in front of a central cylindrical inner hadronic module (ECIH), which is within a ring of 16 middle hadronic modules (ECMH). Outside of this is another ring of 16 outer hadronic modules (ECOH). A view of the ECEM is shown in Fig. 3.11:

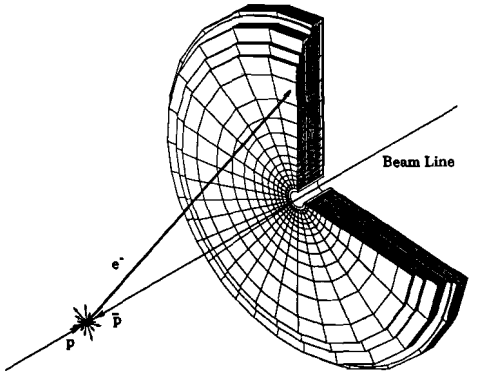

Figure 3.11 End calorimeter electromagnetic section

The ECEMs provide electromagnetic coverage from about 1° to 26° relative to the beamline. The four layers have depths 0.3, 2.6, 7.9, and 9.3 radiation lengths. The first two absorber plates in the ECEM are composed of stainless steel in order to be more sensitive to any "upstream interactions", or showers that are initiated in the cryostat walls (there is about 2 radiation lengths of material in front of the ECs). The remaining absorber plates are all 4 mm thick depleted uranium.

The first four longitudinal layers of the ECIH and ECMH use 6 mm thick uranium

absorber plates, distributed so the layers are 1.3, 1.2, 1.2, 1.2 interaction lengths in depth. The fifth layer uses 46.5 mm absorber plates, which are stainless steel for reasons of economy, for a total depth of 3.6 interaction lengths. The ECOH uses 44.5 mm thick copper plates for absorber, except that, for structural reasons, the first and last layers are made of stainless steel. The ECIH covers the θ range from approximately 1° to 15°, the ECMH from to 15° to 28°, and the ECOH from 28° to 64°. (These ranges are approximate because the modules are designed so that the coverage of each section overlaps that of its neighbors.)

All calorimeter modules are divided into separate longitudinal readout layers: the ECEM and CCEM have four layers (EM1, EM2, EM3, and EM4), the CCFH has three layers (FH1, FH2, and FH3), the ECIH and the ECMH each have five layers (IH or MH 1-5), and the ECOH and the CCCH each have one readout layer. A full cross section of all of the DØ calorimeters and the Central Tracking System, in their relative configurations, is shown in Fig. 3.12. As can be seen, the three calorimeters provide complete coverage almost down to the beam pipe.

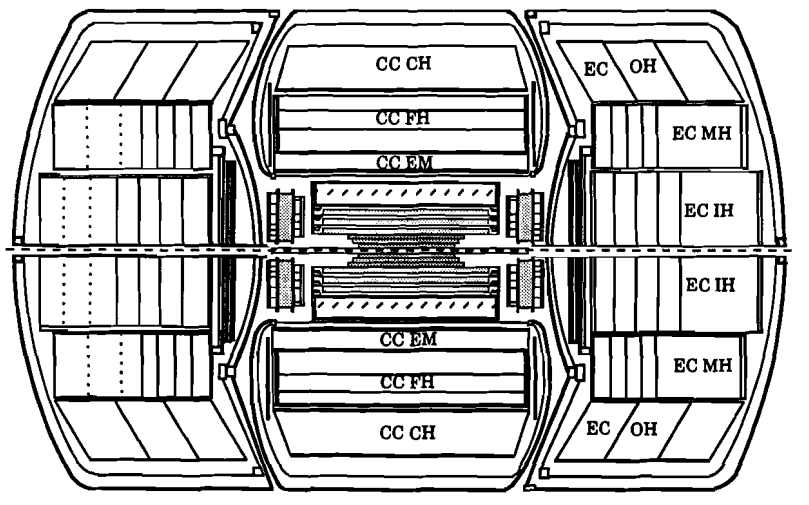

Figure 3.12 A Side View of the DØ Detector. Muon detector not shown.

3.3.4 ICD and Massless Gaps

Between the EC and CC calorimeters, at θ angles of about ±30°, the edges of the cryostat walls present a substantial amount of uninstrumented (inactive) material to any incident particle. Consequently, in order to improve the response of the calorimeters to showers occuring in these regions, additional detectors were added within the calorimeters, as well as between the cryostats,[23] as shown in Fig. 3.13.

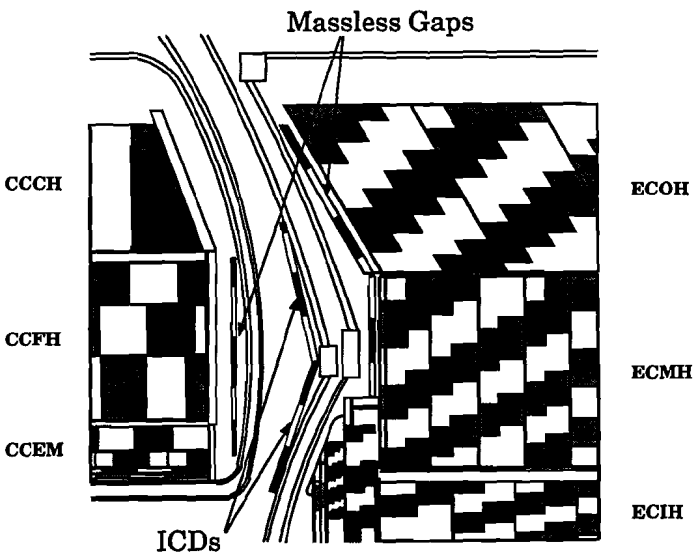

Figure 3.13 Placement of ICD and massless gaps between calorimeters

"Massless gaps" are essentially calorimeter cells (see Fig. 3.8), that have copper-clad G-10 in place of the usual absorber material. Thus, they sample the showers without multiplying them, providing additional information about particles traversing any poorly instrumented region in front of such cells. The ICD is composed of scintillator tiles, located between the EC and CC cryostats. The ICD also provides additional information about particle showers in the region of poor calorimeter resolution, without causing additional shower multiplication.

3.4 Data Acquisition, Electronics, and Triggering

The signals produced in various DØ modules are collected, amplified, converted into digital information, and subsequently analyzed. In addition, some of the information must be examined quickly, and used to 'trigger' on interesting events. All DØ detector systems have separate data subsystems, but this thesis will only describe that used in the calorimeter system.

3.4.1 Electronic System

The signals collected from the cells of the liquid argon calorimeters are transmitted via coaxial readout cables through the interior of the calorimeters to feedthrough ports mounted on the calorimeter walls. After passing through the feedthroughs, the signals are amplified by low-noise charge-sensistive preamplifiers, which are mounted as close to the calorimeter as possible (clustered around the signal feedthroughs on the cryostat walls). Signals from these preamplifiers are then sent to baseline subtractors (BLSs), located on the platform under the detector. The BLSs shape and sample the signals, and provide further amplification. Upon receiving a trigger from the trigger system, the BLS generates a signal for the ADCs (analog-to-digital convertors, located in a counting house outside the interaction region). The signal is then digitized and passed to the data acquisition system.

3.4.2 The Trigger and Data Acquisition System

It is crucial to preselect the desired events, because the total interaction rate at the Tevatron is about 300 kHz, while the data acquisition system can only store events at a rate of about 3 Hz. Since the data storage capacity is far too limited to record events much above this rate, a three-level system of layered triggers is used to reduce the data rate by a large factor. Triggers require an event to meet a set of criteria in order for that event to be accepted. There are three levels of triggering: Level 0, Level 1, and Level 2. The criteria become successively more stringent as the level of the triggering increases.

The Level 0 system[24] consists of two sets of plastic scintillating detectors, placed around the beam pipe in front of the End Cap Calorimeters. The requirement that both

detectors register nearly simultaneous hits allows the selection of events from the collision region. Also, relative timing information between the two detectors can be used to deduce the approximate position of the interaction point. The Level 0 trigger can perform four primary tasks: (1) discriminate $p\bar{p}$ interactions from beam-gas events, (2) measure the approximate location of the collision point, (3) identify multiple interactions in a single event, and (4) monitor the beam luminosity.

The Level 1 trigger[25] combines information from the Level 0 trigger, the muon system, and the calorimeter to provide a fast hardware event selection. The Level 0 and Level 1 triggers together reduce the event rate from about 300 kHz to 130-200 Hz.

The Level 2 trigger is the final software trigger. Events that pass the Level 1 trigger get processed by a farm of about 50 Vax 4000/60s, which apply various algorithms to the data to select events that satisfy certain criteria. For example, the Level 2 trigger can apply a "jet-finding algorithm" to the calorimeter data to require that a jet of a certain mimimum energy be present in the event. The event rate is reduced by Level 2 from 130-200 Hz to the 1-3 Hz, which is low enough for writing to tape. (The Level 2 processing farm has recently been upgraded to use Vax 4000/90s.)

3.4.3 Calibration of Electronics

In order to provide consistent results and to correct data for such time-dependent effects as temperature variations, electronics drift, etc., the electronics channels in DØ are calibrated regularly between the normal data runs.

To acquire information about random noise in the calorimeter, pedestal runs are taken periodically between data runs. These runs are simply sets of data for which there is no trigger selection, and they therefore provide information about electronics and other similar noise present in the calorimeter. The statistical means of the response for each pedestal run are calculated on a cell-by-cell basis, and these means are subtracted from the same cells during later data runs. In this way, a zero response in a cell in a data run corresponds, on the average, to zero energy in that cell. This information is also useful when investigating the resolution of a calorimeter, since the standard deviation of the total response for the pedestal run corresponds to the term N in Eq. 2.4.

In order to ensure that variations in electronics response do not have a detrimental effect on the stability of data runs, gains runs are also periodically taken between data runs. Gains calibration is performed by injecting a known amount of charge into the preamplifiers. Thus, variations in the energy response can be tracked on a cell-by-cell basis. This information is used to normalize all channel responses, and thereby to minimize the effects of any time-dependent variations in the calorimeter system.

3.4.4 Zero-Suppression

Because many cells in the calorimeter have no energy deposited in them, there is no reason to read out every channel in an event. Consequently, in order to minimize the readout time and the size of data banks for each event, DØ implements optional *zero-suppression*. Since all channels contain some finite signal from electronics noise, the zero-suppression process uses the following simple algorithm to select the "empty" cells:

$$|S| \leq n \cdot \sigma \tag{3.1}$$

where S is the pedestal-subtracted signal in the cell, σ is the standard deviation of the noise found from the most recent pedestal run, and n is some arbitrarily chosen constant. Any channel which meets this criterion is not read out. Such a "two-sigma zero-suppression" (with n=2) is the standard mode in which data is taken at DØ. Hence, only large positive and large negative signals are read out for subsequent analysis. (Large negative signals can result from fluctuations due to noise).

Chapter 4.

The DØ Test Beam

Components of the DØ detector and software were tested and calibrated using a charged-particles beam located in the Neutrino fixed-target area of Fermilab (see Fig. 3.1). Tests were made of the data acquisition system and various parts of the central detector and muon system, but the main focus was on the calorimetry.

There were three runs taken over the course of several years in the Neutrino West beamline (NW): a preliminary test of the Central Calorimeter modules was made in 1987 (known as "the 1987 test beam run");[26] a full test of the End Calorimeter modules was made in 1990 (Load 1);[27] and in 1991, a full test of the Central Calorimeters was performed (Load 2).[28] This dissertation is concerned primarily with results found in the run of Load 2.

In the run of Load 2, several modules from the DØ Central Calorimeter and End Calorimeter, as well as simulated versions of the massless gaps and ICD, were placed in a stainless-steel cryostat and submerged in liquid argon. The cryostat was positioned in the NW beam line on a movable table (transporter) in the Neutrino West A (NWA) building. Beams of charged particles of selected energies were directed into the cryostat, and the response of the calorimeter modules was measured. Studies of noise, stability, energy response, and energy resolution were then performed.

4.1 NWA Building and Neutrino West Beamline.

Particles in the Neutrino West beamline are produced by protons extracted from the Tevatron that interact in a fixed target (see Fig. 4.1). Secondary particles are transported down the NW beamline using a set of bending (dipole) magnets, and are focused through several groups of quadrupole magnets. Two energy modes were available for Load 2: a high-energy mode, which produced e^-, π^-, and μ^- at momenta from 7.5 GeV/c to 150 GeV/c; and a low-energy mode, which produced the same particles at momenta of 2-10 GeV/c. Fig. 4.1 provides a sketch of the NW beamline in its high-energy configuration.

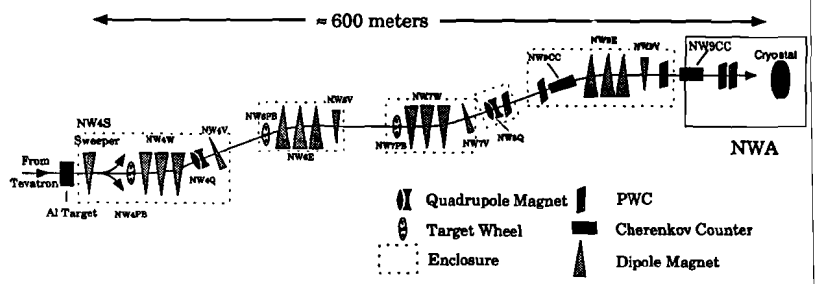

Figure 4.1 NW Beamline

The sweeper magnet (NW4S) is used to select the type of beam that eventually reaches the cryostat. For electrons, the sweeper is set to deflect all charged particles from the beam, leaving mainly photons, which are then converted to electrons and positrons in a lead plate (NW4PB) located immediately downstream of NW4S. When the sweeper is turned off, any electrons from the initial interaction are subsequently filtered out of the beam using thin lead sheets (NW6PB and NW7PB), leaving primarily π^- and μ^- to be transported further downstream. Energy and charge selection takes place using a string of bending magnets, NW4W. The strength of the magnetic field in NW4W can be adjusted so that only negatively-charged particles of a specified momentum continue down the beamline. The remaining dipole magnets remove some of the momentum dispersion caused by NW4W, and steer the beam to the NWA enclosure.

The quadrupole magnets are used to maintain the beam's focus along the way. The field strengths of all magnets (downstream of the NW4 enclosure) and the positions of all target wheels can be controlled by EPICURE, a convenient on-line control system,[29] which is used to tune the beam.

The beam configuration as shown was modified somewhat to accommodate the low-energy mode, but the basic structure of the beamline was still as given in Fig. 4.1.[30] Since pions produced at the initial interaction point (in NW4) must travel about 600 m to reach the cryostat, many low-momentum pions (< 5 GeV/c) do not survive this distance. It was therefore decided to provide a low-energy pion source at a point closer to the cryostat. To accomplish this, a beryllium target was placed in an enclosure about 40 meters upstream of the cryostat (in front of enclosure NW8). High-energy pions incident upon this target produce a spray of lower-energy pions, which are momentum-selected by an additional dipole magnet placed in NW8. With this arrangement, pions of momentum down to 2 GeV/c were studied in the cryostat. However, it was not possible to obtain a pure beam of either pions or electrons. Rather, a mixed beam of charged particles was used, and pions and electrons were selected on an event-by-event basis in the off-line analysis (primarily through the use of Cherenkov counters).

The position of the beam is monitored by proportional wire chambers (PWCs) placed along the beam line, as well as in the NWA building. PWCs are also used to provide precise tracking and momentum information for beam particles on an event-by-event basis. In particular, the beam trajectories are measured both upstream and downstream of the final bend magnet (NW9W) and, along with its field strength, provide an accurate measure of the momentum. The statistical uncertainty on the PWC momentum measurement is estimated at ±0.25%, based upon the wire spacing, bend angle, and distance of the chambers from the bend point.[31],[32],[33] Systematic corrections to the beam momentum are estimated as < ±0.2% for Load I, and < ±0.5% for Load II.[32] These corrections are due to later discovery of survey errors and magnetic field uncertainties, and are not taken into account for this analysis. The total uncertainty on the momentum from the PWCs is < 0.75% for both Load I and Load II. Threshold Cherenkov counters are also available to provide discrimination between μ^- and π^- particles.

4.2 Test Beam Cryostat and Transporter

The test beam cryostat is a stainless-steel cylinder, approximately 3 m in diameter and 5 m long (see Fig. 4.2). To simulate the various angles at which particles from $p\bar{p}$ interactions would impact the DØ calorimeters, the cryostat is rotated and translated about the incident beam using the test beam transporter. The transporter (which is described in detail in Appendix A) uses a system of computer-controlled motors to move the cryostat in four degrees of freedom: translation (east-west, transverse to the beamline), elevation, rotation (about a vertical axis) and rocking (about a horizontal axis through the long axis of the cryostat cylinder). A sketch of the test beam cryostat and transporter is given in Fig. 4.2.

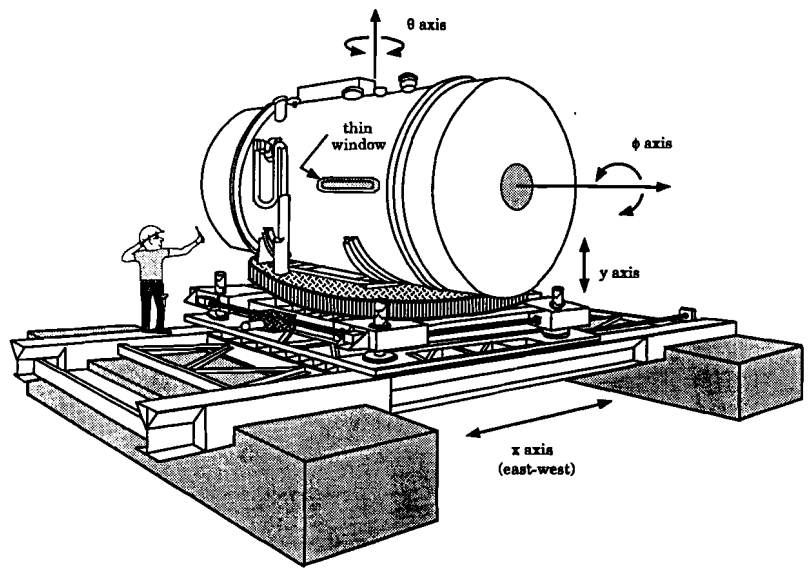

Figure 4.2 Sketch of test beam cryostat and transporter

The cryostat is positioned by the transporter so that the incident particle beam always enters through a thin "window" (constructed of 2 layers of 0.16 cm stainless steel, which is about 5 times less absorber material than obtains for the rest of the steel-

walled cryostat). The transporter moves the cryostat through its various degrees of freedom so that the incident beam simulates different entry angles and positions expected for particles emanating from the DØ collision region. The location of the cryostat is determined with "string-eaters" (encoder devices that measure the displacement along each axis), and these displacements are correlated with known survey information to predict the impact point of the beam upon the modules. Additional information about the impact point is provided by PWC planes mounted on the side of the cryostat (not shown in Fig. 4.2) directly in front of the thin entry window.

4.3 Load 2 Test Beam Configuration

Since the main purpose of the Load 2 run was to investigate the performance of the DØ central calorimeter (CC) modules, a number of central calorimeter modules were placed in the Load 2 cryostat. Because of the coupling between different parts of the DØ detector, portions of the EC calorimeters were included in the tests, along with a rough simulation of the Inter-Cryostat Detector. Fig. 4.3 indicates the region of the DØ detector simulated in the Load 2 test run.

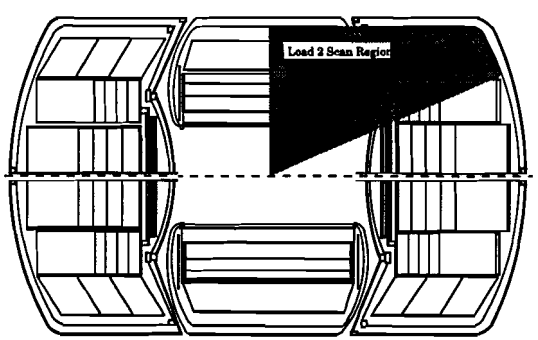

Figure 4.3 Calorimeter modules in Load II test beam

The calorimeter modules were placed in the cryostat in a geometrical configuration similar to that used in the DØ detector. A sketch of the end and top views of the cryostat containing the modules is shown in Fig. 4.4. (The "excluder" consists of low-density

material and other elements that simulate the amount of material expected from the Central Detector and cryostat walls at DØ in front of the modules). It should be noted that the two views shown in Fig. 4.4 are rotated about the beam line with respect to each other.

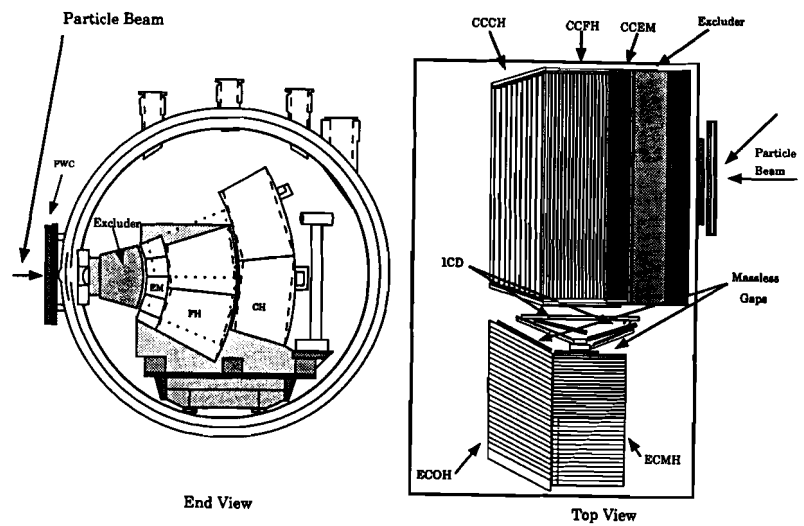

Figure 4.4 Top and end views of the Load 2 configuration

Although the electronics, data acquisition system, and physical configuration of the modules were nearly identical to that in the DØ detector, there were nevertheless several minor differences:

1. The ICD was of necessity submerged in liquid argon, rather than residing at room temperature outside of the cryostat.
2. The volume occupied by the Central Detector at DØ was emulated using a Rohacell excluder, in order to ensure that this large space was not filled with liquid argon, which would initiate showers differently than expected in the experimental configuration at DØ.
3. Cryostat walls were simulated by 0.5" stainless steel plates placed in the appropriate locations. These plates did not have the curvature found in the CC cryostat walls, but were of same thickness.
4. Due to space restrictions caused by the simulated planar cryostat walls, the geometry of the test beam ICD was required to be some-

what different than that for DØ.[23]

5. While the signal cables within the cryostat were the same length as those in DØ, the cable between the preamps and BLSs were longer in the test beam. However, the resulting difference in capacitance was corrected for in the calibration procedure.

4.4 Data Taken at the Test Beam

The test beam data used in this thesis consists of a group of *energy scans*. An energy scan is a set of data runs taken with the particle beam directed at a specified equivalent DØ position in the test beam cryostat, where the energy of the incident beam is varied across the range of available energies. Specifically, two types of energy scans were implemented: *high-energy energy scans*, taken in the high-energy mode at momenta 7.5, 10.0, 15.0, 20.0, 25.0, 30.0, 40.0, 50.0, 75.0, 100.0, 125.0, and 150.0 GeV/*c*, and *low-energy energy scans*, taken in the low-energy mode at momenta 2.0, 2.5, 3.0, 4.0, 5.0, 7.5, and 10.0 GeV/*c*. High-energy energy scans were taken separately for electrons (e^-) and pions (π^-), and a limited number of μ^-. Low-energy energy scans were taken with a mixed-particle beam of e^-, π^-, and μ^-.

Data were taken over effective coordinates ranging from η=-0.5 to η=2.0, and ϕ=3.05 to ϕ=3.42 DØ units (or ϕ=2.99 radians to ϕ = 3.36 radians, since 6.4 DØ units = 2π radians, as explained in Sec. 3.3.3), assuming interactions at the center of DØ. The limits in η were caused by the acceptance of the modules included in the cryostat, and in ϕ by limits on the motion of the transporter (see Appendix A). In addition, data was taken for several trajectories assuming the interaction vertex in DØ was shifted by ±30 cm. Only a subset of the total data sample, consisting of the high-energy and low-energy scans taken at two coordinates as specified in Table 4.1, is used for this thesis.

Table 4.1 Test Beam data incorporated in this thesis

Set	Mode	η	ϕ	particle type
1	high-energy	0.05	3.16	π^-
2	high-energy	0.45	3.16	π^-
3	high-energy	0.05	3.16	e^-
4	low-energy	0.05	3.16	e^-,π^-,μ^-

High-energy hadron data at both pseudo-rapidities (sets 1 and 2) will be used in Chapter 5, and all data at η=0.05 (sets 1, 3, and 4) will be used in Chapter 6. Muons are not used in this analysis. Each data run consisted of 1,000-10,000 events taken at each nominal incident beam momentum P_{nom} (determined by the setting of beam magnets), and measured to high precision using the PWCs. The accepted events are restricted in the offline analysis such that:

$$\left|\frac{P_{PWC} - P_{nom}}{P_{nom}}\right| \leq 0.05 \tag{4.1}$$

where P_{PWC} is the measured momentum of the incident particle using the PWCs. Thus for the accepted events, the spread in incident momentum about the nominal value was less than 5%. For each event, the energies reconstructed in the calorimeter were normalized to the momentum from the PWCs as follows:

$$S^k_{meas} = \frac{P_{PWC}}{P_{nom}} \cdot S^k_{uncorr} \tag{4.2}$$

where $S^k{}_{uncorr}$ is the signal observed in cell k of the calorimeter, and $S^k{}_{meas}$ is the normalized signal for the same cell. This normalization procedure assumes that any nonlinearities in detector response will be negligible for the < 5% spread in incident beam momentum for any given run. The net effect of implementing this correction is that the width of the energy distribution for data taken at some nominal value P_{nom} will reflect only the resolution of the calorimeter and not the inherent spread in the energies of the beam particles.

The data were analyzed using a modified "ICD micro-dst" format,[34] in which data from the calorimeters is processed using the standard DØ software, and then written into unformatted Fortran files on a cell-by-cell basis. All known corrections were made directly to the input data, including cell-by-cell corrections for plate thickness (obtained from survey data of the module structure), gain corrections (TB90L2_GAINCORR),[35]

and capacitance corrections (due to the difference in cable lengths between the test beam and in DØ). The micro-dst format offers an exceedingly compact data set, which results in very fast processing time and reduced storage space. The basic micro-dst format was modified for this analysis in order to further improve accuracy and efficiency of analysis, through the following changes:

1. Observed signals in the calorimeter were reconstructed, gain-corrected, and extracted into an unformatted Fortran file, without pedestal subtraction.
2. Inspill pedestals (accumulated during data taking) for each run were processed to extract the mean μ and standard deviation σ for each channel.
3. The value of μ was then used to perform basic pedestal subtraction, instead of using the means from the standard pedestal runs. (This was done to avoid known program errors in the default test beam pedestal subtraction process, which were corrected subsequent to the test beam run.)

In addition, the data taken at η=0.05 that are used in this thesis were first incorporated in a Test Beam Particle Library (which will be discussed in Chapter 6, and are explained in detail in Appendix B), and then the Particle Library was used to supply the data used for analysis at that coordinate.

Typical reconstructed energy distributions for test beam data taken at η=0.05 and ϕ=3.16 DØ units (3.10 radians) are shown in Fig. 4.5 for both π^- and e^- beams. Included in the figures is information about the distributions: number of events, the statistical mean, and the standard deviation (RMS). Also included are the parameters of a fit to the distribution of the form:

$$f(E) = C\,exp\left[-\frac{1}{2}\left(\frac{E-\mu}{\sigma}\right)^2\right] \tag{4.3}$$

which is a Gaussian (or *normal*) distribution, with mean energy μ and standard deviation σ.

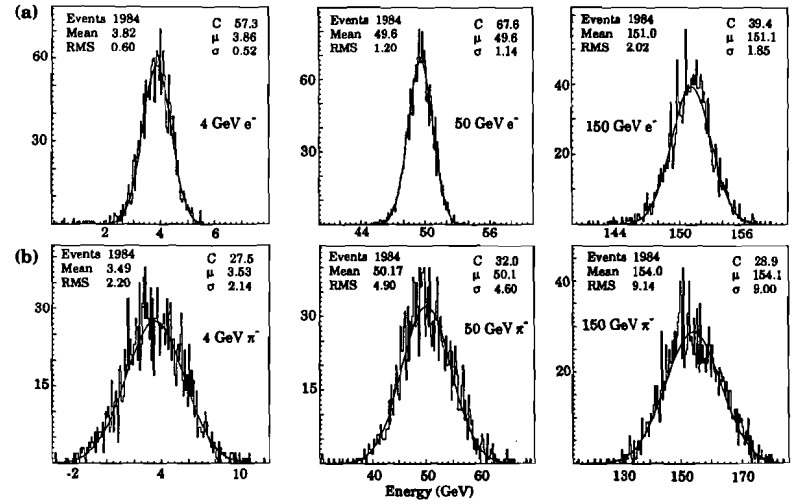

Figure 4.5 Reconstructed energy distributions for (a) e^-, and (b) π^- for a representative set of incident energies in Load II at η = 0.05 and ϕ = 3.16 (3.10 radians)

Chapter 5.

Optimization Of Hadronic Sampling Weights Using Single Particles

This chapter presents a discussion of the sampling weights used for reconstructing energies of hadronic showers in the DØ calorimeter. The weights are chosen with the goal of improving the response of the DØ detector to jets in the central calorimeter. The purposes of this chapter are fourfold. First, we describe an appropriate optimization technique that is intended to improve the resolution of the response of the DØ detector to single-particles by varying the sampling weights of the various DØ calorimeter layers. Second, without considering the detailed structure of jets, we discuss constraints that can be imposed upon the optimization of the response to single hadrons, that can lead to an improvement in the overall jet resolution. Third, we perform optimizations, applying the chosen restrictions, in order to gauge their impact on single-hadron resolution. Finally, we examine if the restricted optimization produces single-hadron response that will, in fact, provide improved resolution for jets relative to that obtained using essentially default (dE/dx) weights.

The data used for this purpose consist of two high-energy scans, both at an azimuth

of ϕ=3.16 (3.10 radians), and at the pseudo-rapidities of η=0.05 and η=0.45 (ϕ = 3.10 radians throughout this thesis, so it will usually not be specified). Since processed low-energy data (from 2-5 GeV) was not available for η=0.45, only high energy data (7.5-150.0 GeV) was used for the analysis in this chapter.

5.1 The Process of Optimizing Sampling Weights

The sampling weights and scale factor for the CC were obtained from the test beam using the following steps.

1. An initial estimate of the relative energy deposited in the various layers was found by choosing a set of default weights, which are inversely proportional to the dE/dx sampling fractions. (These weights are referred to as *dE/dx weights*).
2. An initial estimate of the scale factor α was found by normalizing the observed response of the calorimeter to electrons at 100 GeV.
3. A set of optimized electron weights was found for the electromagnetic layers of the CC, using the full range of energies for data at η=0.05, η=0.45, and η=1.05.[36]
4. A set of optimized weights for hadrons was then found by optimizing the hadron response, subject to certain constraints imposed with the goal of improving jet resolution.

This chapter is concerned with Step 4 of this process, that is, with determining the weights for the hadronic layers that can provide the best jet resolution. In this section, we describe a suitable procedure for use in the optimization of sampling weights for electrons, hadrons, and jets. This optimization procedure is identical to the one used for extracting electron weights.[36]

The hadron data from the test beam consist of data taken at different energies and positions in the calorimeter (as described in Sec 4.4). For any particular event k in a data set, we can write, as in Eq. 2.2:

$$E^k = \alpha \sum_i^X \beta_i L_{ik} \tag{5.1}$$

here, again, X is the total number of longitudinal layers of the calorimeter, α is our conversion factor from ADC counts to GeV, β_i are the sampling weights, L_{ik} are the ob-

served signals in ADC counts in the various calorimeter layers for event k, and E^k is the reconstructed energy for event k.

To compensate for any possible energy-independent offsets to the overall energy scale, a constant δ can be introduced as an *ad hoc* parameter in Eq. 5.1.

$$E^k = \alpha \sum_i^X \beta_i L_{ik} + \delta \tag{5.2}$$

Such an offset is only useful in examining individual particles, as when, for example, dealing with single electrons. For studies of single hadrons, this offset will be set to zero, since a non-zero offset will be difficult to use for reconstructing jets. Nevertheless, we introduce this offset into the formalism in order to maintain consistency with the procedure used to obtain single-electron weights.[36] Also, the offset will be used in studies of optimization of jet energies in Chapter 6.

For simplicity, α can be incorporated into the βs to get new sampling weights $\gamma_i = \alpha\beta_i$. Also, δ can be defined as a $(X+1)^{st}$ layer, with $\gamma_{X+1} = \delta$, and $L_{(X+1)k} = 1.0$. Thus, δ will have units of GeV, and γ_i will have units of GeV/ADC counts. Finally, for any incident energy, we can write:

$$E^k = \sum_i^Y \gamma_i L_{ik} \tag{5.3}$$

where Y is the number of layers + 1.

The parameters γ_i are obtained by minimizing the following χ^2 function with respect to the γ_i:

$$\chi^2 = \sum_{k=1}^T \frac{(E^k_{inc} - \sum_{i=1}^Y \gamma_i L_{ik})^2}{(\sigma^k_{inc})^2} \tag{5.4}$$

here E^k_{inc} is the known incident energy (obtained from PWC information), and the sum

is for all T events included in the optimization (it can be limited to a single energy set, or to events from different energies and calorimeter positions). For σ^k_{inc} we use approximate values for S, N, and C from Eq. 2.4:

$$\sigma^2_{inc} \simeq S^2 E_{inc} + C^2 E^2_{inc} + N^2 \tag{5.5}$$

S is typically 0.50 for hadrons and 0.15 for electrons, and C is typically 0.04 for hadrons and 0.01 for electrons. N is determined by the pedestal noise (primarily due to radiation emitted by the uranium absorber) at the appropriate location in the calorimeter, and is approximately 1.6-2.0 GeV. For this analysis, N is determined from inspill pedestals at the appropriate calorimeter positions.

The χ^2 can be minimized using a fitting routine that varies the parameters in small steps (as found in the CERNLIB software libraries),[37] or, instead, the parameters can be found directly by taking the partial derivatives of the χ^2 with respect to the γ_i and setting them to zero, as shown:

$$\frac{\partial \chi^2}{\partial \gamma_j} = -2 \sum_{k=1}^T \frac{1}{(\sigma^k_{inc})^2} \left[E^k_{inc} - \sum_{i=1}^Y \gamma_i L_{ik} \right] L_{jk} = 0 \tag{5.6}$$

First, considering the sum over k, we can take an average of Eq. 5.6 over all events, and obtain:

$$\left\langle \frac{E_{inc} L_j}{\sigma^2} \right\rangle = \sum_{i=1}^Y \gamma_i \left\langle \frac{L_i L_j}{\sigma^2} \right\rangle \tag{5.7}$$

where the products of all variables within the brackets in Eq. 5.7 are averaged over all the T events.

If we define a correlation matrix $M_{ij} = \langle L_i L_j / \sigma^2 \rangle$, we can solve for the weights γ_j as

follows:

$$\gamma_i = \sum_{j=1}^{Y} \langle \frac{E_{inc} L_j}{\sigma^2} \rangle (M^{-1})_{ij} \tag{5.8}$$

Finally, the parameters for Eq. 5.2 can be extracted from the γ_i, and used to calculate the total energy observed in an event (the *reconstructed* energy):

$$E_{obs} = \alpha \sum_{i}^{X} \beta_i L_i + \delta \tag{5.9}$$

Uncertainties on the weights can be found by calculating the second derivative of χ^2 with respect to γ_k, diagonalizing the resulting matrix (D_{ij}) to find the eigenvalues λ_i, and finding the uncertainties $\Delta_i = 1/\sqrt{\lambda_i}$. Upon taking the derivative of Eq. 5.6 with respect to γ_m, we find that $D_{mj} = 2M_{mj}$. However, due to correlations between the energy deposited in the various layers, just the diagonal uncertainties are of little use in evaluating the results of an optimization. Instead, the resolution on the reconstructed energy provides the best indication of the results of the optimization.

A simple modification of Eq. 5.4 provides a flexibility to fix certain of the weights in the optimization and allow others to vary. We can write:

$$\chi^2 = \sum_{k=1}^{T} \frac{(E_{inc}^k - \sum_{j=1}^{F} \psi_j L_{jk} - \sum_{i=1}^{V} \gamma_i L_{ik})^2}{(\sigma_{inc}^k)^2} \tag{5.10}$$

Here F is the number of number of layers with fixed weights, and V is the number of layers that are varied. The resultant solution for the varied weights is similar to what we obtained before:

$$\gamma_i = \sum_{j=1}^{V} \langle \frac{(E_{inc} - E_{fix}) L_j}{\sigma^2} \rangle (M^{-1})_{ij} \tag{5.11}$$

where E_{fix} is the mean energy deposited in the layers with the fixed weights, which is related to the sum over F in Eq. 5.10.

This optimization technique finds sampling weights based upon correlations between the energy deposited among the various layers. It is equivalent to using a 1-dimensional H-matrix approach.[38]

5.2 Restricting the Optimization of Hadronic Weights to Produce the Best Jet Resolution

To provide a set of sampling weights for the CC hadronic layers that provide the best possible jet response, the following assumptions were incorporated in the analysis:

1. Because electromagnetically and hadronically-interacting particles cannot be distinguished within a jet, the weights must be chosen to be independent of particle type.
2. Because the energies of particles within a jet cannot be measured individually, the weights must be independent of the energies of the particles in a jet.
3. Because the locations and trajectories of particles within a jet cannot be measured individually, the weights should not depend upon the trajectories of particles within the jet.

To make the weights independent of particle type within a jet, a decision was made to choose the weights so that the response to electrons was optimized, even at the possible expense of hadron resolution. The rationale for this was that, since the fractional electron energy resolution is far better than the hadronic energy resolution (at best, $0.15/\sqrt{E}$ vs. $0.4/\sqrt{E}$), a small change in the sampling weights for the electromagnetic layers could result in a big change in the electron energy resolution, but would result in only a slight improvement in the hadron energy resolution. (The actual effect of this restriction upon hadronic energy resolution will be investigated later in this chapter.) Since electrons deposit almost their entire energy in the electromagnetic layers of the calorimeter, the weights for these layers are fixed to those found from the electron optimization.[36]

To make the weights independent of the distribution of particle energies within a jet, the sampling weights were chosen by optimizing the weights over a wide range of incident particle energies. This procedure is based upon an assumption that the re-

sponse of the detector has a linear dependence upon the energy of incident hadrons. In other words, that the sampling weights β_i and the scale factor α can be expressed as energy-independent constants. Consequently, any energy dependence of the weights has to be ignored when jet response is derived from the response to individual hadrons.

Finally, hadronic response was optimized over two beam positions in the calorimeter, using the same procedures as in electron optimization.[36] However, although the electromagnetic weights were optimized over the entire range of the data in the CC, namely at η=0.05, η=0.45, and η=1.05, the hadronic weights were only optimized at η=0.05 and η=0.45 (because hadrons are not fully contained in the CC at η=1.05).

5.3 Characterizing Results of Weight Optimizations

In order to investigate the effects of the constraints on optimization discussed in Section 5.2, the data will be optimized in several ways, beginning with an unrestricted optimization, and then applying the restrictions in sequence. These results will be compared to a control set, which relies on reconstruction of energy using a set of default weights, and thereby used to judge the improvement, if any, produced by the optimization.

5.3.1 The Default Sampling Weights

The default (starting) sampling weights for this analysis (corresponding to β_i in Eq. 5.9, with $\delta = 0$) consist of the optimized electron weights for the electromagnetic sections (layers 1-4),[36] and dE/dx weights for the hadronic layers (layers 5-8). In the following analysis, the original optimized electromagnetic weights (and scale factor α) have all been renormalized so that the weight for the third electromagnetic layer (EM3) is 0.75, or $\beta_i(3) = 0.75$, in order to maintain the previous relative electromagnetic layer weights. The overall scale factor will not vary throughout all the analysis, and is fixed so that α = 0.00394 (which is, again, consistent with previous optimization of electron data). Unless otherwise specified, results of all optimizations will be compared with those obtained using this default set of weights. The default weights are shown in Table 5.1.

Table 5.1 Default sampling weights, with α = 0.00394 and δ = 0

Calorimeter Layer	Sampling Weights
EM1	0.981±0.006
EM2	0.639±0.005
EM3	0.750
EM4	0.734±0.003
FH1	1.354±0.04
FH2	1.293±0.04
FH3	1.295±0.05
CH	6.135±0.18

In order to simplify comparisons between the default weights and any optimized weights, the optimized sampling weights will be presented as factors that are to multiply default set. To prevent confusion, such factors will be listed as *sampling factors*. Consequently, all the sampling factors for the default weights equal unity.

5.3.2 Characteristics of the Response of the Calorimeter to Single Hadrons

The two important characteristics of the response of a calorimeter are the linearity and the resolution. The resolution is found from a fit of Eq. 5.12 to the reconstructed data as a function of energy.

$$\left(\frac{\sigma(E)}{\mu(E)}\right)^2 = C^2 + \frac{S^2}{E} + \frac{N^2}{E^2} \tag{5.12}$$

Here E are the nominal energies of the beam settings (found from PWC momentum measurement, and renormalized as discussed in Sec. 4.4), and $\sigma(E)$ and $\mu(E)$ are obtained from Gaussian fits (see Eq. 4.3) to distributions of the reconstructed energies at the various settings (as shown in Fig. 4.5). Figure 5.1 shows a plot of the fractional resolution for the default weights (see Table 5.1) at η=0.45. In the fit, the noise term N is fixed to the standard deviation of the appropriate inspill-pedestal distribution. The

parameters of the fit are given in the figure.

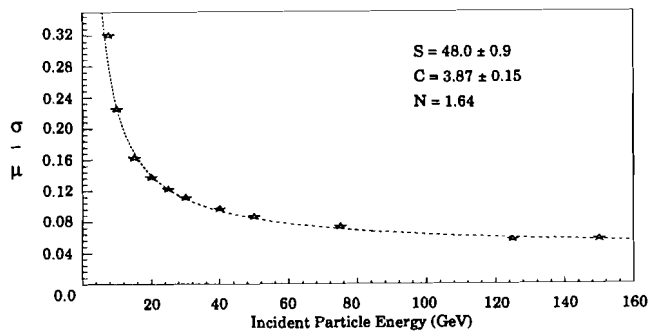

Figure 5.1 Fractional resolution obtained when using default weights at η=0.45

Linearity of response of the calorimeter to single particles is an important characteristic of the detector because it also affects jet resolution. (Linearity refers to the degree to which the reconstructed energy is linearly related to the incident energy.) A plot of the detector response to hadrons at η=0.45, using the default sampling weights is shown in Fig. 5.2(a), along with a linear fit through the data. The residuals, or the fractional differences between the data and the results of the fit, are shown in Fig. 5.2(b), along with the parameters obtained from the fit to a straight line.

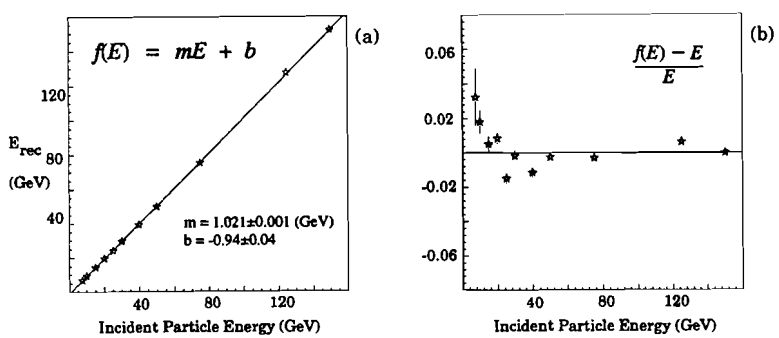

Figure 5.2 Reconstructed energies obtained using default weights at η=0.45

From the statistical errors given in Fig. 5.2(b), it is clear that the fit to a straight line is poor, and that there is a sizeable intercept. At this point, it is important to stress the fact that such a linear fit is of little use when optimizing jet resolution, since individual particle energies within a jet cannot be corrected through such a fit (because the individual energies cannot be unfolded from the total jet energy). Nonlinearities of the detector can be characterized, however, by the fractional difference between the reconstructed and incident energy, as shown in Fig. 5.3. The dashed curve corresponds to the previous linear fit to the data.

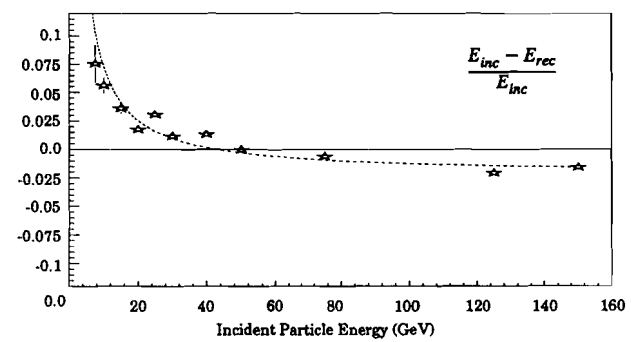

Figure 5.3 Fractional difference between incident and reconstructed energy using default weights at η=0.45

For a detector with a truly linear response, the data points would all be consistent with zero (within statistical uncertainty). Clearly, this is not the case for the default response, especially at the lower energies. It is important to note that the response to electrons in DØ is essentially linear,[36] so that the plot of the fractional differences in the response to hadrons provides almost a direct measure of the difference in the relative electron/hadron response of DØ calorimeters. Thus, Fig. 5.3 shows that, for energies > 50 GeV, the relative electron/hadron response is greater than unity. Remember that the relative electron/hadron response is not the same as e/h (see Sec. 2.1.2).

5.4 Optimizing Single-Hadron Response While Applying Restrictions Aimed at Improving Jet Resolution

In this section, we will investigate the detector resolution and linearity for single hadrons under different restrictions on the optimizations of the sampling weights γ_i. We will consider energy and position-dependent weights, allowing the weights to vary for the electromagnetic layers as well as for the hadronic layers. Then, we will restrict ourselves to energy-independent weights. After that, data from the two η positions in the detector will be optimized simultaneously to find a single set of position-independent weights. Finally, the weights for the electromagnetic layers will be fixed to those considered best for electrons (the default), to obtain a set of weights that is optimized simultaneously for electrons and hadrons. In this manner we hope to learn which restrictions produce the greatest degradation in resolution and linearity for hadrons, as well as deduce whether the final optimized weights (applying all restrictions) are likely to produce better jet-energy resolution.

The optimized sampling weights can be divided into sets that correspond to different restrictions in the optimization of hadronic response. These sets are defined in Table 5.2. For this study we use only the data corresponding to the high-energy beam configuration at ϕ = 3.16 DØ units (see Sec. 4.4), thus optimizing over an energy range of 7.5-150 GeV. Also, the optimization for Sets 1 and 2 were performed over each energy individually, resulting in a different set of weights for each energy, while the other sets were optimized for all energies simultaneously, as shown in the table. The entire data sample for this optimization consists of the two high-energy sets described in Sec. 4.4, one set taken at η=0.05, and one at η=0.45.

The results from the various optimizations will be presented solely for gauging the effect of the various restrictions on single-hadron response. Because, for application in DØ, all restrictions must be imposed upon any final set of weights, only the results of the optimization using Set 6 will be compared to the default set to decide which of the sampling factors would be best for the DØ detector. However, in Chapter 6 we will be investigating ways to reduce the impact any of the restrictions through alternate implementations, so it is useful to study the relative magnitudes of the effects that the different contstraints have on the energy resolution of individual hadrons.

Table 5.2 Definitions of sets of hadronic weights

Set	η Value	EM Weights	Energy Points
1	0.05	allowed to vary	individual
2	0.45	allowed to vary	individual
3	0.05	allowed to vary	simultaneous
4	0.45	allowed to vary	simultaneous
5	0.05,0.45	allowed to vary	simultaneous
6	0.05,0.45	fix at default	simultaneous

5.4.1 Results of Hadronic Optimizations

The sampling factors found for Sets 1 and 2 for each available energy are presented in Tables 5.3 and 5.4, respectively. As stated earlier, correlations between layers make any uncertainties cited on purely the sampling factors difficult to interpret. Therefore, no uncertainties are given. Instead, the resolution of the reconstructed energies will be used to provide an indication of the quality of the results.

Table 5.3 Sampling Factors for Set 1

Energy (GeV)	EM1	EM2	EM3	EM4	FH1	FH2	FH3	CH
7.5	1.98	1.55	1.03	1.28	0.98	0.73	0.66	0.51
10.0	1.81	1.58	1.12	1.19	0.93	0.93	0.80	0.63
15.0	1.68	1.34	0.89	1.24	0.94	0.88	0.95	0.78
20.0	1.97	1.28	0.94	1.20	0.96	0.92	0.91	0.87
25.0	2.30	1.34	0.94	1.21	0.96	0.95	0.98	0.88
30.0	2.18	1.29	0.95	1.19	0.95	0.95	1.02	0.87
40.0	1.91	1.79	0.88	1.22	0.95	0.94	0.96	0.95
50.0	2.98	1.30	0.87	1.17	0.94	0.95	1.02	0.90
75.0	2.58	1.39	0.87	1.15	0.96	0.91	1.02	0.95
100.0	2.16	1.80	0.86	1.15	0.94	0.93	1.04	0.92
150.0	2.41	2.21	0.75	1.13	0.92	0.93	1.00	0.91

Table 5.4 Sampling Factors for Set 2

Energy (GeV)	EM1	EM2	EM3	EM4	FH1	FH2	FH3	CH
7.5	1.20	0.96	0.98	1.45	0.85	0.70	0.72	0.22
10.0	2.01	0.58	1.07	1.23	0.97	0.89	0.85	0.74
15.0	1.89	1.03	0.94	1.27	0.95	0.94	0.91	0.85
20.0	2.24	1.07	0.93	1.21	0.94	0.93	0.96	0.85
25.0	1.99	1.28	0.99	1.18	0.97	0.93	0.98	0.88
30.0	1.72	1.55	0.97	1.17	0.96	0.90	1.00	0.87
40.0	1.94	1.43	0.98	1.17	0.94	0.92	1.02	0.93
50.0	2.19	1.34	0.94	1.18	0.94	0.95	1.01	0.90
75.0	2.23	1.31	0.94	1.16	0.93	0.94	1.04	0.93
125.0	2.97	1.47	0.98	1.11	0.93	0.94	1.02	0.94
150.0	2.77	1.00	0.93	1.12	0.93	0.95	1.02	0.92

These tables show that the weights vary somewhat with energy, but do not display any clear trend. Also, due to correlations between layers, the significance of the observed variations is quite uncertain.

Table 5.5 gives the sampling factors for the other optimizations. The weights are consistent overall, except for the EM weights for Set 6, which, of course, are fixed to the default values. The hadronic weights are virtually the same for all optimizations.

Table 5.5 Sampling Factors for Sets 3, 4, 5, and 6

Set	EM1	EM2	EM3	EM4	FH1	FH2	FH3	CH
3	2.24	1.63	0.87	1.16	0.94	0.93	1.00	0.90
4	2.11	1.13	0.96	1.15	0.94	0.93	1.01	0.91
5	2.16	1.34	0.92	1.15	0.94	0.94	1.01	0.91
6	1.00	1.00	1.00	1.00	0.98	0.94	1.01	0.91

Tables 5.6 and 5.7 provide the parameters characterizing the optimizations for the data sets at η=0.05 and η=0.45, respectively. Although the character of the results for Sets 1 through 5 are not grossly different, Sets 1 and 2, which allow an energy dependence, provide the best results overall. The results using Set 6 show a larger degradation in resolution and linearity than the other sets, indicating that restricting the EM

weights to those that are best for electrons has the biggest detrimental effect on the hadron response.

Table 5.6 Parameters from optimizations at η=0.05

	Fits to $\sigma(E)/E$		Fits to straight line	
Set	S (%)	C (%)	Slope	Intercept (GeV)
Default	51.1±1.0	3.56±0.21	1.022±0.001	-0.84±0.04
1	39.8±0.9	2.84±0.17	1.004±0.001	-0.51±0.03
3	42.7±0.9	2.45±0.21	0.999±0.001	-0.41±0.03
5	43.8±0.9	2.31±0.21	1.000±0.001	-0.49±0.03
6	47.2±0.9	3.30±0.20	0.995±0.001	-0.75±0.03

Table 5.7 Parameters from optimizations at η=0.45

	Fits to $\sigma(E)/E$		Fits to straight line	
Set	S (%)	C (%)	Slope	Intercept (GeV)
Default	48.0±0.9	3.87±0.16	1.021±0.001	-0.94±0.04
2	39.1±0.8	2.57±0.15	1.000±0.001	-0.21±0.03
4	40.2±0.8	2.38±0.17	1.001±0.001	-0.34±0.03
5	41.2±0.8	2.22±0.18	1.000±0.001	-0.30±0.03
6	45.9±0.9	3.51±0.16	0.994±0.001	-0.81±0.04

Fig. 5.4 shows the fits to the fractional resolutions for the various optimizations. These fits were used to extract the values of C and S presented in Tables 5.6 and 5.7. The plots confirm that the best resolution is obtained using energy-dependent weights, and that restrictions worsen the resolution. However, the energy-independent weights (Sets 3 and 4), and the energy-independent and position-independent weights (Set 5) produce only slightly worse resolution at lower energies, and equivalent resolution at higher energies, indicating that requiring the weights to be independent of energy and position does not have a great effect on the resolution.

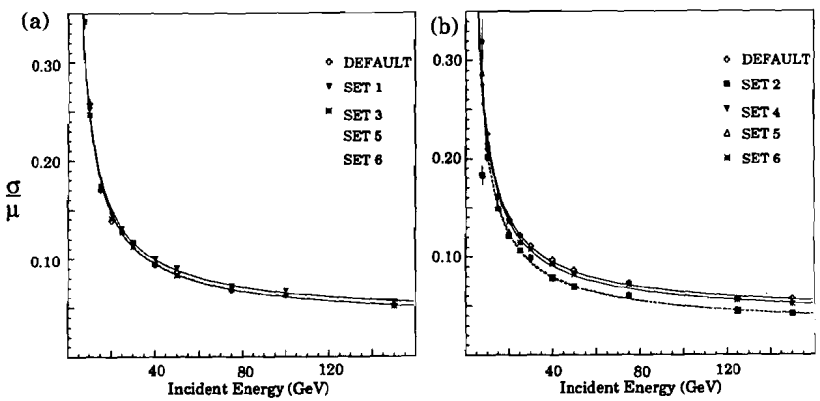

Figure 5.4 Fractional resolutions for hadrons at (a) η=0.05, and (b) η=0.45

Figure 5.5 gives the fractional differences in the energies (between reconstructed and incident) for η=0.05 and η=0.45, for the various optimizations. As can be seen, the default set of weights produce reconstructed energies that are, on average, symmetric around zero for the range of incident energies. However, optimized results appear to provide less absolute spread over the entire range of energies. It is important to recognize that the fractional differences for all sets other than Set 6 (and the Default) could be renormalized (with an overall scale factor) so that they would be symmetric about the zero. Since the purpose of these optimizations is just to show the effect of the various restrictions, we will not perform such a renormalization. It should be pointed out that the factors for Set 6 are constrained by the requirement of best electron resolution, and cannot be rescaled.

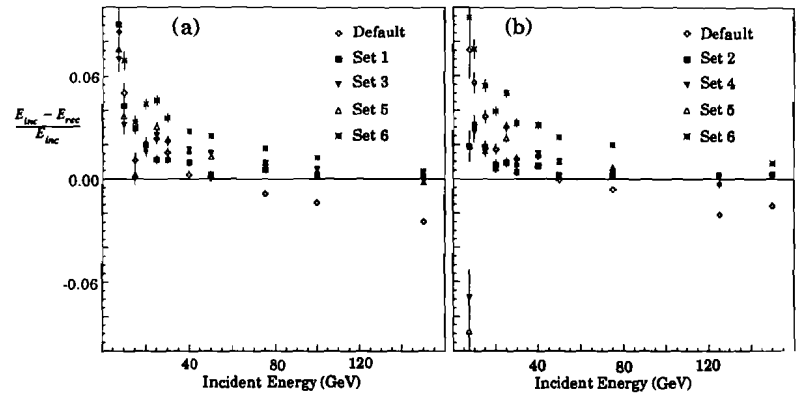

Figure 5.5 Deviation plots for (a) η=0.05, and (b) η=0.45

From these results, we conclude that optimization improves the single-hadron energy resolution. However, it is also clear that the successively imposed restrictions tend to worsen the resolution relative to that obtained using the unrestricted optimization. All of the sets of sampling factors do indeed produce resolutions somewhat better than that found for the Default Set (including Set 6). However, because the Default Set provides reconstructed energies that are more evenly distributed around the incident energies than Set 6 does, it is not clear which one would best optimize jet energy resolution.

5.4.2 Varying only Relative Scales on the Default Set ("Shifted Set")

Hadronic resolution can also be improved by simply changing the relative scales used for the hadronic and electromagnetic sections. That is, the reconstructed energy can be described by:

$$E^k = \alpha E^k_{em} + \alpha' E^k_{had} \tag{5.13}$$

where E^k is the reconstructed energy for event k; α is the scale factor appropriate for electromagnetic layers; E^k_{em} is the sum over layers 1-4 in Eq. 5.1; and E^k_{had} is the sum

over layers 5-8 in Eq. 5.1, using the Default Set of sampling weights; and α' is the scale for the hadronic layers, nominally equal to α. It is interesting to see how a change in the relative value of α and α' affects the response of the detector to single hadrons.

Table 5.8 Results from varying only the relative hadronic scale, α'

		Fits to σ(E)/E		Fits to straight line	
Weights	η	S (%)	C (%)	Slope	Intercept (GeV)
Default	0.05	51.1±1.0	3.56±0.21	1.022±0.001	-0.84±0.04
Set 6	0.05	47.2±0.9	3.30±0.20	0.995±0.001	-0.75±0.03
Default (shifted)	0.05	47.2±0.9	3.33±0.20	0.996±0.001	-0.75±0.03
Default	0.45	48.0±0.9	3.87±0.16	1.021±0.001	-0.94±0.04
Set 6	0.45	45.9±0.9	3.51±0.16	0.994±0.001	-0.81±0.04
Default (shifted)	0.45	46.3±0.9	4.13±0.16	1.020±0.001	-0.83±0.04

Table 5.8 compares the results for the Default Set and the fully optimized weights of Set 6 (both also given in Tables 5.6 and 5.7) with the results when α' is shifted from 1.000 to 0.965, an amount chosen arbitrarily to produce results close to the optimized set. We refer to the shift in the Default Set as the Shifted Set of sampling factors. As can be seen, within errors, the results using optimized and shifted weights are essentially identical.

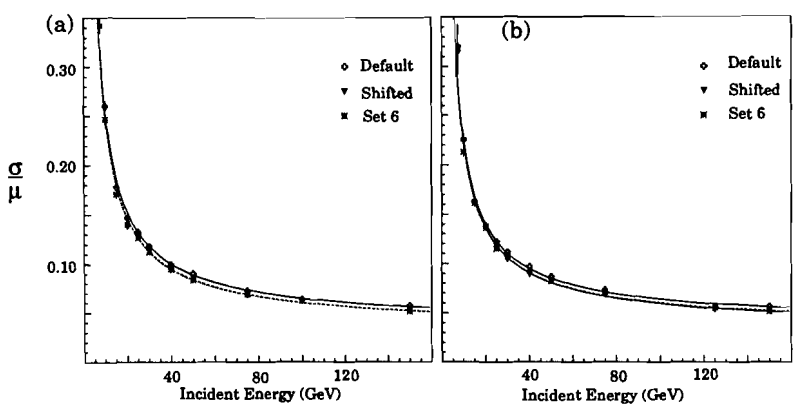

Figure 5.6 Resolution plots for (a) η=0.05, and (b) η=0.45

Figure 5.6 displays the energy resolution of the detector for our three cases, and Fig. 5.7 shows the plot of the fractional differences in energy. Again, the results for a shift in α' to 0.965 are essentially identical to those already found for Set 6. The response using the Shifted Set is virtually identical to that for Set 6, and significantly different from that using the Default Set.

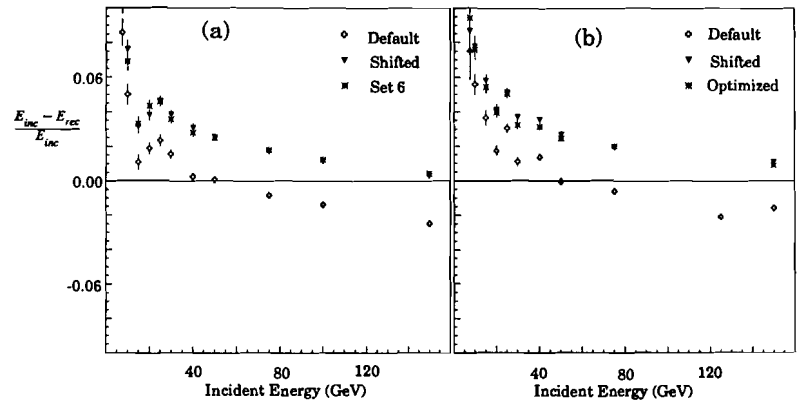

Figure 5.7 Fractional energy deviations for (a) η=0.05, and (b) η=0.45

The results of this section suggest that the small improvement in resolution and linearity gained through optimization of layer weights can also be achieved by simply changing the relative scale between the electromagnetic and hadronic modules. Such a simplification of the optimization procedure is reasonable because differences in the relative responses between different portions of the calorimeter can have a negative impact on resolution. Thus, reducing these differences, as is done by changing the relative scale here, can improve the resolution. Since the optimization routine is designed to improve the resolution, the primary impact of the restricted optimization may well have arisen out of such a variation between the electromagnetic and the hadronic scales. The results of this section seem to have verified that this is the case.

5.4.3 Quality of the Response of the Calorimeter to Hadrons

As we have discussed before, the goal of any optimization of the response of a calorimeter to single hadrons is to improve the measurement of jet energy. However, without a detailed knowledge of the structure of jets, and without the means to implement any such knowledge in the optimization, it is, of course, difficult to determine which weights produce the best jet resolution. We have therefore examined the response to single hadrons in order to estimate the features of the calorimeter response that are likely to have the greatest impact on jet energy resolution.

Three characteristics of energy deposition for single hadrons that come to mind involve the resolution, linearity with energy, and the relative electron/hadron response. Improving resolution is desirable because it leads to more precise measurement of energies of single particles, and thereby, hopefully, to a more precise measurement of the energy of a jet. Also, increasing linearity of response to incident-particle energy is important for minimizing variations in the reconstructed energy of a jet that may depend upon the energies of its individual particles. Finally, it is important to ensure that the mean response of the detector is the same for electromagnetically and hadronically interacting particles, since differences in response to different types of particles can lead to large *a priori* variations in the energies of reconstructed jets.

From previous arguments,[13] it appears that the relative electron/hadron response has the greatest impact upon jet resolution (see Sec. 2.1.3). Since jets of a given energy can exhibit wide fluctuations in the types of their constituents, there is no simple way to correct for effects of a large electron/hadron response. Thus, the principle requirement for improving jet resolution through a variation in the response to single hadrons is making the average hadron response as close to electron response as possible. The issue of linearity is also very important, but since the energy of jets is the sum of the energies of individual particles, corrections can be based upon overall jet energy. Therefore, after settling the electron/hadron issue, linearity can also be improved.

Finally, while it is useful to have good single-particle resolution, the degradation of jet resolution due to variations in the response to different jet constituents at a given jet energy is far more important. Thus, improving single-hadron resolution of calorimeters

is not a primary concern in collider environments. It should be recognized that the overall optimization procedures discussed in this chapter tend to equalize the response of the hadronic layers and of the electromagnetic layers (thus improving resolution). Because the DØ calorimeter is not completely compensating (that is, $e/h \approx 1.05$ and not 1.00), the optimization therefore decreases the reconstructed energies, which has the unfortunate effect of worsening the linearity, while improving resolution.

Since the Default Set of weights produces a hadron response that is, on average, more symmetric relative to the electron response (which, as stated before, is essentially linear with incident hadron energy), the default weights would seem to be better suited for use in improving jet resolution. (Although the optimized weights improve both the resolution and the linearity of response for hadrons, these improvements have less impact on the jet resolution.) Thus, based upon the results of this chapter, the DØ experiment decided to use the default weights for reconstructing jet energies.

It is clear that the methods for determining the appropriate restrictions upon the optimized weights, as well as the rationale for deciding which weights are best, are only qualitative. As we have emphasized, a detailed knowledge of jet structure is needed to determine quantitatively which weights are best for jet resolution. In the following chapter, we introduce a method for simulating jets using a Monte Carlo program for jet fragmentation, which, when coupled with data from the test beam, can provide a more rigorous procedure for maximizing jet energy resolution.

Chapter 6.

Optimizing Jet Energy Resolution with Jets Simulated from Test-Beam Data

As we discussed in Chapter 5, restrictions introduced in the optimization of the energy response of the DØ calorimeter to hadrons worsen hadron energy resolution by a total of about 6% for the sampling term S over that found using an unrestricted optimization (see Tables 5.6 and 5.7). The worst degradation occurs when the weights for the electromagnetic layers are fixed to values that provide the best resolution for single electrons. Another restriction that produces a clear loss in resolution is when the weights are required to be independent of the energy of the incident particle. These restrictions can produce similar or perhaps even more detrimental effects on jet resolution. Finally, the qualitative determination that the Default Set of weights would be best for jet resolution leads to a loss in single hadron resolution of about 9-11% in the sampling term S. However, without a detailed knowledge of the composition of jets, it is hard to predict the impact of such constraints. Unfortunately, jets of precise energy cannot be produced in test beams, and consequently cannot be studied in a calorimeter.

However, production of jets can be modeled using Monte Carlo generation based on

QCD theory. The individual hadronic fragments of such jets can be taken from a library of data obtained in the test beam, summed to form a jet, and then propagated through the detector to simulate the response of the DØ calorimeter to jets. In this chapter, we use such simulations to study the effects that the restrictions placed on single-hadron optimization produce on jet resolution. In particular, we study the effects on jet response using the default weights from Chapter 5, and investigate possible alternate schemes for improving jet resolution.

6.1 Generating Test Beam Jets

The Particle Library, based on data from the test beam, was formed to provide the individual particles needed for generating jets. The Particle Library, which is described in greater detail in Appendix B, contains both electron and hadron data over the full range of energies studied at the test beam, but only at the position corresponding to η=0.05 and ϕ=3.16 (3.10 radians) in the DØ calorimeter. Extrapolations, also described in Appendix B, are performed to shift the scales and locations of particles to the appropriate energies and positions of specified jet constituents. These particles are then superimposed to form complete jet events which mimic DØ events on a cell-by-cell level.

To specify the structure of the jets to be built by the Particle Library, partons were generated at minimum transverse energies of 20, 30, 40, 50, 63, 80, 100, 120, 150, 175, and 200 GeV, using the Isajet program.[40] After fragmentation and radiation, the jet with the highest p_T from the collision was selected and stored in a file specifying the energy, type, and the η and ϕ for each constituent. For each specified minimum energy, this process produced a group of jets distributed around the minimum energy. The specified set of minimum energies had been selected so that, taken all together, the Isajet events had a broad range of energies with essentially uniform distribution between about 15 and 225 GeV. We will refer to these seed events as "Isajet events", to distinguish them from the test-beam jet events ("TB jets"), which are constructed using the Isajet events.

For each Isajet event, the Particle Library was used create TB jets that are similar to jets seen in the DØ detector. Because the library is limited to particles at η=0.05,

only central jets could be simulated accurately (see Appendix B for a discussion of the differences between the assembled jets and DØ jets). For each specified Isajet event, 200 TB jets were constructed from data randomly selected from the Particle Library (see Appendix B).

6.2 Parameters of Jet Response

Because a non-linearity in the energy response of calorimeters to jets can, in principle, be easily corrected, we will concentrate on issues relevant to the resolution of the DØ calorimeters in optimizing TB jets. The jet resolution was fitted to the same generic equation that was used for parametrizing the energy resolution of single particles (see Eq. 5.12). However, because the noise term in the jet cannot be simply the sum over the noise of individual hadrons, the N parameter must be handled differently for TB jets.

For the resolution of hadrons in single-particle test beam data, the term N in Eq. 5.12 was equated to the expected standard deviation of an appropriate pedestal distribution, and thereby the number of degrees of freedom in the fit was reduced. When the contributions from individual particles are added together to form TB jets, the magnitude of the noise in a typical TB jet will usually be far greater than for a single particle, and will increase with the multiplicity of the jet. Since the multiplicity of a jet also depends upon jet energy, the noise in TB jets will have a dependence upon incident jet energy. This is an artificial feature of building jets from individual particles, and does not reflect the true noise of the calorimeter.

Noise in TB jets was estimated by merging data for inspill pedestal events on a cell-by-cell basis, using the same correction algorithms that were applied to the cells occupied by the particles in a TB jet, using the following procedure. First, an inspill-pedestal library was created in parallel with the Particle Library: this contained inspill pedestal events from the test beam. For each initial Isajet event that had been used to create TB jets, we then created a jet-pedestal event by adding events from the pedestal library for all individual particles in the Isajet event. Essentially, a TB jet was built, but with cells containing only pedestal signals, rather than ionization energy. This procedure overestimates the noise seen in a DØ jet-pedestal event by an amount equivalent to that over-

estimated by a TB jet relative to a real (DØ) jet, providing a dependence of the standard deviation of a jet-pedestal event on incident jet energy. The mean value of the jet-pedestal events is, of course, still zero. A plot of the N parameter (i.e., the average width of the jet-pedestals) vs. incident jet energy, in 5 GeV intervals, is shown in Fig. 6.1. A fit to the energy dependence is also shown in the figure, and is given by:

$$N(E) = P_1 + P_2 \ln(E) \tag{6.1}$$

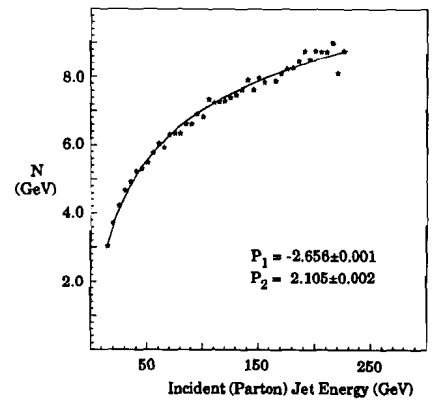

Figure 6.1 Standard deviation of "artificial" inspill pedestals (jet-pedestal events) as a function of incident jet energy

Due to the way the data in the Particle Library are scaled for low incident energies (see Appendix B), the noise for a single particle (≈1.9 GeV) does not have to correspond exactly to the noise at smallest jet energy in Fig. 6.1. Also, the same scaling techniques cause the above fit to become non-physical at energies less than about 10 GeV (for example, N(5 GeV) ≈ 0). Since the particle library is only used down to 15 GeV, this will not present a problem.

Using Eq. 6.1 in Eq. 5.12, we obtain a modified form that we can use to extract the

other parameters of the fractional resolution:

$$\left(\frac{\sigma(E)}{\mu(E)}\right)^2 = C^2 + \frac{S^2}{E} + \frac{\left[P_1 + P_2 \ln(E)\right]^2}{E^2} \tag{6.2}$$

The analysis in Chapter 5 indicated that the default weights (given in Table 5.1) should be used for building jets. Here we will examine the jet properties found using these weights. Figure 6.2(a) gives a plot of the reconstructed jet energy vs. the incident jet energy, including a linear fit through the data, and the parameters for the fit (the statistical errors on these are very small). In Fig. 6.2(b) we show the result of the linear fit compared to the fractional energy difference.

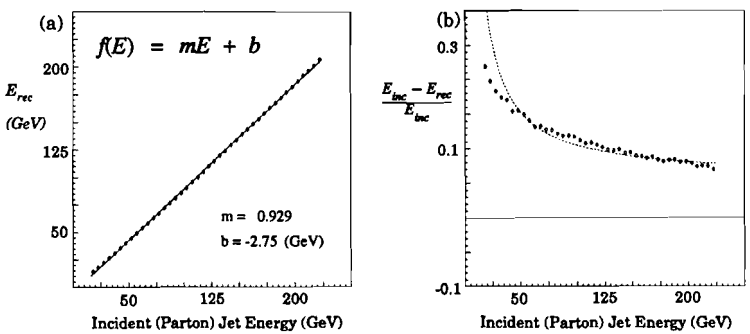

Figure 6.2 Reconstructed energies obtained using default weights at η=0.45

As seen in Fig. 6.2, the response of the calorimeter to energy is not completely linear, and has both a large offset and a slope that differs significantly from 1.0. In order to correct for these effects, a simple second-order polynomial can be fitted to the response, and the reconstructed energy can be corrected using the resulting function. In this chapter we correct all energies in this manner. The corrected energy for the default weights, in terms of the plot of fractional energy differences, is given in Fig. 6.3(a), and the relative resolution is shown in Fig. 6.3(b).

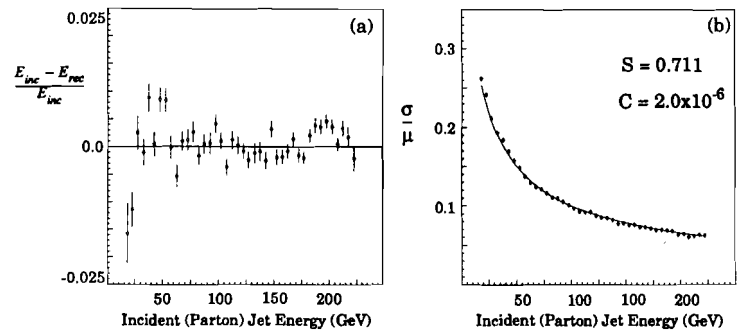

Figure 6.3 (a) Relative differences and (b) relative resolution for corrected reconstructed jet energies

The fit that corresponds to the corrected data in Fig. 6.3 is:

$$E_{rec}^{corr} = P_1 + P_2 E_{rec} + P_3 E_{rec}^2 \tag{6.3}$$

with P_1 = 2.42 GeV, P_2 = 1.13, and P_3 = -3x10^{-4} GeV^{-1}, and where E_{rec} is the uncorrected reconstructed energy shown in Fig 6.2.

Figure 6.3 shows that the data at the lower end of the energy range have more scatter than at the central region. This is due to the fact that the simulation of DØ jets becomes less accurate at the lowest energies. This breakdown of the simulation is mainly due to the scaling of the lowest energy particles, and an arbitrary cutoff of low-energy jet constituents used when building the TB jets (see Appendix B).

The Isajet jets in this analysis were required to be in the central region of the calorimeter at the Isajet generation stage. However, due to the way the particle library produces the coordinates of TB jets by shifting the particles at η=0.05 to the appropriate coordinates, TB jets will not vary in structure, regardless of pseudo-rapidity of the Isajet jet.

6.3 Optimization of Jet Resolution

All results in the following optimizations will again be presented in terms of sampling factors, relative to the default weights, as was done in Chapter 5. (The default weights correspond to dE/dx weights for the hadronic layers, and EM-layer weights chosen to optimize the response to electrons, and were given in Table 5.1).

Five different optimization schemes (OS) were implemented to try to improve the energy resolution of TB jets. OS-1 simply varies the relative scales between the EM and hadronic layers, and otherwise uses the default weights. OS-2 allows all weights to vary, and provides a single constant offset δ for the simultaneous optimization of all jet energies. OS-3 admits weights that depend on the reconstructed jet energy, and OS-4 allows weights that depend on the fraction of total reconstructed jet energy deposited in the electromagnetic layers (EM fraction). Finally, OS-5 implements a sequential optimization of energy-dependent and EM fraction-dependent variations. A summary of the various optimization schems is included in Table 6.1, and the details of the separate optimizations are given below.

Table 6.1 Summary of optimization schemes (OS)

OS	Parameters allowed to vary	# parameters	constant offset δ
1	scale factors describing relative contributions of EM and hadronic sections	2	set to zero
2	energy-independent weights describing the relative contributions of all layers	8	varies
3	parameters describing the energy-dependence of 8 layer weights	16	set to zero
4	parameters describing the EM fraction-dependence of 8 layers weights and a constant offset δ	18	varies
5	parameters describing the EM fraction-dependence and energy-dependence of 8 layer weights and a constant offset δ	8	varies for EM dependence set to zero for energy-dependence

6.3.1 Optimization of Relative Electromagnetic and Hadronic Scales (Scheme OS-1)

Just as in the case of single hadrons, the relative scales of the signals from the electromagnetic and hadronic sections were varied, keeping the default weights for the individual layers in the two sections. The reconstructed jet energy (E^k_{rec}) is found from:

$$E^k_{rec} = \alpha_{em} E^k_{em} + \alpha_{had} E^k_{had} \tag{6.4}$$

where E^k_{rec} is the reconstructed energy for TB jet event k, E^k_{em} and E^k_{had} are the sums of the energies found in the electromagnetic and hadronic layers, respectively (calculated using the default weights), and α_{em} and α_{had} are parameters that are varied using our standard optimization routine for all TB jet events (all energies). The resultant values of α_{em} and α_{had} are given in Table 6.2. Uncertainties on these values are not included: since the scales are found through the optimization procedure used to find sampling weights, the uncertainties are of little use in evaluating the results, due to the correlations between them.

Table 6.2 Optimized relative scales (OS-1)

α_{em}	1.25
α_{had}	0.98

6.3.2 Full Optimization Without Energy Dependence (Scheme OS-2)

The TB jet resolution was optimized simultaneously over the full range of energies, resulting in the set of 8 sampling factors and the constant offset δ (see Eq. 5.9), given in Table 6.3. This scheme assumes that the weights are independent of jet energy.

Table 6.3 Fully optimized, energy-independent sampling factors (OS-2)

Calorimeter Layer	Sampling Factors
EM1	2.443
EM2	1.163
EM3	0.856
EM4	1.335
FH1	1.006
FH2	0.895
FH3	0.839
CH	0.758
δ (GeV)	3.325

6.3.3 Sampling Factors as a Function of Reconstructed Jet Energy (Scheme OS-3)

The energy-dependent weights were found as follows:

1. The default reconstructed energy (E_{def}) was calculated using the default weights in Eq. 5.9.
2. The events were divided into 5 GeV bands of E_{def}.
3. A set of sampling factors were obtained for each band E_{def}.
4. The samling factors were fitted to a linear function of E_{def}.

A constant offset δ is not allowed in this optimization, since such an offset is not suitable optimizations over small energy ranges. The calculated sampling weights, along with the linear fits to E_{def}, are shown as a function of reconstructed energy in Fig. 6.4. All eight fits are superposed in Fig. 6.4(i) to demonstrate the correlations between the weights as a function of energy, along with a line at unity. The parameters for these functions, along with the statistical uncertainties on them, are given in Table 6.4.

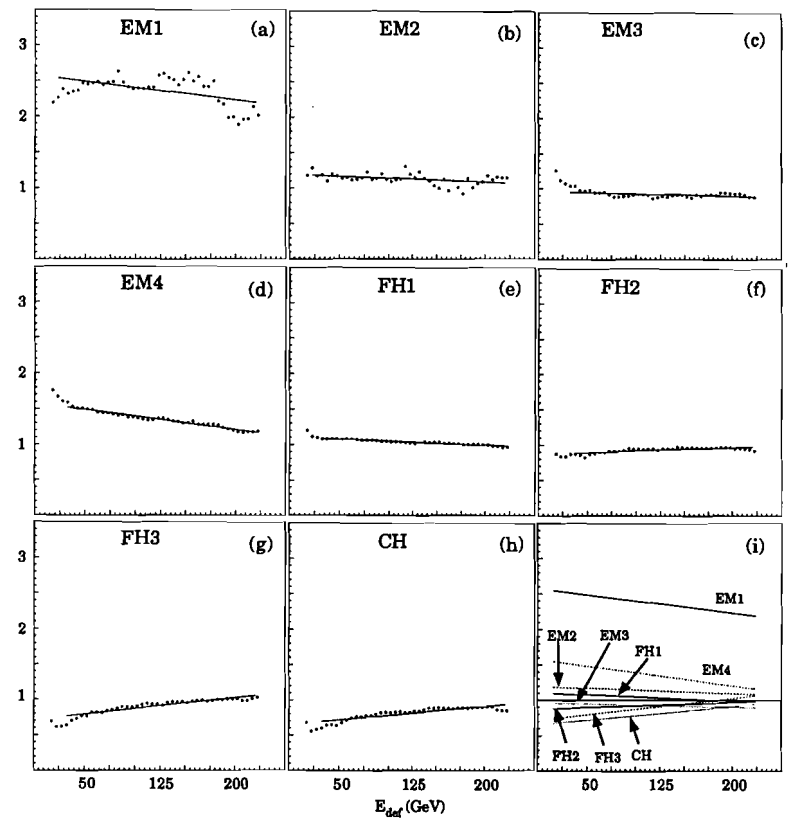

Figure 6.4 Sampling factors as a function of reconstructed energy (OS-3). The fits are to linear functions of the form $P_1 + P_2 E_{def}$ (see Table 6.4).

As can be seen in Fig. 6.4, the sampling factors at the extreme ranges of the energy scales do not seem to follow the trend observed in the center regions. By changing the ranges for the fits, we have determined that restricting the fits to the trend established by the central energy regions results in the best overall resolutions. The functions in the figures are plotted only over the energy ranges used in the fits.

It can also be seen from Fig. 6.4 that some of the sampling factors do not seem to depend linearly on energy. We have tried to fit the sampling factors with a more complex energy dependence, but found that using a linear fit provides similar overall resolution, and produces a more linear energy response. We have consequently chosen the simplest parameterization for this study.

Table 6.4 Parameters describing energy-dependence of sampling factors (OS-3)

	P_1	P_2 ($\times 10^{-3}$) (GeV^{-1})
EM1	2.571±0.003	-1.69±0.02
EM2	1.195±0.003	-0.51±0.02
EM3	0.963±0.004	-0.33±0.03
EM4	1.579±0.004	-1.88±0.03
FH1	1.104±0.004	-0.56±0.03
FH2	0.870±0.004	0.49±0.03
FH3	0.714±0.004	1.56±0.03
CH	0.652±0.004	1.28±0.03

It is interesting that all weights appear to approach unity at highest energies, as shown in Fig. 6.4(i). This would suggest that these weights should provide the greatest improvement in reconstructed energy resolution at lowest energies.

6.3.4 Sampling Factors that Depend on Jet EM Fraction (OS-4)

The weights that depend on EM fraction were found as follows. Starting out with the default E_{def} values, as discussed in Section 6.3.3, we defined F_{EM} as the fraction of the energy in a TB jet that reconstructed in the EM section. The F_{EM} values for all events were divided in bands of 0.04 width, to obtain a set of sampling factors (and a constant offset δ) for all events (independent of energy) within each band of EM fraction. These factors were then fitted as a function of F_{EM}.

The sampling factors as a function of EM fraction in a TB jet are shown in Fig. 6.5, along with the linear functions used in the fit. The parameters for these functions, along with their statistical errors, are given in Table 6.5.

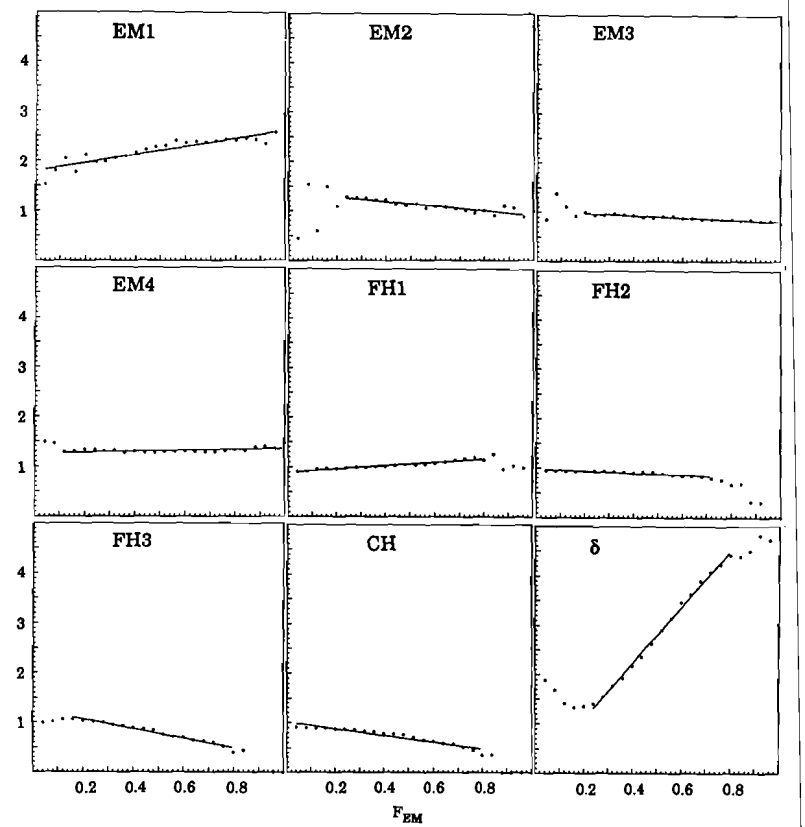

Figure 6.5 Sampling factors as a function of the fraction of the reconstructed energy in a TB jet that is deposited in the EM section. The fits are to linear functions of the form $P_1 + P_2 F_{EM}$ (see Table 6.5)

As seen in Fig. 6.5, the sampling factors for $F_{EM} \leq 0.2$ and $F_{EM} \geq 0.8$, (especially for δ) show marked deviations from the trend established in the rest of the range. This is caused primarily by the characteristic patterns of energy deposition for jets in these regions. For example, a jet with more than 90% of its energy in the electromagnetic section, will have little energy in CH that could be used to sharpen the CH sampling factor.

Also, it should be recognized that jets usually deposit ≈ 0.5 of their energy in the EM section, so the low incidence of jets with > 0.9 of the total energy in either section makes the optimizations in these regions tend to be limited by statistics (the statistical uncertainties on these points are connected to the correlations between weights, so these uncertainties are not shown in the plots).

Table 6.5 Energy-independent sampling factors (OS-4) obtained from linear fits to the EM energy fraction in TB jets (with statistical uncertainties from the fits)

	P_1	P_2 ($\times 10^{-1}$ GeV^{-1})
EM1	1.788±0.004	8.37±0.07
EM2	1.370±0.007	-4.47±0.1
EM3	1.016±0.006	-2.11±0.09
EM4	1.263±0.005	0.96±0.08
FH1	0.896±0.005	3.34±0.09
FH2	0.977±0.005	-1.99±0.1
FH3	1.247±0.006	-9.40±0.1
CH	1.011±0.005	-6.60±0.1
δ	-0.057±0.001	56.9±0.1

6.3.5 Sampling Factors that Depend on both EM Fraction and Reconstructed Energy (Scheme OS-5)

In order to exploit information about both the energy of the TB jet and its EM fraction, optimizations were carried out that included both dependences. First, the factors found in Sec. 6.3.4 (for OS-4) were applied to data, and then sampling factors were recalculated as a function of reconstructed energy as was done in Sec. 6.3.3. However, the reconstructed energy for this optimization was taken, not as E_{def}, but as the corrected energy E_{EM} found using the parameters discussed in Sec. 6.3.4.

Plots of the final factors as a function of E_{EM} are shown Fig. 6.6, and the parameters for fits to a linear dependence on E_{EM} are shown in Table 6.6. We see in Fig. 6.6 that after correcting for the EM fraction, the sampling factors are all close to unity over our entire energy range, indicating that applying both energy-dependent and EM fraction-dependent corrections is not significantly more useful than using only one of these corrections.

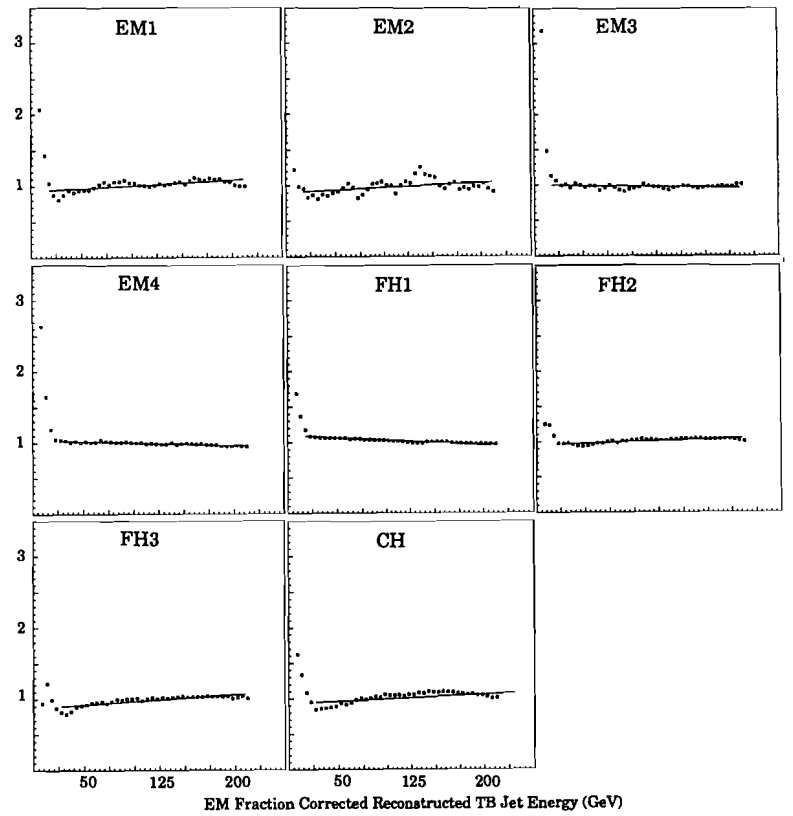

Figure 6.6 Sampling factors as a function of EM-fraction corrected reconstructed energy (OS-5). The fits are to linear functions of the form $P_1 + P_2 E_{rec}$ (see Table 6.6).

We also see in Fig. 6.6 that the sampling weights for the lowest energies show a marked difference from those for the higher energies. This indicates that using both EM fraction and energy-dependent corrections will have a negative impact on lowest-energy jets.

Table 6.6 Energy dependent sampling factors obtained from linear fits to the energy after it is corrected for EM fractions (OS-5) (with statistical uncertainties from the fits)

	P_1	P_2 ($\times 10^{-4}$ GeV^{-1})
EM1	0.927±0.003	7.65±0.02
EM2	0.898±0.003	7.29±0.02
EM3	0.998±0.003	-1.75±0.02
EM4	1.042±0.004	-4.17±0.03
FH1	1.094±0.003	-6.07±0.02
FH2	0.957±0.004	4.57±0.03
FH3	0.869±0.004	9.71±0.03
CH	0.927±0.004	6.90±0.03

6.3.6 Corrections to Reconstructed Energies

As stated in Sec. 6.2, all reconstructed TB jet energies for the default as well as for the optimized parameters were corrected using a second-order polynomial in E_{rec} (Eq. 6.3). The plots of the nominal parton energies vs. reconstructed energies are given in Fig. 6.7, and the parameters for the fits indicated are given in Table 6.7.

Table 6.7 Parameters from fits of second-order polynomial in reconstructed TB jet energy to the incident parton energy (with statistical errors from the fits)

OS-#	P_1 (GeV)	P_2	P_3 ($\times 10^{-4}$ GeV^{-1})
Default	2.41±0.02	1.13±0.01	-3.12±0.03
1	2.22±0.02	1.02±0.01	-2.16±0.02
2	-1.96±0.02	1.04±0.01	-0.96±0.02
3	1.37±0.02	0.97±0.01	1.70±0.02
4	-2.07±0.02	1.05±0.01	1.53±0.02
5	-1.97±0.02	1.04±0.01	-1.03±0.02

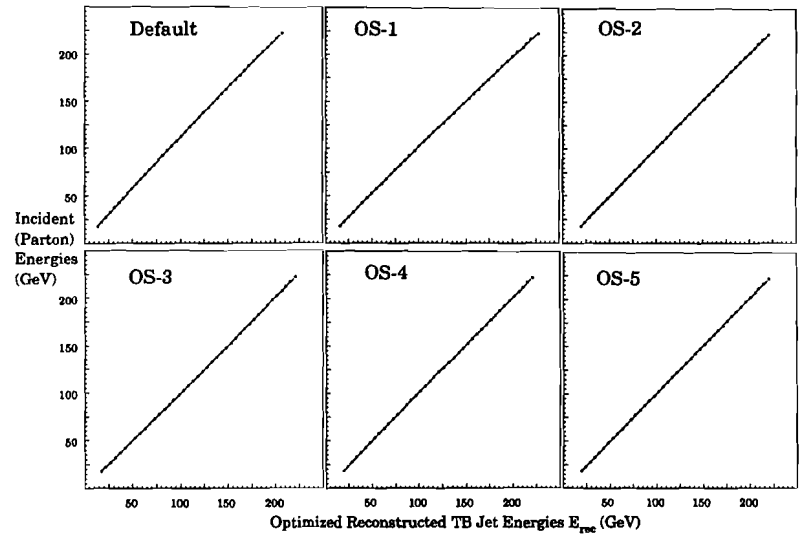

Figure 6.7 Nominal parton energy as a function of reconstructed TB jet energy for various optimizations. The fits are to second-order polynomial functions of E_{rec}.

These plots give little indication of the differences between the different response distributions. The parameters in Table 6.7 give greater detail about the differences between the various optimizations.

6.4 Judging the Success of the Optimization Schemes on Resolution

To investigate the effect of the optimization schemes on reconstructed TB jet energy resolution, a separate set of data, consisting of 218,500 events, was generated from the Particle Library. The corrections obtained from the optimization schemes were then applied as follows:

1. For each event, we calculated the default reconstructed TB jet energy E_{def}, using the default weights.
2. Choosing some optimization scheme, the appropriate sampling factors were then determined for any given E_{def}.

3. These factors were then applied to the layer energies to find the optimized reconstructed energies E^i_{opt}, for any given optimization scheme i.
4. Finally, the corrections to the reconstructed TB jet energy, based on Table 6.7, were applied to determine the final energies E^i_{corr}.

These corrected and optimized energies were then compared with the parton energies to determine the jet resolution as a function of incident energy, as explained here. The reconstructed energies E^i_{corr} were separated into bands of 5 GeV. In parallel with the rescaling of energies of singles hadrons that was based on the measurementes using PWCs (see Eq. 4.2), we also rescaled all the values of E^i_{corr} to the mean parton energy in the band. This eliminated any smearing in E^i_{corr} due to the spread in parton energies. We then calculated the standard deviation $\sigma(E)$ and mean $\mu(E)$ for each band of E^i_{corr} energies. The parameters of the resolution were then extracted by fitting Eq. 6.2 to the values of σ/μ. The parameters S and C from the fits, and their statistical uncertainties, are given in Table 6.8, and the corrected data for the various schemes with the fitted functions are shown in Fig. 6.8.

Table 6.8 Parameters describing resolution of reconstructed and corrected TB jet energies

OS-#	S (%/√E)	C (%)
Default	71.15±0.004	0.002±0.003
1	58.18±0.01	1.98±0.002
2	48.19±0.01	2.32±0.002
3	43.42±0.01	2.76±0.001
4	37.03±0.01	3.32±0.002
5	35.18±0.01	3.40±0.001

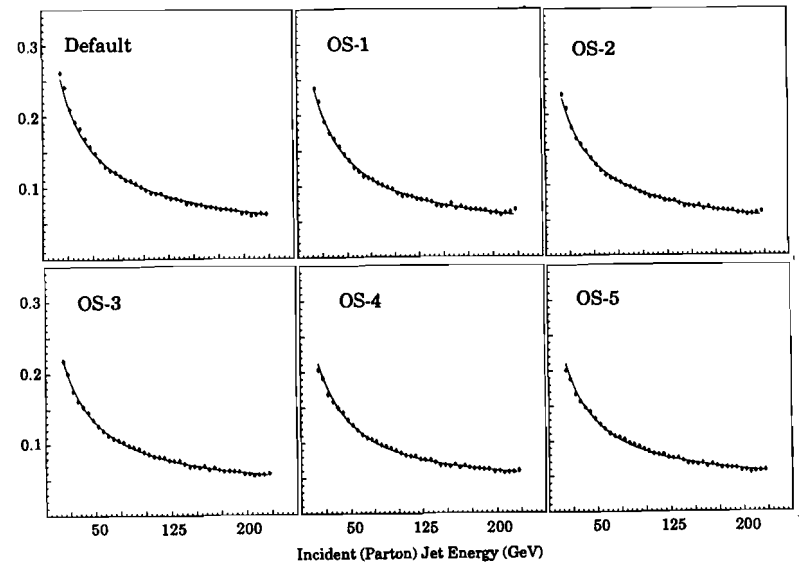

Figure 6.8 Fractional resolutions for TB jets as a function of incident energy for the various optimization schemes. Fits of the data are to Eq. 6.2

Because of the similarity of the plots in Fig. 6.8, and the fact that an increase in C can be compensated by a decrease in S in Table 6.8, if is difficult to gauge any improvement in jet energy resolution from the different optimization schemes. We therefore provide in Fig. 6.9 a comparison of the resolutions for the various schemes relative to the case using the default parameters.

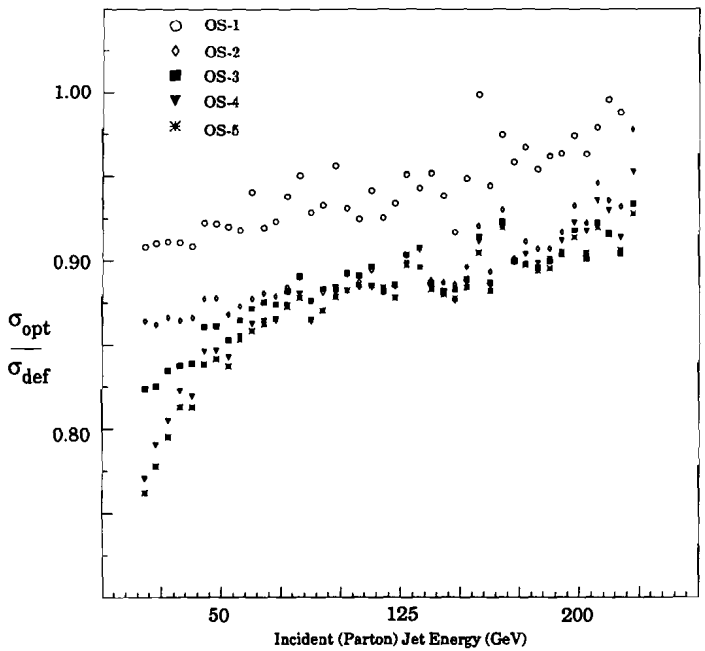

Figure 6.9 Ratio of optimized TB jet resolutions to the default values as a function of jet parton energy.

From Fig. 6.9, we see that while OS-1 improves the resolution over the default scheme, it is not as marked an improvement as those using the other schemes. The improvements for OS-2 to OS-5 are only slight at the highest energies, but more apparent at the lower energies. The OS-4 and OS-5 schemes appear to provide the best overall resolution.

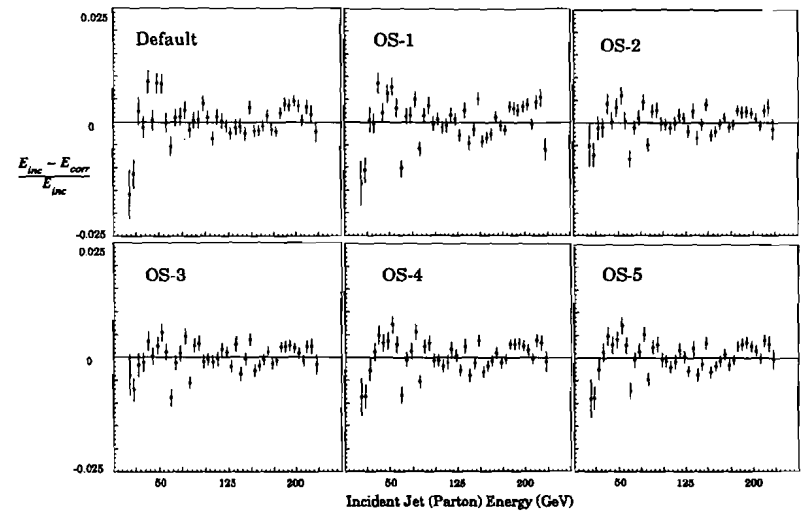

Figure 6.10 Fractional differences between the corrected reconstructed TB jet energies and incident parton energies, for different optimization schemes.

Fractional energy differences for the various optimization schemes are shown in Fig. 6.10. As can be seen in the figure, the fractional differences are all very similar, as expected, since all energy responses were corrected using a second-order polynomial in E_{rec}, (see Sec. 6.3.6). Nevertheless, this verifies that the corrections were adequate. (As we mentioned previously, when the sampling factors in Sections 6.3.3, 6.3.4, and 6.3.5 were fitted to third or fourth-order polynomials in E_{rec}, these fractional differences were not as well-behaved.)

From the results of this chapter, we see that the energies of TB jets more closely reflect the original parton characteristics (as shown by jet energy resolution) when we implement our optimization schemes. Thus, the weights suggested by single-particle optimization can be improved upon by applying a more detailed knowledge of jet structure to test beam data.

Chapter 7.

Conclusion

Electron and hadron data from the DØ test beam Load II data run, at an azimuth of ϕ=3.10 radians (3.16 DØ units) and pseudo-rapidities η=0.05 and η=0.45, and at energies of 2 GeV to 150 GeV, were used to improve the energy resolutions of simulated DØ jets. The techniques examined in this thesis outline methods that can be used to calibrate calorimeters for measuring jet energies at collider detectors. We have shown that by varying relative scales for different calorimeter layers (sampling weights), the jet energy resolution of calorimeters can be optimized significantly.

In Chapter 5, we applied a naive (although widely used) procedure to improve the energy resolution for single hadrons in order to obtain optimal sampling weights. This was done by minimizing the difference between incident and reconstructed hadron energies. We found that the resolution and linearity of the response of the DØ detector to hadrons can be improved by varying different sampling weights for individual layers of the calorimeter. Defining a default set of weights as dE/dx weights for the hadronic sections, and optimized weights for the electromagnetic sections (which were obtained by optimizing the response of the electromagnetic section of the calorimeter to electrons), we can allow all layer weights of the calorimeter to vary, and thereby improve the sampling term of the hadron resolution over the default resolution by about 10%. Such an

optimization also improves the linearity of the calorimeter's response to hadrons.

Because the purpose of improving hadron response in the test beam is primarily to improve the response of the DØ detector to hadronic jets, three restrictions were imposed on the optimization procedure in order to enhance jet energy resolution. These restrictions entailed ignoring the energy dependence, particle-type dependence, and position dependence of the sampling weights for single-particle showers. We showed that imposing such restrictions leads to a deterioration in the resolution and linearity of response for single hadrons, relative to that given by the unrestricted optimization. Requiring the response to be independent of particle-type (by choosing the layer weights for the electromagnetic sections to be the values that produce the best electron resolution, i.e., the default EM weights), causes the greatest degradation in optimal hadron resolution (an increase in the sampling term of about 4%). Nevertheless, applying even all three restrictions to the optimization still produces an improvement in the sampling term of about 3% over the resolution found using the default sampling weights. Also, allowing a simple variation in relative scale between hadronic and electromagnetic sections of the calorimeter produces an improvement in resolution that is close to that obtained using the restricted optimization, which indicates that using the full optimization gives no benefit over using a simple variation of relative scales.

However, both the restricted optimization and the variation in relative scales gives an absolute hadron response that is uniformly lower than the response to electrons. Because the relative electron/hadron response has a greater effect on jet resolution than variations due to non-linearities in energy response or due to single-particle resolutions, we conclude from the results that the default weights may, in fact, be better ones to use for reconstructing jet energies in the DØ calorimeters than the weights from the restricted optimization.

To more directly examine the effect of different layer weights on jet resolution, we simulated jets using data from the test beam. Except for the overestimated noise reconstructed for the test beam jets, and the fact that the simulation is not well implemented at jet energies below ≈20 GeV due to the lack of test beam data at low energies, the test beam jets should have properties similar to jets expected to be produced at DØ. By

varying the sampling weights, we tried to improved the energy resolution of these simulated jets. Taking account of the difference in noise, results of various optimizations show that test beam jet resolution can be improved significantly (10-15%) over that found using the sampling weights determined only from single-particle information. Different sets of energy-independent, as well as energy-dependent, sampling weights were then obtained that improve the energy resolution of all test beam jets relative to that using default weights.

Our studies suggest that up to 15% improvements in jet energy resolution can be achieved at DØ, provided that the energy deposition we have simulated using data from the test beam is sufficiently similar to that for jets in a collider environment. This being quite likely to be the case, we expect that such improvements can be implemented, and thereby provide important additional tools for studying multi-jet production, especiall in final states such as $t\bar{t}$ production where the t and $\bar{t}$ quark decay into all-jet systems. Consequently, we would argue that DØ should use different sampling weights for hadronic jets and for purely electromagnetic showers.

Bibliography

1. M. Gell-Mann, *Phys. Rev.*, **125**, 1067 (1964).
2. C. Zweig, CERN Rep. 8419/TH 412.
3. E. Eichten, et. al., *Supercollider Physics*, Rev. Mod. Phys., **56**, 579 (1984)
4. G. Alterelli, R. Barbieri, and F. Caravaglios, "Non-standard Analysis of Electroweak Precision Data (Updated with the Results Presented at the Winter Conferences)", CERN-TH-6859-93, April 1993
5. I. Aitchison and A. Hey, Gauge Theories in Particle Physics, (1982)
6. A. Clark, *Experimental Aspects of Hadron Collider Physics*, Techniques and Concepts of High Energy Physics VI, edited by T. Ferbel, (Plenum Press, 1991) 71.
7. L. DiLella, *Physics at the CERN $p\bar{p}$ Collider and Status of the Electroweak Theory*, Techniques and Concepts of High Energy Physics IV, edited by T. Ferbel, (1987)
8. G. Altarelli and G. Parisi, Phys. Lett. **153B**, 111 (1985).
9. F. Dydak, "Proceedings of the XXV International Conference on High Energy Physics", Singapore (1990), K. K. Phua, ed, World Scientific.
10. F. Abe, *et. al.*, "Lower Limit on the Top-Quark Mass from Events with Two Leptons in pp Collisions at $\sqrt{s}$ = 1.8 TeV", Phys. Rev. Let., **68**, 447 (1992).
11. V. Barger and R. Phillips, Collider Physics, page 301, Addison Wesley (1987)
12. I. Hinchliffe, *Old Phyics, New Physics, and Colliders*, Techniques and Concepts of High Energy Physics IV, edited by T. Ferbel, Plenum Press (1987)
13. R. Wigmans, "Advances in Hadron Calorimetry." *Annu. Rev. Nucl. Part. Sci* **41**, 133-85 (1991)
14. R. Wigmans, *Calorimetry in High Energy Physics*, Techniques and Concepts of High Energy Physics VI, edited by T. Ferbel, Plenum Press (1991)
15. A. Das and T. Ferbel, Introduction to Nuclear and Particle Physics, John Wiley & Sons, Inc. (1994).
16. A. Clark *et al.* (DØ Collaboration), "The Central Tracking Detectors for DØ" *Nucl. Instr. and Meth.* **A279**, 243 (1989).
17. A. Clark *et al.* (DØ Collaboration), "The DØ Vertex Chamber Construction and Test Results." *Nucl. Instr. and Meth.* 1992.

18. J-F. Detoeuf *et al.* (DØ Collaboration), "The DØ Transition Radiation Detector." *Nucl. Instr. and Meth.* **A265**, 157 (1988).

19. J-F Detoeuf et al., "Status of the Transition Radiation Detector for the DØ Experiment", *Nucl. Instr. and Meth.* **A279**, 310 (1989).

20. C. Brown *et al.* (DØ Collaboration), "DØ Muon System with Proportional Drift Tube Chambers." *Nucl. Instr. and Meth.* **A279**, 331 (1989).

21. R. Hirosky, PhD. Thesis, University of Rochester, 1993.

22. "D0 Design Report." DØ Internal Notes, #137, (1984).

23. T. Geld, PhD. Thesis, University of Michigan, 1993.

24. K. McFarland, "Design and Testing of a Calibration System for the Level-0 Trigger at DØ", D0 Internal Notes, #840, (1989).

25. M. Abolins, *et al.* (DØ Collaboration), "The Fast Trigger for the DØ Experiment" *Nucl. Instr. and Meth.*, **A289**, 543 (1990).

26. M. Abolins, *et al.*, "Hadron and Electron Response of Uranium/Liquid Argon Calorimeter Modules for the DØ Detector", *Nucl. Instr. and Meth.*, **A280:36** (1989).

27. S. Abachi, *et al.*, "Beam Tests of the D-Zero Uranium Liquid Argon End Calorimeters", *Nucl. Instr. and Meth.*, **A324**, 53 (1993).

28. De, K., "Test Beam Studies of the DØ Calorimeter with 2-150 GeV Beams", *Proceedings of the XXVI International Conference on High Energy Physics*, Aug. 6-12, 1992.

29. Bartlett J. F., *et al.*, *The EPICS System: an Overview*, Fermilab-TM-1244-fiche (1984).

30. P. Bhat, "Low Energy Beam Tests and Studies", DØ Internal Notes #1076, January 1991.

31. P. Bhat, Private Correspondence.

32. D. Owen, Private Correspondence.

33. M. Tartaglia, "1990 NW Beamline Performance", DØ Internal Notes #1076, January 1991.

34. T. Geld, K. De, and J. Borders, "Test Beam ICD DST Format", DØ Internal Notes #1271, February 1992.

35. K. Streets, "The DØ Test Beam Load 2 Gain Calculation", DØ Internal Notes, #1600, 1993.

36. W. G. D. Dharmaratna (DØ Collaboration), "Reconstruction of the Calorimeter

Response- Test Beam Load 2", DØ Internal Notes, #1731 (1993).

37. CERN Program Library, CERN document 1989.05.30 (1989).

38. D. Kewley, G. Blazey, J. Chiu, T. Ferbel, "Improving Energy Resolution of Calorimeters Using a Covariance Matrix Approach", *Nucl. Instr. and Meth.*, **A280**, 36 (1989).

39. F. Paige and S. Protopopescu, BNL Report no. BNL38034, (1986, unpublished), release v. 6.49.

40. I would like to thank R. Astur for supplying the Isajet events used in this analysis.

41. S. Feher and C. Stewart, "Test Beam Alignment", DØ Internal Notes #1653, (1993).

42. K. Streets, Private Correspondence.

Appendix A.

The DØ Test Beam Transporter

The DØ calorimeter modules surround the interaction region of the proton and antiproton beams. Particles from the interactions enter the detector at different positions and angles. The response of the detector must therefore be calibrated at all these coordinates, and the best way to perform such a calibration is to illuminate the detector with particles of known energy and particle type. For this purpose, modules from representative regions of the DØ calorimeter were placed in a special cryostat that was positioned in a test beam. Two primary tests of DØ modules were performed in this manner: Load I, which contained modules from the DØ End Calorimeter; and Load II, which contained modules from both the DØ Central Calorimeter and the End Calorimeter. The two test beam configurations are sketched in Fig. A.1. A transporter system was designed to move the test-beam cryostat relative to the incident beam in order to study the response of the calorimeter modules as a function of position and entry angle of the beam particles. This Appendix describes the features of the Transporter.

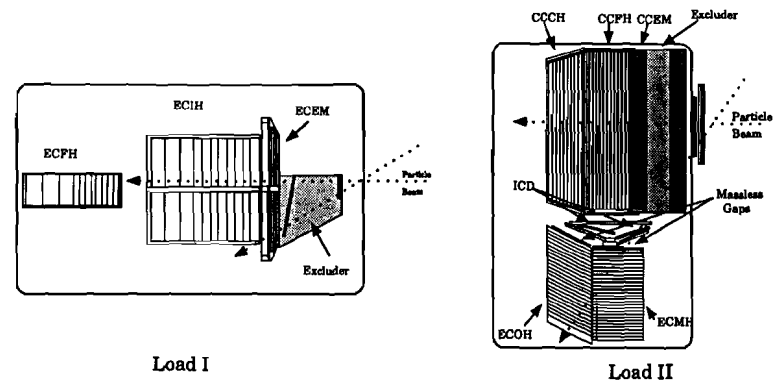

Figure A.1 Calorimeter modules studied in the DØ test beams.

A.1 Design Specifications of the Transporter

The Test Beam Transporter system is required to move a large cryostat, containing massive but delicate modules in a bath of liquid argon, through a wide range of motion in four degrees of freedom. The loaded cryostat, including the attached plumbing, support structures, modules, and liquid argon, weighs about 75 tons.

In order to ensure reproducibility of the data runs, the overall placement accuracy of the transporter was required to be about 1/3 of the size of the beam spot (which was about 4 cm wide and 2 cm high). In addition, a sophisticated readback system was required to monitor position settings to better than 1 mm for studies of the dependence of response on position in the calorimeters. The range of motion had to be sufficiently large to cover all calorimeter regions of both Load I and Load II. Finally, the speed and acceleration of the movement had to be limited to prevent any shifting of the modules within the cryostat.

Since the beam studies involve a large range of highly precise motion, an interactive system of motion control was required, in which coordinates of the DØ coordinate system ("DØ coordinates") can be specified in terms of η, ϕ, and the interaction *z-vertex*

by an operator. The transformations from these coordinates to the transporter system ("NWA coordinates") require a computer-driven interactive control system that can be programmed to handle the coordinate transformations. Finally, a variety of safety control systems must be built into the control system (electronically, mechanically, and through software), to conform with strict limitations on the ranges of motion due to the somewhat restricted space in which the cryostat is located.

A.2 A Description of the Transporter System

The test beam transporter and cryostat are located in the NWA (Neutrino West Line, Building A). The transporter can be controlled via an electronic control panel (referred to as "manual control"), or via a software-driven computer interface. Both control systems will be described in detail below. A sketch of the cryostat in relation to the NWA building is given in Fig. A.2. The cryostat and transporter system reside in a pit 2.92 meters deep, so that the incoming particle beam (1.52 meters above the NWA floor) enters the cryostat at the proper height.

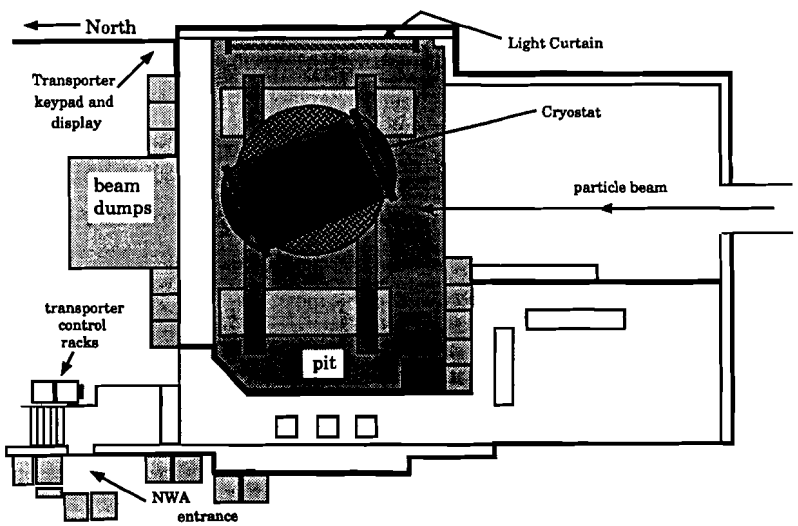

Figure A.2 NWA Test Beam cryostat and transporter layout

The pit and the immediate upstream area are enclosed by mesh fencing for reasons of radiation safety. Also, concrete and steel radiation shields, and enclosed beam dumps, are used to protect the environment and the experimenters from any stray radiation. As shown in Fig. A.2, the control electronics for the transporter are located in a pair of racks near the central entrance to the NWA building, with a manual control panel mounted on the side of one of these racks.

A.2.1 Motion of the Transporter

A rough sketch of the transporter and cryostat system is shown in Fig. A.3.

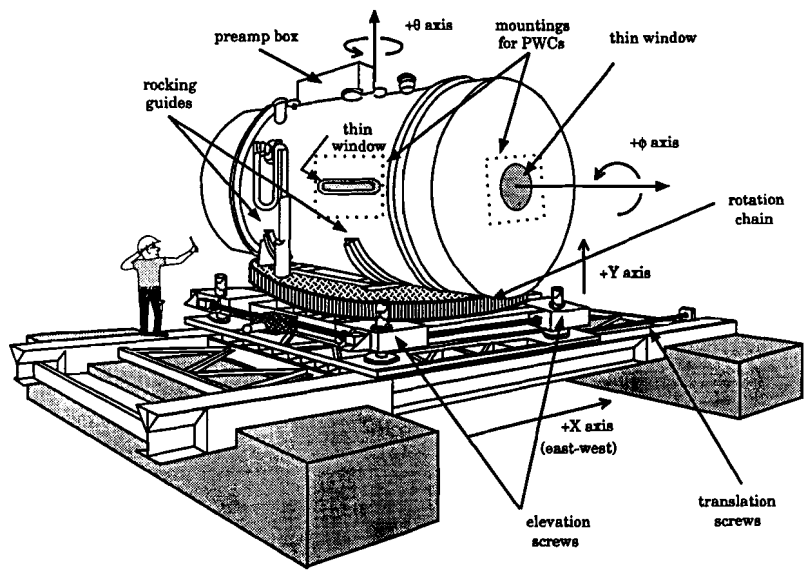

Figure A.3 Sketch of test beam cryostat and transporter

The entire system is moved by four motors, one for each axis. *Translation* in X (translation) is provided by motion of two horizontal east-west screws, and *elevation* in Y by four vertical screws. *Rotation* in θ is performed with a chain wrapped around the circular transporter table. *Rocking* motion in ϕ is implemented with a horizontal screw,

producing motion along rocker guides located around the cylindrical cryostat.

Readback of the positions for each axis is monitored dynamically through the use of a set of displacement transducer devices, named "string-eaters". These devices consist of an internal spool containing a stainless steel cable. The end of the cable can be attached to some part of the transporter system, while the transducer is mounted on some base (fixed with respect to that axis). As the transporter moves, the cable is extended from or retracted into the spool, producing a measurable digital signal in a VME readback system (shown later). The VME control electronics provide a full-precision position signal to the on-line data acquisition system, and a coarser-precision readback to the transporter software control system for placement of the transporter. There are four string-eaters for the elevation, two for the translation, and one each for rotation and rocking. The rotation string-eater rests on an arc-shaped piece of metal that guides the cable around the circular transporter table.

The placement accuracy, readback precision,[41] range of motions, and maximum velocities for all four axes are presented in Table A.1.

Table A.1 Transporter motor parameters of motion

Axis	Range	Velocity	Placement Accuracy	Readback Precision
elevation (Y)	76 cm	5 cm/min.	0.5 cm	0.8 mm
translation (X)	366 cm.	10 cm/min.	0.5 cm	0.2 mm
rotation (θ)	190°	3°/min	3.0 mr	0.3 mr
rocking (ϕ)	28°	3°/min	1.5 mr	0.2 mr

A.2.2 The Cryostat PWC

A proportional wire chamber (PWC) mounted upon a table assembly was attached to the front face of the cryostat for Load I, and was moved to the side of the cryostat for Load II. The places where the PWCs are attached for each Load are indicated in Fig. A.3 by the dashed rectangles around the thin beam-entry windows. For Load I, the fixed base of one table was mounted upon the side of the cryostat, the second table was mounted upon the first, and the PWC was mounted on the second. For Load II, the fixed base of the table was mounted on the face of the cryostat, and the PWC was mounted on the table.

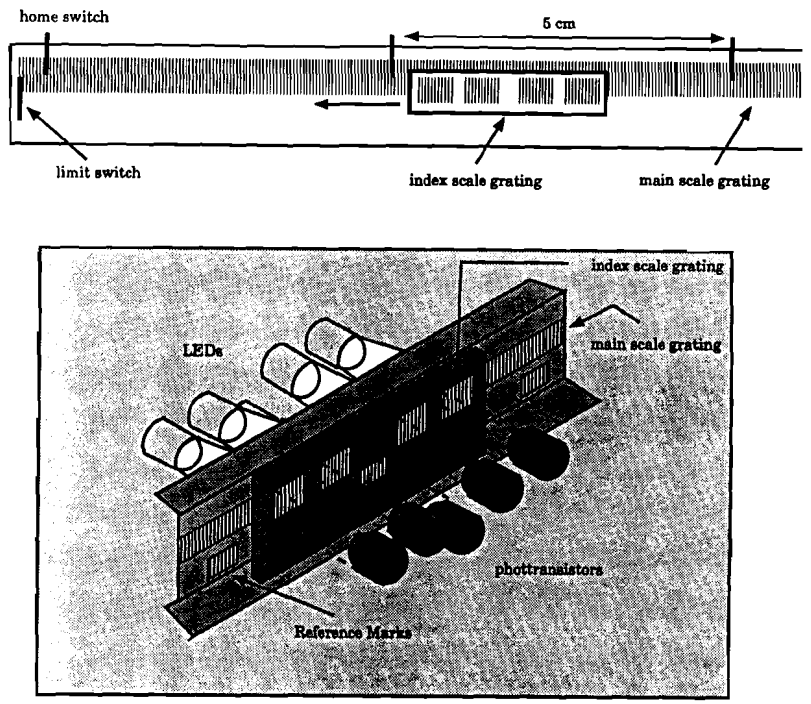

Figure A.4 Linear scales on tables used for mounting the Cryostat PWC

Linear scales to measure the position of the tables are located on the bases of the tables (see Fig. A.4). The encoder for each linear scale consists of four pairs of LEDs and photodiodes, a main scale grating, and a reference scale grating. The scale gratings are of 20 μm pitch. The index scale grating moves along the main scale grating, along with the pairs of LEDs and photodiodes. Light from the LEDs shines through both sets of gratings, and is detected by the photodiodes. The system provides a resolution of 5 μm.

The position of the table is measured by an electronic single-axis multiplier (SAM) device, that keeps a count of signals produced by the linear scales. The system is zeroed

using a "home" switch located at the extreme negative limit of travel; thus, if the SAM loses track of the position, the entire table must be returned to the home position to be recalibrated. The current position can be lost, for example, in the case of a power outage. Calibration marks on the linear scales are located every 5 cm, so that a SAM can check if it has lost its position at these points. Also, limit switches at either end of the range prevent the table from continuing off the end of its track.

The position of the table is passed to the VME system, which passes a precise measurement of the position of the PWC to the data acquisition system, and which generates a coarser measurement for the transporter software control system. The resulting placement accuracy is ± 1 mm, and the readback precision is ± 5 μm, for the 50 cm range of travel.

A.3 The Safety System

Four principal safety features are included in the transporter design. They are in effect whether the transporter is being moved manually or via software controls. The individual components are described below.

1. Current-sensitive relays are built into the motor drive system, are designed to trip if the current to the motors goes over a prescribed limit. Thus, in the event that some obstruction blocks the motion of the transporter, the current increase will trip a relay before damage is done to the transporter. In the event of a trip, the relays must be reset manually at the manual control panel (which will be described in Sec. A.6.1). The current limits were set by trial and error, by turning screws in the relays until they did not trip under normal running conditions.

2. Limit switches are located at the extreme ranges of each of the axes of travel are designed to prevent the system from either going beyond the safe limits of motion, or crashing into the walls of the pit. When the transporter reaches a limit switch, motion for that axis is only allowed in the reverse direction.

3. A "light curtain" is installed along the east wall of the pit, because the limit switches cannot be configured to prevent the cryostat from running into that wall without requiring an unacceptable limitation in the degrees of freedom. This refers to a group of horizontal beams of coherent light and light sensors placed in a vertical row parallel to the east wall. In the event that any object interrupts any of the beams of light, a relay is tripped in the control electronics, cutting the power to all drives.

4. Each drive has a clutch built into the linkage between the motor and the drive system. Thus, if a mechanical obstruction interferes with the motion along any axis, that motor will disengage. Also, metal plates at the physical limits of the motion of each axis activate the drive clutch to prevent the transporter from falling off the table.

There are, in addition, software safety features built into the control program (described later) to prevent a variety of mishaps from occuring. These features do not affect the manual control of the transporter, and are described below.

1. The program will stop the motion along any axis before it reaches a prescribed limit at each end of the allowed travel. These limits are usually set to points just inside the physical limit switches.

2. The program checks each position that the transporter is commanded to proceed to ("command position") before commencing motion. By calculating a "virtual volume", that surrounds the cryostat, the program determines if the final position will result in some portion of the transporter striking some obstruction. For example, none of the physical or software limits, or even the light curtain, can be configured to prevent a special combination of coordinates that result in the preamp box striking the east wall of NWA. The software boundary prevents such an occurrence.

3. The program continually monitors the positions of the X and Y axes using both the motor encoders and the string-eaters. If a sizeable discrepancy exists between any two readouts on either axis, the program will halt and prevent further motion until the problem is diagnosed and corrected.

Finally, there are warning and safety features available for personal protection of the operator of the transporter as well as any individuals in the transporter area:

1. There are warning lights in the pit area that flash whenever the transporter is enabled.
2. There are large red crash buttons located near the stairs in the pit at the southwest and northeast corners, that, when pressed, interrupt all power to the transporter and disable it immediately, until a reset button is pushed on the manual control panel.
3. There are halt buttons both on the manual control box and on the software control keypad that halt all motion when activated.
4. The main power switch is located near the manual control box, and can be thrown by any concerned observer. This power switch is locked in the off position when the transporter is not in use, to prevent unauthorized motion of the transporter.

A.4 The Control System Electronics

The software control system for the transporter consists of a control chassis containing the control electronics, 4 motor drivers that control the motion of the motors, the PWC controls, and readback interfaces for monitoring the position of the various transporter components. In addition, a manual control panel is included for direct control of the transporter axes. A sketch of the layout of the system is given in Fig. A.5.

Fig. A.5 also shows the location of the VME interface, which monitors data from the string-eaters and from the cryostat PWC. The main power switch is located opposite the manual control box.

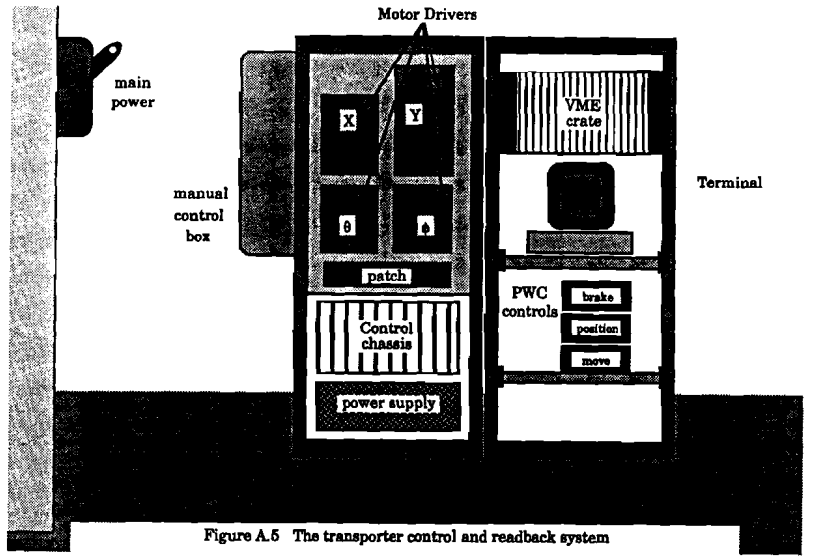

Figure A.5 The transporter control and readback system

The transporter computer-control is based upon a Motion Plus™ system produced by MTS Corporation. MTS also supplied a control chassis, which houses electronic cards that control the functions of the system, including one system processor card which is used to run the software control program, one CRT interface, four command generators, four encoder translators, and four I/O cards to provide control of the transporter system. A description of these components is included here.

The main components of the system processor card are an 8 MHz Intel 80188 CPU (essentially the same as a 8088 CPU), 64 KB of RAM, and a serial port. Programs are written and compiled on a host computer, downloaded through the serial port into the RAM, and then executed on the CPU to control the motion of the various axes of the transporter system.

Each axis of motion has an individual *command generator*, which is a card using an on-board microprocessor (an Intel 8085A-2) to process motion profile (a description of the planned acceleration, velocity, and deceleration) data from the main CPU, and then

to control the motion of a drive motor. The command generators can sense the motion of the motor, and provide rapid profile modifications dynamically.

Each axis also has an *encoder servo translator*, which utilizes command pulses and direction information from a command generator, reads the measured position of the motor, and provides appropriate motor control signals to the individual motor.

The host computer, a PC-compatible Ast Premium/286, was maintained near the cryostat during the initial software development of the control programs. MTS provided an IDE (integrated development environment) to produce programs for running on the processor card. The IDE also contained an interface to directly control the downloaded program. A CRT interface is also utilized to produce textual information on a small video display. Coupled with a remote keypad (which uses one I/O card to communicate with the system), a CRT provides control of the transporter program away from the host PC.

The I/O cards have 32 discrete Input/Output lines which can be connected to external devices to control peripherals, receive input from control devices, and monitor I/O information from position measurement devices. The bi-directional I/O ports use 0 or +5 V (at 10 mA) levels to indicate off or on states, respectively. Each port can be assigned as either an output or an input line.

One of the I/O cards is used to interface with a remote keypad, which, along with the CRT, is located near the cryostat for local operation of the transporter (see Fig. A.2). The other three I/O cards receive data from the VME readback system about the positions of the string-eaters and the PWC, and are also used to interface with the beam trigger electronics to detect when beam is being received and to notify the data acquisition system when the transporter is being moved.

A.5 The Transporter Control Program

The transporter software control system is intended to provide an interactive and convenient method for any operator to specify DØ coordinates and have the transporter place the cryostat in the appropriate position. As mentioned above, the system also provides safety features and controls the cryostat PWC. In addition, the system can move

the transporter through a pre-defined list of positions during position scans, while interacting with the data acquisition system to prevent motion of the transporter during data-taking. The program that controls this wide range of activities is described below.

A.5.1 Brief Summary of the Programming Language

The transporter control program is written in a custom language, INCOL86, an improved version of INCOL (INdustrial Control-Oriented Language), which is designed by the control-systems manufacturer (MTS Corp.). The language uses a very fundamental set of commands for motor control, and has limited mathematical and text I/O commands for user interaction. Also, only a finite number of pre-named variables are available, which are shared among all subroutines and functions in the program. The variables are named according to their nature, and there are 256 of each type. For example, character strings are labeled S0 to S255, integers are I0 to I255, etc. Due to the limitations on variable names (strings of letters and descriptive names cannot be used), and the fact that all variables are shared, a strict record must be kept of which variables were used for what purpose and in what routines. This list of variables is in the file VARIABL.TXT.

Programs written INCOL86 are multitasking, and are composed of *tasks*. Each of these tasks is identified within the program by name, and no name can be used twice. The tasks can either be *started*, by a START command, or *executed*, with a DO command. When a task is started, the calling task then immediately proceeds with its next step. When a task is executed, the calling task waits until the required task is performed before going to the next step. Any program is simply a group of tasks, any of which can initiate any others, and all of which share the same common variables.

A.5.2 The Transporter Program

We include a brief description of the transporter control program, both for a reference, and to aid in future modifications of the code.

The program consists of a main calling task, INIT, which starts a variety of other tasks. The program can be broken down into three main tasks, MENU, SETMON, and ALARMS, each of which fills a fundamental purpose in the program. MENU continu-

ously scans for input from either the host PC or the numeric keypad, and takes the appropriate actions when given input, such as entering new positions, moving the transporter, resetting the PWC position, or starting special tasks. SETMON runs a continuous loop to read the PWC and transporter positions and status, and print the relevant information to the display screen. ALARMS is intended to continuously monitor the status of various safety features of the system, and notify users of the source of the problem when something an alarm condition occurs. However, the test beam data runs ended before the completion of the ALARMS package, so that ALARMS is not fully implemented, although its framework is in place.

A task SETUP is called by INIT at the beginning of the program. SETUP, which runs once and then terminates, initializes the system by setting the motor encoder positions (which are set to an arbitrary scale and position when the program is downloaded) equal to the string-eater positions, homing and resetting the PWC (which must be done when power to the system is lost), etc.

A map of the most important tasks in the transporter control program is given in a flow diagram of the program in Fig. A.6. Major routines (that run continuously and perform many functions) are distinguished from "service" routines (such as those that read the keypad or calculate new positions), by indicating the former in uppercase and the latter in lowercase. Some routines are not represented in the diagram, but are described below.

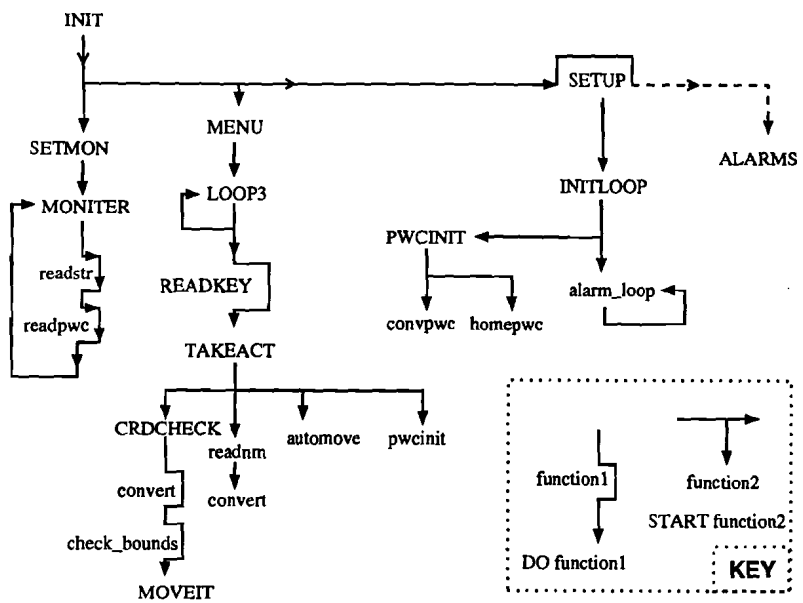

Figure A.6 Diagram of transporter control program

We include a list of all the tasks and a brief summary of their function. In parentheses, we include the calling program or programs of the tasks, if they are not given in the sublists.

1. INIT: starts the program.
2. SETMON (INIT): monitors the positions of the transporter and PWC, and prints these positions to the screen.
3. MENU (INIT): watches for input from the keypad and PC, and performs the actions selected.
   a. inv1: simple routine to invert text for menu selections, without conflicting with print commands from other routines running in parallel.
4. SETUP (INIT): initializes all variables and startup conditions of the program.
5. ALARMS (INIT): currently not implemented.
6. MONITER (READKEY, SETMON): continuous loop to print posi-

tions to screen for SETMON.
   a. moving_init: since the ranges of motion for X and θ are greater than the motor encoders can measure, moving_init resets the encoders when their internal limit is reached.

7. LOOP3 (MENU): continuous loop to check for keypad or PC input.
8. READKEY (LOOP3): wait for input from either PC or keypad.
   a. padread: reads commands from keypad
   b. pcread: reads from PC
   c. padent: enters numbers from keypad
9. TAKEACT (LOOP3): take whatever action requested by operator.
10. automove (TAKEACT): commences predefined series of movements while communicating with the data acquisition and beam trigger system for position scans.
11. CRDCHECK (TAKEACT): checks if coordinates are within bounds, calls routine to convert to NWA coordinates, and then moves transporter.
   a. convert: converts DØ coordinates to NWA coordinates.
   b. check_bounds: verifies that new position is acceptable (virtual box around cryostat).
      (1) r_bounds: checks if preamp box is close to any obstructions
      (2) box_bounds: builds virtual box around cryostat to check for problems.
12. MOVEIT (CRDCHECK): controls the movement of the transporter and PWC.
   a. movall: determines which axes should be moved, then initiates motion.
      (1) move1: moves axis 1 (Y).
      (2) move2: moves axis 2 (X).
      (3) move3: moves axis 3 (θ).
      (4) move4: moves axis 4 (ϕ).
   b. movepwc: starts pwc motion.
      (1) loop10: loops until PWC is in position, then stops PWC motion.
13. INITLOOP (SETUP): initializes all axes, homes PWC, resets all variables.
   a. init2: performs special initializations of tranlation (X) axis.
   b. init3: performs special initializations of rotation (Y) axis.
   c. PWCINIT: controls calculation of new PWC coordinates and homes the PWC.
      (1) convpwc: calculates new PWC positions based upon transporter command positions.
      (2) homepwc: moves PWC to negative extreme, then moves it to positive until the coordinates are properly set.
   d. ALARM_LOOP: loops continuously comparing translation string-eater values to make sure there isn't a great difference between any two values of the X and Y axes (a safety feature).

A.6 Using the Transporter Control Systems

The manual control system is intended primarily for use during mechanical maintenance when there is no data-taking. It allows direct manipulation of the motion of each axis, but provides no readback information or DØ coordinate information. The software-controlled system provides computer-aided calculation of destination parameters and computer-controlled motion of all transporter axes. We will discuss both options below.

A.6.1 The Manual Controls for the Cryostat Transporter

The manual controls for the transporter are mounted on the side of the rack that contains the electrical system for the the motor control (see Fig. A.5). A sketch of the manual control system is given in Fig. A.7.

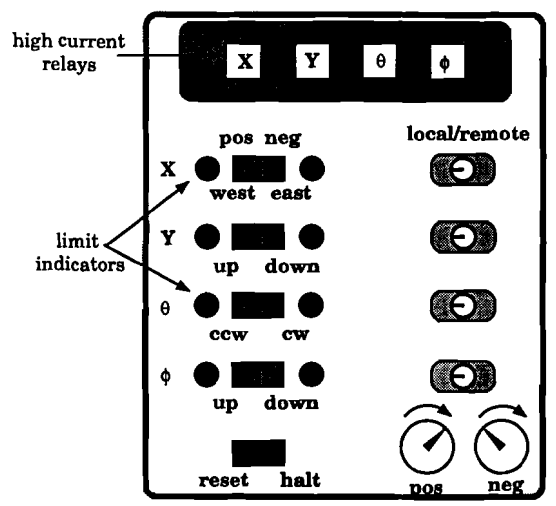

Figure A.7 Manual controls for transporter

The manual controls for the cryostat transporter consist of a set of reversible polarity DC voltage pots. These pots adjust the voltage (0 to 10 volts) connected to the trans-

porter motors, thus providing direct control over the motion of each axis. A key is required to put any axis into "local" mode, which refers to using the manual control system, as opposed to "remote" mode, or control by the transporter control program (described below).

Each axis has a positive and negative button, only one of which can be turned on at a time. Once pushed, turning up the voltage pot for that polarity will cause motion in that direction. Simultaneous motion along multiple axes in the same or different directions is also possible, but the voltage is the same for all axes going in the same direction (since there is only one pot for each polarity). The directions are labeled according to motion: X, Y, θ is clockwise (+) or counter-clockwise (-) as viewed from above, and ϕ "up" is the direction that rotates the preamplifier box on the side of the cryostat upward.

In the event of a current relay trip or light curtain activation, the "halt" button must be pushed and held in for several seconds until the relay is reset (signaled by an audible "click").

A.6.2 The Manual Controls for the Moving PWC

The moving PWC contains a set of readback and control boxes which can be used in conjunction with or separate from the computer control system, as shown in Fig. A.8. For Load I, there were two sets of three controls, one set for each degree of freedom (vertical and horizontal). In Load II, there was only one set, for horizontal motion.

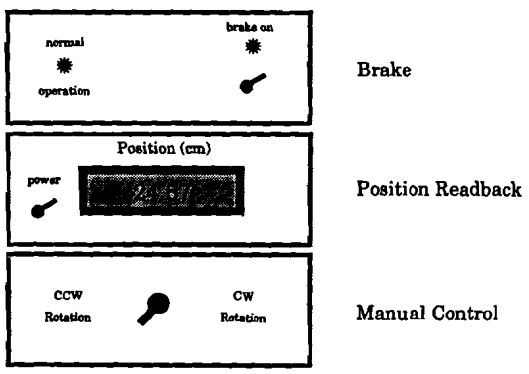

Figure A.8 Manual controls for the cryostat PWC

The top box is a brake, which halts the motion of the PWC, overriding both the software and hardware control, to prevent possible motor drift due to anomalous currents in the control system. In normal operation, this brake is off. During the course of the Test Beam runs, the brake was never used.

In the middle is a position readback device and power box. Turning off the power on this box disables the PWC motion, and also erases the current PWC positions from the control electronics. The position is read out in the range ± 25 cm, with zero corresponding to when the PWC table is centered.

The lowest box provided manual movement of the axis of the PWC. A toggle switch enables either clockwise or counterclockwise motion of the driver motor of the axis, and the resulting position changes can be observed on the readback LED. The switch is simply a bi-directional DC voltage source connected directly to the drive motor (0 or 10 V).

A.6.3 The Computer Control System

The interface for the computer control system consists of a video screen and a keypad, located near the northeast corner of the pit (see Fig. A.2). The video screen displayed information about the positions of each axis of the transporter, as well as allowed a command interface for entry of data from the keypad. A diagram of the display and the keypad are shown in Fig. A.9.

The top half of the display gives status information about the transporter and the moving PWC. The second line, LOCATE, tells whether the axis is in the command position or off position. The second line, STATUS, reports "STILL" if the motor is not turning, and "MOVING" if it is in motion. The third line, PWCSTS, gives information about the moving PWC, reporting its axis positions (since this information is of primary importance only to experts, the display does not clearly label the axes. Instead, the number in the X column is the command position (cm) of the X axis, and the number in the THETA column describes the current position of the PWC X axis. For Load I, the other two columns also reported similar information about the Y axis.

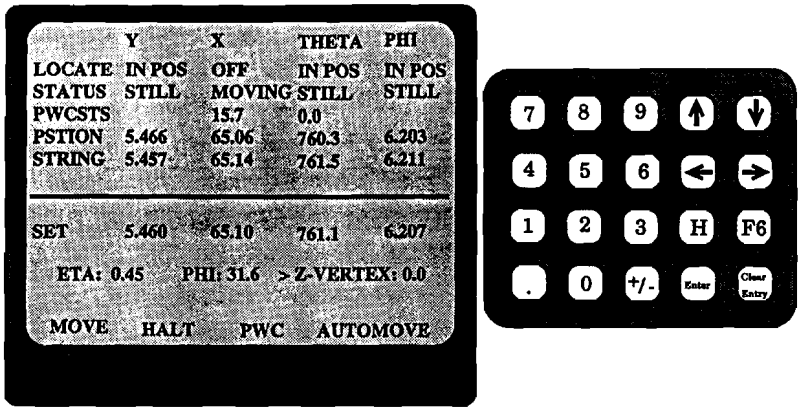

Figure A.9 Remote keypad and display for computer-controlled transporter system

The fourth line, PSTION, reports the current position (inches for X and Y, milliradians for θ and ϕ) of the motors as determined by the encoder motor control system. (The encoders keep an internal count of motor revolutions, and translates them to arbitrary, specifiable, units). The fifth line, STRING, gives the positions as reported by the string-eaters. These positions are the most relevant ones, and when the motor system is reset, it is calibrated by the string-eater positions.

Differences between PSTION and STRING values indicate a discrepancy in the encoder position, and the program automatically resets the encoder positions when sizeable differences occur. This is a somewhat common occurence, especially for the rocking (ϕ) motion, since the motion is rotational, but controlled by a linear screw (so the rotational position is not linear with the number of motor revolutions). The values of the two numbers are always somewhat different, as the precision of the placement is not as great as shown on the screen.

The bottom half of the screen is used to input command information to the program. The first row of numbers indicates direct command positions for each axis: X, Y, θ and ϕ. The second row indicates the desired DØ coordinates, in η, ϕ, and *z-vertex*. Whenever coordinates are changed in the second row, all coordinates for the first row are automatically recalculated to reflect the NWA coordinates needed to simulate the requested DØ position. However, since the positions of the transporter in NWA coordinates do not always correspond to DØ coordinates, an entry in Row 1 does not affect the numbers in Row 2.

The cursor (shown as a ">") can be moved between the various values of the first two lines using the arrow keys on the keypad (the arrow keys and the "H", or HALT keys, are keys F1 through F6 on the keypad, but an adhesive label has been placed over them to label them as shown). Then, the value of the selected position can be changed by: 1) pressing the ENTER key to indicate to the program that the data entry mode is required, 2) typing in the desired command position, and 3) pushing the ENTER key again to terminate data entry.

Once all axes show the desired command positions, the MOVE option can be selected to start the motion of the transporter, by moving the cursor to that option, and pressing ENTER. (When the cursor is in the bottom row, selections are indicated by reversing the video of the text for the selected option, to differentiate "action options" from "data entry options"). Also located on the bottom row is the HALT option, which completely halts and resets the system, resetting all encoder positions to the string-eater positions, and freezing all axes until MOVE is selected again. The PWC option resets the PWC table, by zeroing the PWC, then moving to the appropriate PWC position (recalculated to center the PWC on the beam). The PWC option is useful when the transporter is moved manually.

The bottom row also contains the AUTOMOVE option. When this is selected, a predefined sequence of moves is initiated. In this sequence, the transporter and PWC are automatically moved to some coordinate in a list, the transporter waits until one complete beam spill passes from start to finish, and then moves to the next coordinate in the list.

Appendix B.

DØ Particle Library

The Test Beam Particle Library was created to provide a source of fully corrected particle showers from data from the test beam. It was originally designed for simulating DØ jets from test beam particles (TB jets). However, the Particle Library has also been gaining popularity as an easily accessible source of single-particle showers. In this Appendix, we describe the data contained in the Particle Library, as well as the procedure used to construct simulated jets.

B.1 Contents of Particle Library

The Particle Library contains data from the test beam on hadron and electron showers that have information on signal response stored on a cell-by-cell basis. The Library has showers in the energy range from 2 GeV to 150 GeV, taken at the pseudorapidity η=0.05 and azimuth ϕ=3.10 radians (3.16 in DØ units) in the central calorimeter. Any set of showers (or *events*) in a particular energy range is known as a *field* of events. Using PWC information, these events have been renormalized for small dispersions in incident momentum. All required corrections to the showers were made directly at the input stage, including corrections for cell-by-cell plate thickness variations (obtained from survey data of the module structure), gain corrections, and capacitance

corrections (due to the use of longer readout cables in the test beam than at DØ). Also, by using inspill pedestal data to perform pedestal subtraction upon the data, the standard test-beam analysis software was bypassed to avoid previously existing problems.[42] Finally, events were selected using information extrinsic to the calorimeter, i.e., scintillation counters were used to detect muons and MIPs that passed through the calorimeter, Cherenkov counters were used to select electrons and pions, "hot cells" were found using pedestal data, etc. No further data selection was performed using the calorimeters, which thereby defined an essentially unbiased sample of events, comparable to that expected in DØ. Also, there was no zero-suppression performed on these data.

Histograms of the total energy spectra for data stored in the Particle Library are shown in Fig. B.1, B.2, B.3, and B.4, for hadrons and electrons. The number of events, the mean reconstructed energies (using optimized electron weights for the electromagnetic sections,[36] and dE/dx weights for the hadronic sections), and the RMS widths of the distributions are given on the graphs. The parameters (not given) obtained using Gaussian forms fitted to the data, are in rough agreement with the calculated means and widths given in the figures. (Fits to the Gaussian forms are shown in the graphs.)

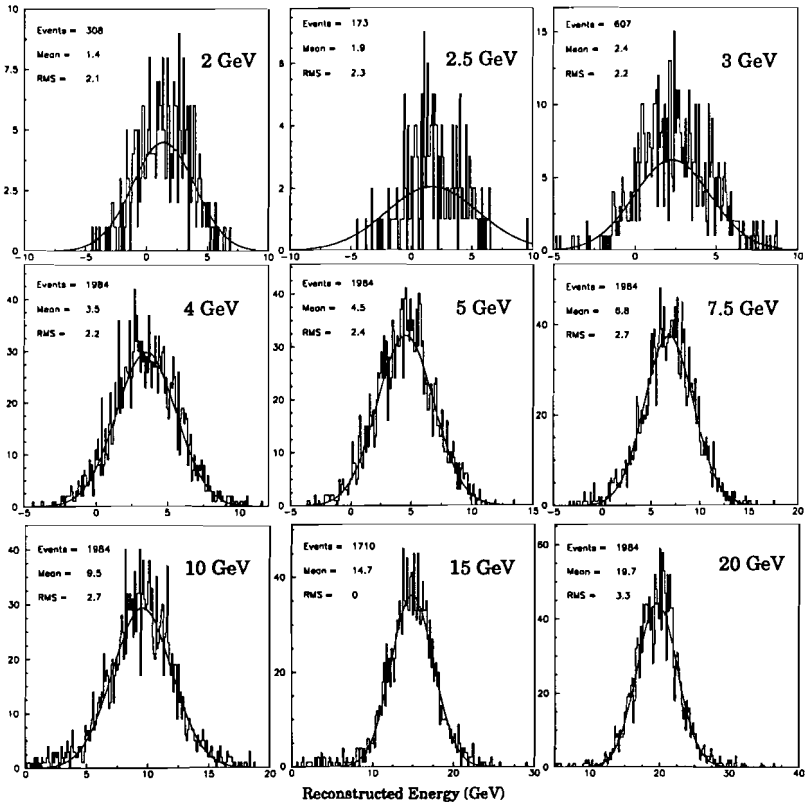

Figure B.1 Particle Library hadrons from 2 GeV to 20 GeV

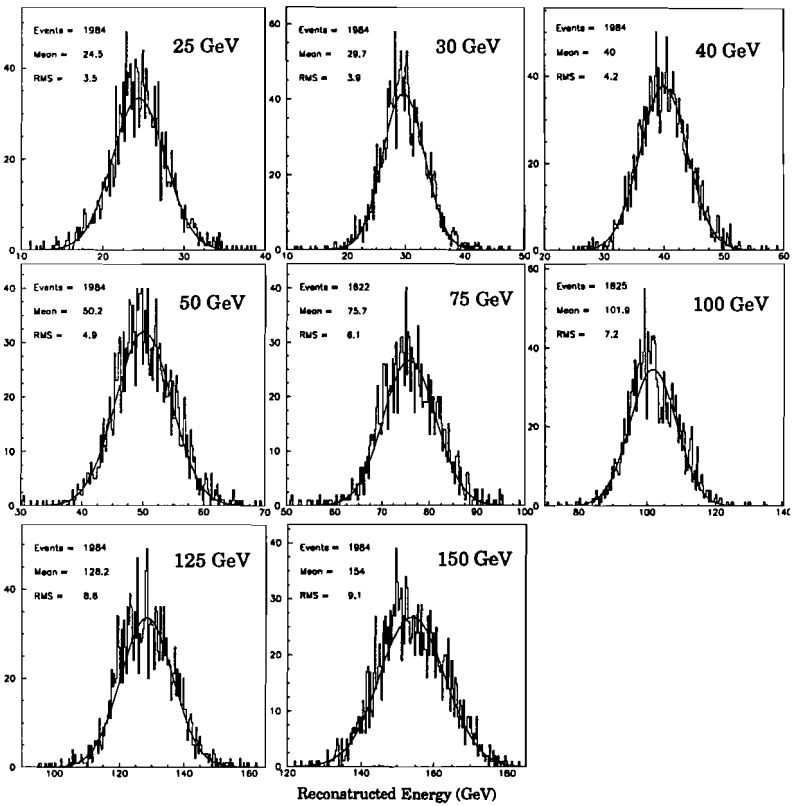

Figure B.2 Particle Library hadrons from 25 GeV to 150 GeV

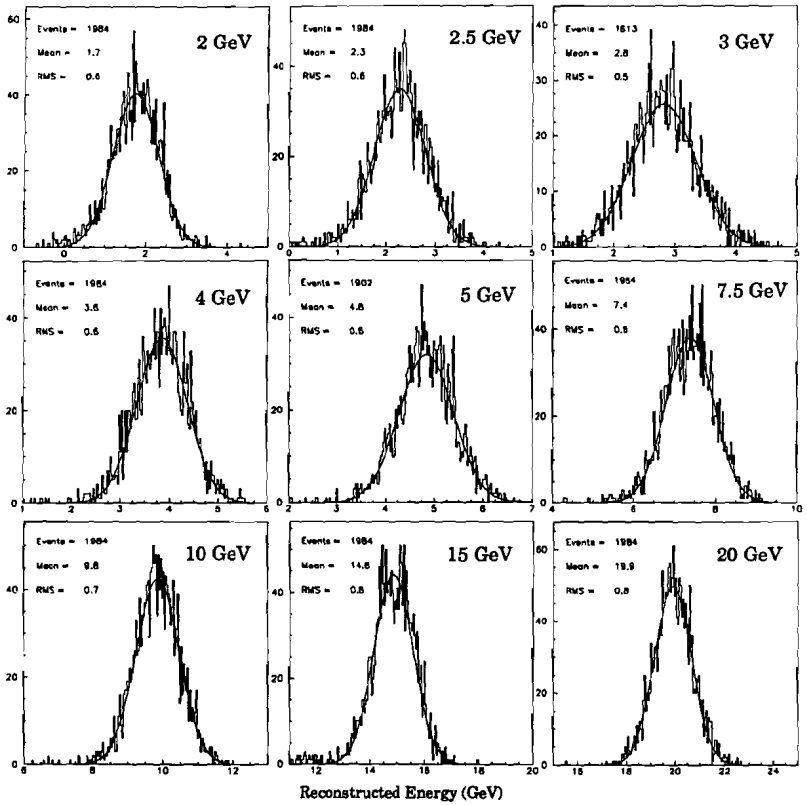

Figure B.3 Particle Library electrons from 2 GeV to 20 GeV

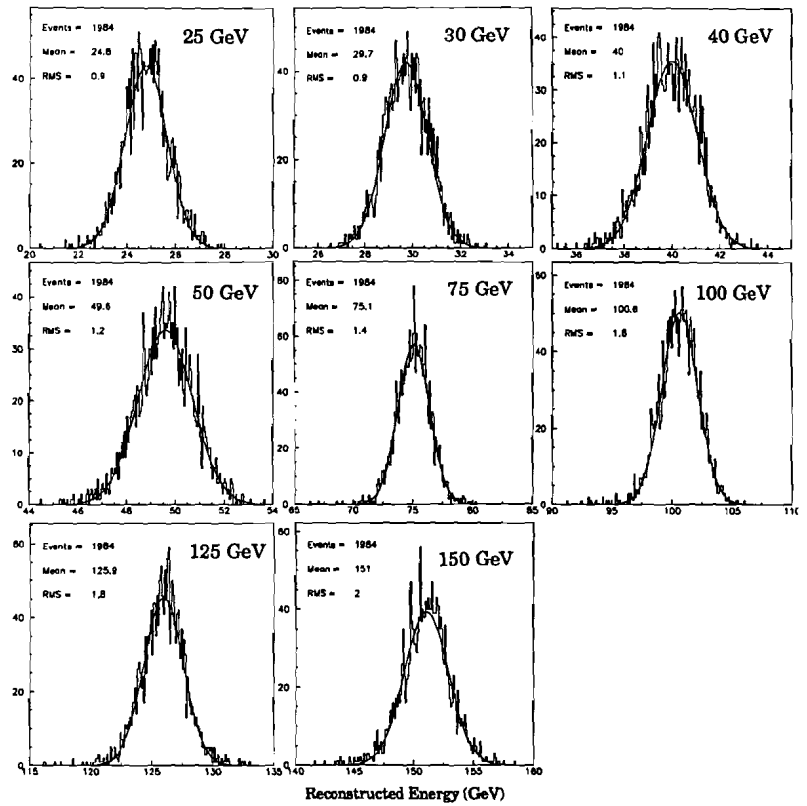

Figure B.4 Particle Library electrons from 25 GeV to 150 GeV

The energy fields within the Particle Library are assigned an identification number (ID), as shown in Table B.1.

Table B.1 ID numbers for the energy fields in the Particle Library

ID	1	2	3	4	5	6	7	8	9	10	11	12	13	14	15	16	17
Energy	2.0	2.5	3.0	4.0	5.0	7.5	10.0	15.0	20.0	25.0	30.0	40.0	50.0	75.0	100.0	125.0	150.0

A plot of the electron and hadron responses versus incident energy, along with a second-order polynomial fit to that data, are shown in Fig. B.5 (the parameters of the fits, and their statistical errors, are given in the graphs).

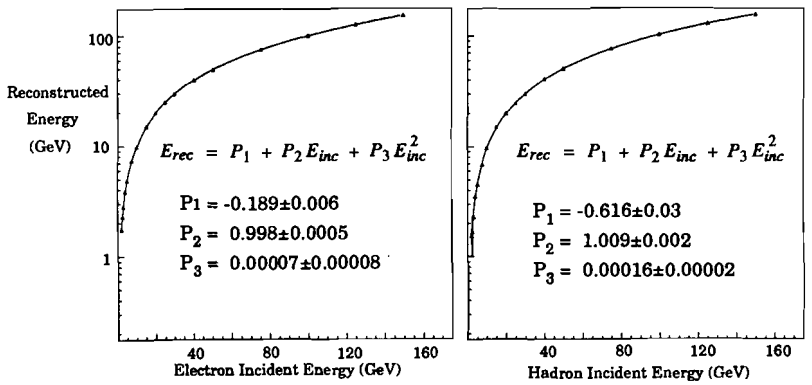

Figure B.5 Polynomial fits to electron and hadron data in the Particle Library

B.2 Using the Test Beam Particle Library to Simulate DØ Jets

Given the information about the constituents of a jet, the Particle Library can be used to simulate DØ jets by adding together appropriate particles from the test beam on a cell-by-cell basis. The "jet-builder" is a routine that can be used either in a standalone Fortran program, or linked to the DØ Library. In the latter case, a special version of the jet-builder deposits the simulated jet event directly into some appropriate DØ Zebra banks for direct manipulation with the standard DØ analysis packages. The description here focuses primarily on the DØ Library version.

Since the Particle Library contains electrons and hadrons in narrow energy bands, with energies only down to 2.0 GeV, and the data were taken only at η=0.05 and ϕ=3.10 radians (3.16 DØ units), several approximations must be made when other showers are needed for forming TB jets. In the following, we assume that the jet-builder has been

given the command to build a jet of N particles, and that each particle i has pseudo-rapidity η_i, azimuth ϕ_i, energy E_i, and is of particle type T_i.

When using single-particle events from the TB Particle Library, the energy of any chosen shower must be scaled to the appropriate energy of the jet fragment, then shifted spatially to reflect the appropriate trajectory. Finally, all the particles must be added together to form a TB jet. The step-by-step procedure is outlined here, and the individual parts are described in detail in the following sections.

1. For each particle i, the jet-builder first selects an appropriate shower from the library. It does this by choosing the nearest field and particle type (this procedure is described in Section B.2.1), and then selecting randomly an event from within the field, and reading the cell-level information from the Library into an array.
2. Each cell in the event is then scaled for energy by a value λ_i (described in Sec. B.2.2).
3. Each cell of the event is then shifted by $\delta\eta$ and $\delta\phi$ (described in Section B.2.3).
4. The cells are then added together into a jet (Section B.2.4).
5. After all particles are processed, the final TB jet is presented to the analysis routines.

B.2.1 Particle and Energy Field Selection

The Particle Library is rather primitive, being limited in both energy range and particle types. In particular, π^0s and photons are approximated by single electron showers. All hadrons are approximated by πs, and all muons are ignored. Thus, the particle type is either hadron or electron.

The jet-builder determines the appropriate Particle Library energy field by finding the energy field with the nominal energy value closest to the fragment energy E_i, and assigning the appropriate ID (from Table B.1) to the fragment. Particles with energies of $E_i \geq 150$ GeV are chosen from the 150 GeV fields (ID 17), and particles with energy $E_i \leq 2$ GeV are chosen from the 2 GeV fields (ID 1).

B.2.2 Energy Scaling

Using the parameters given in Fig. B.5, the required energies are scaled by a factor λ_i, which is found by:

$$\lambda_i = \frac{P_1 + P_2 E_i + P_3 E_i^2}{P_1 + P_2 E_{id} + P_3 E_{id}^2} \tag{B.1}$$

where E_i is the energy of the jet constituent particle as given above, and E_{id} is the nominal energy of the Particle Library field, as found from the Fortran code given above (E_i is represented in the code as E_ID, and E_{id} is represented by E_ID). Every cell in event i from the Particle Library is then scaled by λ_i.

Using this procedure, when $E_i = E_{id}$, $\lambda_i = 1$ as expected. Thus, energies between the nominal energies are scaled appropriately, and energies both above and below are projected according to the trend established by energies from 2 GeV to 150 GeV.

This procedure has three principal drawbacks. First, particles of energy below 2 GeV probably do not follow such a projection, so very low energy particles are not represented accurately. Second, it is likely that particles with energy below a certain magnitude probably do not even make it past the upstream material into the DØ detector, especially electromagnetic particles. Finally, using the above algorithm means that all hadrons below 2 GeV are constructed out of the extremely small event sample available for such hadrons (308 events, which represent all the available processed 2 GeV hadrons from the test beam).

To properly establish a prediction of low energy response, Monte Carlo studies should be made of the behavior of such low energy particles. However, since such a study was not available, an arbitrary 300 MeV cutoff was made on constituent particles. Effectively, this means that any particles with $E_i < 300$ MeV have $\lambda_i = 0$, and do not contribute to the jet event.

B.2.3 Position Shifting

For a track with $\eta = \eta_i$ and $\phi = \phi_i$, the jet-builder finds $\delta\eta_i$ and $\delta\phi_i$, the shifts of the events from the Particle Library, as follows:

$$\begin{aligned} \delta\eta_i &= \eta_i - 0.05 \\ \delta\phi_i &= \phi_i - 3.16 \end{aligned} \tag{B.2}$$

The coordinates of every cell k in the Particle Library event are then shifted by:

$$\begin{aligned} \eta_{ik} &= NINT\left(\eta_{ik}^o + \delta\eta_i\right) \\ \phi_{ik} &= NINT\left(\phi_{ik}^o + \delta\phi_i\right) \end{aligned} \tag{B.3}$$

where η^o_{ik} and ϕ^o_{ik} are the coordinates of the cell for the shower in the Library, η_{ik} and ϕ_{ik} are the transformed coordinates, and the nearest integer of each shift is taken to obtain a new cell address for each cell k.

This procedure has the disadvantage that it does not properly simulate particles at large $|\eta|$. Since cells in the central region are larger than cells in the regions at higher $|\eta|$, the simulation results in jets with large $|\eta|$ that are identical to jets with small $|\eta|$. However, the approximation can still be useful for certain issues, such as investigating the distribution of jets with pseudo-rapidity according to Monte Carlo. The jet-builder creates DØ jets up to a pseudo-rapidity of $|\eta| \approx 4.5$. Since there are gaps in coverage in the transition between the CC and the EC, and the layers are of somewhat different distribution between the two calorimeters (the EC has 4 EM + 5 IH layers, while the CC has 4 EM + 3 FH + 1 CH layers), transformations of the cells in the CC are made to the appropriate cells in other regions, for the portion of the jet that is not contained in the CC. Where a transformation of a particular cell cannot be performed due to less complete coverage (especially in the Inter-Cryostat Region), the jet-builder simply "drops" the cell from the CC, thus further reducing the accuracy of the jet mapping at high $|\eta|$.

Translations in ϕ are handled by a simple rotation of azimuthal coordinates (as was shown above), and due to azimuthal symmetry of DØ, ϕ translations are less questionable.

B.2.4 Constructing the Jet

The individual showers are added together to obtain the final TB jet as follows. We include this as a technical reference for a programmer desiring to construct a similar program. First an integer array is created, of the form INDEX(30,-60:60,64), along with an empty real vector JET_DATA(60000). Once data from the first particle is available,

each cell k in the particle shower is entered into the variable JET_DATA(J). Each time an entry J is opened in JET_DATA, the value of J is assigned to INDEX($L^k_i, \eta^k_i, \phi^k_i$), with L^k_i the layer index for that cell, and η^k_i and ϕ^k_i the shifted coordinates. After the data for the first particle in the jet is entered, the vector JET_DATA contains M non-zero entries, where M is the number of cells in the first shower.

As succeeding particles are processed, the array INDEX(L_i, η^k_i, ϕ^k_i) is first checked to see if an entry for the cell with coordinates L_i, η^k_i, and ϕ^k_i had previously been made. If so, the energy of the cell k is added to JET_DATA(J) (where J = INDEX(L_i, η^k_i, ϕ^k_i)). If no entry had been made, the energy of cell k is entered into the first empty space in JET_DATA, and then the array INDEX is updated accordingly. Thus, as particles within a jet are processed, the vector JET_DATA grows, and INDEX receives entries. After all showers are entered, and the jet event is submitted for analysis, the two variables INDEX and JET_DATA are reinitialized to zero and processing is begun on the next jet event.

This method of building TB jets provides a very powerful tool for analysis, but it has some limitations. The most important is that the noise in a TB jet is much greater than in jets expected to be produced at DØ. This is because, as events are added together to form jets, the intrinsic noise in those events is also added together. Nevertheless, the mean response, shape, and shower development for TB jets should be very similar to that of a DØ jet.